DUSTY RINGS AND CIRCUMPLANETARY DUST: OBSERVATIONS AND SIMPLE PHYSICS

JOSEPH A. BURNS, DOUGLAS P. HAMILTON,
MARK R. SHOWALTER
Cornell University, University of Maryland, Stanford University

Each giant planet is encircled by planetary rings, usually composed of particles centimeters to meters in radius, but each system also contains regions where much smaller dust grains predominate. This chapter summarizes the techniques used to determine the properties of circumplanetary material, and then gives a precis of the known characteristics of circumplanetary rings (with emphasis on tenuous structures) and dust grains, before describing some of the physics and orbital dynamics relevant to them. *Jupiter*'s dusty rings (as discovered by the Voyager and Galileo spacecraft) have three components: i) a radially confined and vertically extended *halo* which rises abruptly, probably due to an electromagnetic resonance; ii) a 6500-km-wide flattened *main ring* that shows patchiness and whose outer edge is bounded by the orbit of the satellite Adrastea; and iii) a pair of exterior *gossamer rings* that seem to be derived from the satellites Amalthea and Thebe whose orbits circumscribe these rings. In addition, small particles are strewn throughout the inner Jovian magnetosphere, especially near the paths of the Galilean moons, and the jovian system seems to eject very tiny particles at hypervelocities to interplanetary space. *Saturn*'s circumplanetary dust is unusual in the size distribution of its various rings: the broad and diffuse E ring seems to be mainly 1-micron grains whereas the narrow F and G rings have quite steep size distributions, indicating the predominance of very small grains. Surprisingly little dust resides in the main Saturnian rings, except in the localized spokes. Dust is interspersed between the narrow classical *Uranian* rings, forming a sheet that is punctuated by narrow bands and gaps. *Neptune*'s system contains at least some grains that lie well off the planet's equatorial plane, perhaps as a result of Neptune's highly tilted and offset magnetic field. The debris lost off the small moons Phobos and Deimos is believed to produce very tenuous *dust tori around Mars*. Complex orbital histories for circumplanetary grains result from conservative and non-conservative forces (gravity, radiation pressure and electromagnetism); the latter become most important for smaller particles and may even lead to ejection or planetary impact. Orbital resonance phenomena, several of which are unique to circumplanetary dust, seem to govern the distribution of grains orbiting planets. Circumplanetary dust is short-lived in a cosmic sense, owing to erosion through sputtering by the surrounding magnetospheric plasma and orbital loss due to various evolution mechanisms. These brief lifetimes imply continual regeneration to supply new material. Circumplanetary dust is often found in intimate relation with embedded small moonlets since it can be generated through energetic impacts into such bodies but is also absorbed by them.

I. INTRODUCTION

Innumerable dust grains circle each of the giant planets, not only interspersed among the macroscopic bodies that comprise the familiar opaque ring systems, but also elsewhere forming tenuous structures of their own. The original detections of dust clustered near the equatorial planes of Jupiter and Saturn were accomplished a quarter-century ago by pressurized "beer-can" experiments aboard the Pioneer spacecraft (Humes 1976, 1980). The distribution and properties of these tiny motes in the neighborhoods of all the giant planets were more thoroughly explored in Voyager images. In addition sensitive plasma detectors aboard Voyager found dust strewn throughout planetary systems in quantities too faint to be visible. Most recently circumjovian dust has been studied by Ulysses and Galileo instruments. From the ground, circumsaturnian and circumjovian dust rings were viewed during the 1995-96 and 1997 ring-plane crossings. Cassini's scientific payload, including imaging systems extending from the UV to the IR, a sophisticated dust detector and plasma instruments, is capable of revolutionizing our understanding of Jupiter's dust rings (during flyby at the end of 2000) and Saturn's complement of dust (throughout the 4-year tour, commencing in 2004).

Circumterrestrial dust is, of course, well known historically with the most diagnostic information coming from LDEF (see chapter by McDonnell et al.). Because the circumterrestrial data differ so markedly from those about the other planets, we will not consider the Earth's particles at all although our dynamical modeling is of course relevant. Dust has not been unequivocally found around any other terrestrial planet, although Dubinin et al. (1990) claim to have detected some material about Mars; the Japanese Planet-B (Nozomi) spacecraft is carrying an ionization dust detector that should map the dust distribution in this system. In explanation of the Soviet observation and in preparation for this latter mission, a dozen or so papers have been written concerning Martian dust since the late 1980s. This interest is appropriate since Soter's prescient (1971) report first explored the modeling of circumplanetary dust in connection with this system.

Several motivations provoke interest in circumplanetary dust. First, ring dynamicists are challenged by the wide range of forces to which these grains are subject and by the counter-intuitive behavior of some of this material. Second, circumplanetary grains intimately interact with the surrounding magnetospheric plasma and with neighboring satellites, in some cases being derived therefrom and in others modifying those surfaces. Thirdly, dust probes conditions in the surrounding magnetospheric plasma and, through its response, calibrates the nature of those fields. Finally, Cassini mission designers are justifiably concerned about sizes and realms of circumsaturnian dust since Cassini will pass continually (and usually at high relative speed) through the faint rings; optical surfaces can be scoured by the impacts of small grains, while larger collisions can destroy other components or even the entire spacecraft. In an earlier case Galileo's probe was redirected to avoid Jupiter's gossamer ring

following its discovery (Showalter et al. 1985).

The applicable physics and dynamics acting on circumplanetary dust are distinct from those pertinent to interplanetary dust, because the dust orbits through a magnetosphere and about a central mass other than the radiation source. But circumplanetary dust particles are not classical ring particles either. In the latter case, collisions dominate and the resultant structures can be studied with the tools of fluid dynamics and kinetic theory. For faint rings, collisions among ring particles are rare, and each particle behaves as a miniature independent satellite circling its primary; thus the methods of single-particle dynamics may be applied. However, as constituent particles are generally tiny, non-gravitational forces (electromagnetism, radiation and drag) must be included.

Previous overviews of circumplanetary dust have been written mainly in the context of planetary rings (e.g., Burns et al. 1984; but see Burns 1991). Reviews by Mendis et al. (1984) and Grün et al. (1984) emphasized electrodynamic processes in rings, whereas Mignard (1984) was concerned with the role of radiation pressure; the dynamics of circumplanetary dust were described by Burns et al. (1979) and Hamilton (1993) among others. Goertz (1989), Northrop (1992), Hartquist et al. (1992), Mendis and Rosenberg (1994) and Horányi (1996) have provided the most recent reviews of dusty plasmas in an astrophysical context. Much activity, seeking explanations for various puzzling phenomena found by spacecraft, has been carried out in the last decade but, to date, has not yet been summarized. The only available text on the subject is Bliokh et al. (1995).

This section will be organized as follows. After describing the techniques used to characterize circumplanetary dust, we will outline our knowledge of the fine material strewn around the giant planets sequentially in distance from the Sun. We will then discuss the forces that act on circumplanetary dust and the relevant physical processes before considering celestial mechanics. Finally we will suggest future studies. As mentioned above, we do not discuss circumterrestrial dust; we also do not consider interplanetary particles found to be streaming away from Jupiter by the Ulysses and Galileo dust detectors and thought to have originated somewhere in the bowels of the planet's magnetosphere. We do not discuss interplanetary and interstellar dust particles, although they penetrate planetary magnetospheres, except insofar as they may generate circumplanetary dust through impacts onto satellites and other orbiting bodies.

The sorts of questions that we will address in this chapter concern the sources and fates of circumplanetary dust. How do faint rings evolve? How old are planetary rings? What causes the tenuous ring systems to differ so much? Why are some faint rings confined while others are vertically or radially extended? Which of the phenomena displayed by our relatively simple dynamical systems are relevant to the collisionally dominated classical ring systems?

II. DESCRIPTION

In this section we review how ring properties are determined and then we summarize the properties of the known dusty rings. Detailed imaging observations of a planetary ring, at multiple wavelengths and phase angles, provide a wealth of information on a ring's global characteristics including its radial and vertical structure, particle size distribution, and normal optical depth. In addition, particle detectors on spacecraft can provide information on local conditions within diffuse dusty rings. Pioneer 10 and 11's dust detectors returned limited data on $\sim 5 - 10~\mu$m particles from the near-Jupiter and near-Saturn environments, while Voyager's PWS and PRA experiments proved to be sensitive to micron-sized dust around all of the giant planets. The dust detectors aboard Ulysses, and especially Galileo, provide the best calibrated and most useful dust detections in the jovian system. As described below, both imaging and *in situ* observations allow us to determine – or at least put useful constraints on – the gross properties of a planetary ring

A. Physical Models

For our purposes, we define a ring to be any ensemble of particles orbiting a planet. In general, most rings are circular, vertically thin, equatorial and axisymmetric, although specific rings exist that violate each of these generalizations (Burns 1999). The challenge to astronomers is, from remote measurements of a ring, to infer the physical and orbital properties of the constituent particles. In this section we present a brief overview of the methods used to model the physical properties of a ring.

Typical properties that one wishes to learn about a planetary ring are its radial distribution, particle sizes and composition. At any location in a ring, particle sizes can be described by a differential size distribution $n(s)$, defined such that $n(s)ds$ is the number of particles per unit ring *area* (i.e., integrated normal to the ring plane) in the radius range s to $s+\mathrm{d}s$. The particles that comprise the known rings extend in size from smaller than a micron to ~ 10 m.

One of the most fundamental properties of a ring is its *normal optical depth* τ, which is the quantity directly probed by ring occultation experiments. It is related to the local size distribution via

$$\tau = \int \pi s^2 Q_{\mathrm{ext}}(s) n(s) ds ~. \tag{1}$$

Here the extinction efficiency Q_{ext} is the dimensionless ratio of a particle's extinction cross-section to its physical cross-section; it describes the fraction of light impinging upon a particle that is either absorbed or scattered into a different direction while the remainder of the light continues unimpeded. If Q_{ext} were to equal 1, τ would be the fractional area of a ring filled by particles (at least for $\tau \ll 1$; more precisely, the filling fraction is $1 - e^{-\tau}$ if particles are positioned randomly).

However, this simple interpretation of τ is actually only appropriate for particles much larger than the wavelength of light. For tiny dust grains, Mie theory is typically employed to derive Q_{ext} as a function of radius s (van de Hulst 1981). Mie theory assumes the grains are homogeneous spheres; variant formulations (e.g., Pollack and Cuzzi 1980) can be used to model more irregular shapes. Within these theories, the two key free parameters are the refractive index, which depends on the composition, and the particle size. Particle sizes are best described by a dimensionless "size parameter" X, defined as $2\pi s/\lambda$, where λ is the wavelength of light. In general, Q_{ext} is of order unity for X of order unity (cf. Fig. A2 of Cuzzi et al. 1984); it decreases rapidly (typically $\propto X^4$) for smaller X, in the Rayleigh scattering limit. For this reason, measurements of a ring's optical depth are generally insensitive to particles much smaller than the wavelength. Accordingly, a ring's optical depth generally decreases with increasing λ, and this decrease can be used to constrain the particle sizes. For larger X, Q_{ext} rapidly levels out to a value of two; this difference from our expected value of unity will be discussed further below.

In practice, the optical depth measured in a ring occultation experiment is not the normal optical depth τ, but the larger value τ/μ, where μ is the cosine of the emission angle (measured from the ring normal vector to the line of sight). This μ factor corrects for the increased line of sight when the ring (assumed to be a flat slab) is not observed pole-on. Because the value of μ is known in any given experiment, however, recovery of the ring's normal optical depth is straightforward.

Rings are detected usually through the light that they absorb or reflect. For a ring in which τ/μ is small, a simple relationship exists between the ring's properties and the intensity of light I (power per area per wavelength interval per steradian) reflected:

$$\frac{I}{F} = \frac{\tau \varpi_0 P(\alpha)}{4\mu} \; . \tag{2}$$

Here I is expressed as a dimensionless ratio relative to F, where πF is the incoming solar flux density (power per area per wavelength interval). By this definition, I/F removes the effects of the Sun's spectrum and its distance from the ring, and it equals unity for a perfectly diffusing "Lambert" surface illuminated at normal incidence. In addition to τ, the key ring properties here are the single scattering albedo ϖ_0 and phase function $P(\alpha)$, where α is the phase angle or Sun-ring-observer angle. Both quantities can be derived from Mie theory (for example) and represent averages over the size distribution. Single-scattering albedo ϖ_0 describes the fraction of impinging light not absorbed by the particle, and always ranges between zero and one. The phase function describes the fraction of light scattered into various directions; it is normalized to an average value of unity when integrated over all solid angles.

The phase function is extremely sensitive to particle size. In the Rayleigh-scattering limit ($X \ll 1$) the phase function becomes isotropic to within a factor of two (see Fig. A2 in Cuzzi et al. 1984). As X increases to order

unity, the phase function becomes predominantly forward-scattering due to diffraction, with a large peak at $\alpha = 180°$. It also retains a shallower peak near backscatter ($\alpha = 0°$) and a minimum at intermediate α. As X increases further, half of the energy is diffracted into an ever-narrower forward-scattering peak, of angular width $\sim \pi/X$, while the remainder of the phase function is predominantly backscattering.

The mysterious result that $Q_{\text{ext}} \to 2$ for large X, called Babinet's principle and mentioned above, is closely related to this narrow diffraction spike in forward-scatter. For X extremely large (as is the case for centimeter and larger objects under visible light) it becomes impractical to distinguish the narrow diffraction peak from un-scattered light rays. One therefore tends to eliminate this component of the phase function and simultaneously halve Q_{ext} to its expected value of unity. For this reason, phase functions of macroscopic bodies (such as moons) never include the diffraction spike. However, it should be noted that, under special circumstances, this spike cannot be neglected. For example, radio occultations of planetary rings record the phase of the signal in addition to its amplitude; the forward-diffracted signal undergoes a phase shift relative to the direct signal so the two components can be distinguished. For this reason, the definition of τ, as given in (1), for a radio occultation experiment typically differs from its visual counterpart by a factor of two. Cuzzi (1985; see also Porco et al. 1995) discusses other circumstances in which this pitfall arises.

In Eq. (2) above we made the assumption that the ring was optically thin. This is not the case for some rings, so the relation breaks down. For larger τ it becomes probable that some ring particles will shadow or block others, in which circumstance (2) becomes a significant overestimate of I/F. Furthermore, multiple scattering of light among particles leads to a more isotropic phase function. Under these circumstances, more accurate "radiative-transfer" calculations are employed, analogous to those used in atmospheric sciences. The "doubling" algorithm is most general, in which the theoretical I/F pattern for a ring is built up by successive summings of lower-τ layers (Hansen 1969). In these approaches, it is possible and often necessary to include the secondary illumination from the planet in addition to sunlight (Cooke 1991; Dones et al. 1993; Showalter 1996); for rings close to a planet, this secondary illumination can be quite significant.

Nevertheless, as will be shown below, usually the dusty planetary rings are extremely optically thin, so that (2) can be used directly. In these cases it is convenient to introduce the concept of the "normal I/F," $\equiv \mu I/F$, meaning not the value measured, but instead the value that would have been measured if the ring were viewed normally. By applying this μ factor, one can trivially compensate for a ring's intensity variations with emission angle, and this can simplify data analysis.

Of course, astronomers are confronted with the inverse problem to that described above—one is not given a ring and asked to deduce its scattering behavior; instead one acquires a set of measurements and wishes to infer the

ring's properties. Then the size distribution $n(r)$ has no unique solution, and one can only consider a restricted set of models. For tiny dust, the most common distribution considered is a power law, of the form

$$n(s) = Cs^{-q} \, , \tag{3}$$

where q is called the power-law index, with larger q implying a steeper size distribution, and C a normalization constant. These distributions have the advantage of simplicity, with only two free parameters. In addition, power laws are widely observed in astrophysical and geological systems (Dohnanyi 1972; also see below). In practice, one needs to specify lower and upper limits to the size distribution in order to calculate the integrals above. However, in most cases the precise limits are not important. For $q < 7$, the lower limit is unimportant as long as it falls well into the Rayleigh scattering limit; in practice, distributions steeper than $q = 7$ have never been encountered. For $q > 3$, the number density drops off fast enough with s to make the precise upper limit irrelevant. Even for flatter distributions, the upper limit rarely plays a major role in the scattering properties, although one should always perform tests to verify this.

In addition to the dust, photometric models usually include a population of larger bodies. As we will see below, the lifetime of dust in planetary rings can be quite short, so these larger bodies are needed to serve as "parents" for the visible dust (Burns et al. 1980). In this regime, very little can be inferred about actual sizes of the parent bodies, because anything larger than ~ 1 cm scatters light indistinguishably. In this situation (2) can be simplified somewhat by using the geometric albedo $k \equiv \varpi_0 P(0°)/4$, yielding

$$I/F = (k\tau/\mu)P(\alpha)/P(0°) \, . \tag{4}$$

The unknowns k and $P(\alpha)$ are then based on values inferred for nearby or analogous moons. For this reason, the best one can generally hope for is a constraint on the ring's total optical depth in larger bodies, not their sizes. Sometimes, however, occultation data at radio wavelengths are available to better constrain this size regime.

These two populations, "small" and "large" bodies, are well distinguished by their scattering properties, because dust tends to be highly forward-scattering whereas the parent bodies are mostly backscattering. In practice, one usually first lets measurements at higher phase angles constrain the dust distribution. Then one uses photometric models to predict the ring's brightness in backscatter, and any shortfall of the model relative to the measurements serves as a constraint on the parent bodies. The ratio of dust to parent bodies in a ring is typically characterized by a dust fraction f, equal to the dust optical depth divided by the ring's total.

B. Observational Methods

Most of our knowledge about the diverse family of planetary rings comes from the reconnaissance of the outer planets by Voyagers 1 and 2. These two spacecraft encountered Jupiter in 1979 and Saturn in 1980 and 1981, while Voyager 2

proceeded to Uranus in 1986 and to Neptune in 1989. However, Pioneer 11 actually provided the first closeup data from Saturn a year before Voyager, in 1979. Although its imaging capabilities were inferior, its trajectory sampled very different regions of the Saturn system and provided complementary data. In recent years the capabilities of Earth-orbiting instruments such as Hubble Space Telescope (HST) and large ground-based, infrared optimized instruments like Keck's 10-m telescopes, have improved tremendously, and these data sets, especially those taken during ring-plane crossings, provide valuable complementary information. Ongoing observations by Galileo at Jupiter and future ones by Cassini at Jupiter, and especially at Saturn, will likely revolutionize the field of ring studies in much the way that the Voyager encounters did in previous decades.

1. Images. By far the largest body of information we have about planetary rings comes from images. A single image can record a ring system's I/F as a function of radius and longitude, unlike other data sets which typically only constrain a single location at any one time. During the Voyager encounters, the ring systems were imaged by wide- and narrow-angle cameras through a variety of phase angles and emission angles over a period of weeks to months. Spatial resolution was as fine as a few km. Wavelength coverage ran through the visual band using several broadband filters (Smith et al. 1979a, 1979b, 1981, 1982, 1986, 1989). Galileo's images of Jupiter's ring, which were primarily taken through the clear filter (0.6 μm), had much improved signal to noise (Ockert-Bell et al. 1999; Burns et al. 1999); a sequence of infrared images (0.9–5.2 μm) was also obtained (McMuldroch et al. 2000).

As we will see below, many of the known dusty rings are extremely faint, some with $\tau < 10^{-6}$. Such rings required long exposure-times and this seriously reduced the number of useful images acquired. Indeed, some of the rings discussed below are only known because of a handful of Voyager observations, or just a single detection. Color information was also often severely limited; the Voyager and Galileo clear filters (with pass-bands centered near 0.5 μm and 0.6 μm, respectively) had much greater transmissivity than the typical narrow-band filters, and so fainter rings were usually imaged through the clear filters. On the other hand, because an image comprises many pixels, it is often possible to make suitable pixel-averages to improve significantly the detectability of faint rings that are not obvious to the eye.

Compared to spacecraft, Earth-based observatories are capable of observing rings over much longer time periods and through a much broader range of wavelengths and ring opening angles, although they are restricted to small phase angles. A few Earth-based images have begun to rival the quality of some Voyager data; the Planetary Camera aboard HST can image Saturn's ring system with a resolution of 300 km per pixel. HST and other Earth-based observatories were used widely in 1995-96 to observe Saturn during the Earth and Sun's passages through the ring plane (Nicholson et al. 1996). Jupiter's ring-plane crossings in 1997 have afforded comparable viewing opportunities (de Pater et al. 1999). These rare edge-on viewing geometries, which in Sat-

urn's case only come every 15 years, make it possible to detect faint rings and small moons that are normally lost in the glare of the main rings. This geometry also maximizes the line-of-sight optical depth of a ring, because the factor $1/\mu$ becomes very large.

In addition to the terminology introduced above, a few additional concepts are valuable when working with ring images. In particular, many of the rings of interest are quite narrow, often unresolved in an image. Under such circumstances, it makes no sense to talk about the ring's peak I/F because that value varies inversely with image resolution. To compensate, one introduces the "equivalent width," $\int(I(a)/F)da$, where a is the projected distance from the planet's center in the ring plane. By converting the image to a radial profile $I(a)/F$ and then integrating under the curve, the effect of variations in resolution, width, and smear can be eliminated. For rings that are both optically thin and narrow, the "normal equivalent width," scaled by μ, removes the emission angle dependence as well.

2. Spectra. In much of planetary astronomy, spectral measurements provide our most direct information about the composition of surfaces and atmospheres. The same is true for Saturn's rings, where absorption bands in the infrared indicate that water ice is the major component (see Cuzzi et al. 1984; Esposito et al. 1984 and references therein). However, beyond the recognizable absorption bands, particle composition is difficult to infer because spectra from laboratory samples do not duplicate the multiple scattering prevalent within denser rings.

Multiple scattering is not an issue in faint and dusty rings, but other more substantial difficulties arise. First, these rings are especially difficult to detect unless one averages over broad swaths of wavelength (eliminating spectral information), or else uses exceedingly long exposures. For this reason, even broadband spectrophotometry has rarely been acquired for most optically thin rings. Second, absorption bands are a phenomenon uniquely associated with macroscopic bodies, arising because the material rapidly dissipates light energy at specific wavelengths. For particles comparable in size to the wavelength, the path length of a light ray through the substance is too small for this absorption to become significant. Composition, therefore, is never measured directly for dusty rings; it is usually assumed, based on the composition of the nearby moons and denser rings.

This is not to say, however, that color measurements of a ring are not useful. Although they do not constrain composition, they provide valuable information about the dust particle sizes. The reason is that the wavelength defines the "yardstick" by which the size distribution is measured, so the phase function and optical depth can be strong functions of wavelength. For example, very steep distributions are dominated by tiny Rayleigh-scatterers and so tend to appear blue, for the same reason that the sky is blue. Hence, the color of a ring can provide very useful size information as a complement to phase angle coverage.

3. Occultation Profiles. Occultation experiments fall into two general categories—stellar and radio. In the former case, a ring passes in front of a star

as seen from the observer, who measures the star's brightness as a function of time. Upon reconstructing the projected path of the star, one derives a profile of the ring's optical depth as a function of radial position and longitude. Stellar occultation experiments have been performed from both spacecraft and Earth-based observatories. The rings of Uranus and Neptune were, in fact, discovered in this manner (Elliot et al. 1977; Hubbard et al. 1986). Radio occultation experiments consist of a spacecraft transmitting continuous-wave radio signals through a ring and back to Earth. In principle, "uplink" radio experiments are possible, in which an Earth-based transmitter sends the data to a spacecraft, but this has never been attempted.

Occultation experiments are capable of obtaining much finer spatial resolution than images, although only along a one-dimensional track. The photo-polarimeter (PPS) aboard Voyager performed stellar occultation experiments at Saturn, Uranus and Neptune, acquiring profiles with spatial resolution of 10–100 m at $\lambda = 0.265$ μm (Lane et al. 1982, 1986, 1989); the precise resolution depends on the available signal-to-noise (Colwell et al. 1990). Voyager's ultraviolet spectrometer (UVS) performed simultaneous observations at 0.11 μm, but these profiles are generally lower in resolution and signal-to-noise ratio (Sandel et al. 1982; Broadfoot et al. 1986, 1989).

Occultation profiles of Saturn's and Uranus' rings using the Voyager radio science subsystem (RSS) have resolutions comparable to the PPS experiments (Tyler et al. 1981a, 1986; Marouf et al. 1986). The RSS transmitter operated at two wavelengths simultaneously, 3.6 and 13 cm; comparison of the results from the two wavelengths provides our best constraints on the upper end of the particle size distribution (Marouf et al. 1983; Tyler et al. 1983; Zebker et al. 1985).

Earth-based occultation observations, now spanning more than two decades, provide a useful complement to these data sets. The detailed shape models for Uranus' rings (French et al. 1991) have only been possible because of regular occultation observations of these rings. On July 3, 1989 the bright star 28 Sgr was occulted by Saturn and its ring system, and the resultant ring profiles (French et al. 1993; Harrington et al. 1993; Hubbard et al. 1993) have resolutions approaching that attained by Voyager. An occultation experiment using the high-speed photometer aboard HST provided similar resolution (Elliot et al. 1993). Bash et al. (2000) have used the occultation of GSC 5249-01240 to understand the F ring's kinematics and photometry.

However, it should be remembered that most dusty rings are extremely optically thin, and in this case occultation observations become problematic (Tyler et al. 1981b). No occultation experiment has ever attained a sensitivity to $\tau \lesssim 10^{-3}$, so dusty rings cannot be detected in this manner. French et al. (1996) have summed many occultation profiles to bring out Uranus' λ ring. In the general situation, τ can only be modeled, along with the phase function, from image photometry.

By analogy to the equivalent width defined above for images, the "equivalent depth" D of a ring is defined as $\int \tau(a)da$. This quantity is again useful

when rings are only marginally resolved, or when occultation measurements are to be compared to results from images. We note in passing that a slightly different quantity also called "equivalent width" is sometimes used in occultation studies (Porco et al. 1995; see also references therein). It is defined as the radially integrated fraction of light removed from the stellar beam, or approximately $W_{occ} = \mu \int (1 - e^{-\tau(a)/\mu})da$. This is similar to the equivalent depth for small τ, but is a more directly measured quantity and can differ significantly from D when τ is large. However, in this paper we reserve the term "equivalent width" for the radially integrated I/F, as discussed above.

4. Charged Particle Absorption Signatures. All the ring observation methods discussed above rely on a ring's interaction with light. The ring's interaction with the charged particle environment of a planet provides an additional probe of the ring material. Pioneer 11, both Voyagers and Galileo's atmospheric probe, all of which passed near rings, carried arrays of instruments to study the electrons/ions trapped in the planetary magnetospheres they traversed. Some of these electrons/ions are absorbed when they intercept rings and moons, so the presence of rings can be inferred by a decrease in the phase space density of ions/electrons as the spacecraft crosses the ring's magnetic-field L shell. At both Jupiter and Saturn, Pioneer 11 returned data sets in some ways superior to those of the Voyagers because this spacecraft passed much closer to the planets and therefore probed more L shells containing ring material. The Voyagers did not cross any L shells that intercepted rings at Jupiter or Uranus. As Galileo's probe plunged at $6°$ out of the equatorial plane towards its destination in the atmosphere, its high-energy electron detector measured clean absorption signatures (Fisher et al. 1996). Specific experiments and their implications will be discussed below in the context of the particular rings to which they relate.

Unfortunately no instrument yet flown can characterize the full six-dimensional phase space of particles, so investigators must make assumptions to fill in the missing information; these assumptions are often subject to criticism. The distinction is widely made between a "macrosignature" caused by an axisymmetric ring versus a longitudinally incomplete "microsignature" trailing behind a moon or ring clump (Van Allen 1982; Cuzzi and Burns 1988). However, even this distinction is often subject to dispute; one observer's macrosignature may be another's microsignature. These uncertainties often hinder our inferences about ring properties from charged-particle-absorption data sets.

5. Direct Sampling of Ring Dust. The final way to probe a planetary ring is the (possibly perilous!) method of directly sampling the material using a dust impact-detector. On Pioneers 10 and 11, pressurized "beer can" dust detectors recorded occasional impacts by circumplanetary, interplanetary and interstellar dust particles, from which their density in space was inferred (Humes et al. 1974; Humes 1976, 1980). It is telling that these instruments recorded substantial increases in impacts during the crossings of Saturn's (and, to a lesser extent, Jupiter's) ring planes. Unfortunately, the design of the Pioneer instruments was such that impacts separated by upwards of 80 minutes were recorded as a single event, so one can only place a rough lower limit on the

number of dust particles in dense regions. The instruments were sensitive to a limited range of particle energies, corresponding to $s \gtrsim 5~\mu$m for Pioneer 10 and twice as large for Pioneer 11.

The Voyagers did not carry any dust detectors *per se*, but nevertheless acquired some useful information on ring dust. The Plasma Wave Spectrometer (PWS) and Planetary Radio Astronomy (PRA) instruments recorded substantial increases in impulsive noise during the ring-plane crossings at Saturn, Uranus and Neptune (Aubier et al. 1983; Gurnett et al. 1983, 1987, 1991; Meyer-Vernet et al. 1986, 1996, 1998; Pedersen et al. 1991; Oberc 1994; Tsintikidis et al. 1994, 1995). Plasma-wave data from Jupiter's flyby have also been reanalyzed (Tsintikidis et al. 1996). This noise is now recognized as having been caused by dust impacts into the spacecraft. Despite the challenges associated with interpreting data for which the instruments were never calibrated, these measurements have been used to constrain particle sizes, densities and vertical distributions.

The next generation of dust detectors is flying on the Galileo and Ulysses spacecrafts (Grün et al. 1992c) and an improved version is aboard Cassini. These sophisticated instruments obtain information about the number, mass, vector velocity and electric charge over a much broader range of particle sizes (Grün et al. 1992b, 1996b). The Cassini detector even will provide some compositional information. These devices have detected periodic bursts of sub-micron grains streaming away from Jupiter (Grün et al. 1992b, 1993, 1996a,b; Zook et al. 1996; Krüger et al. 1998a; Graps et al. 2000), presumably accelerated outward by the magnetospheric corotational electric field after originating at Io (Horányi et al. 1993) or Jupiter's rings (Hamilton and Burns 1993). Although safety constraints prevent these spacecraft from actually crossing through most known rings, the dust distribution in other regions of circumplanetary system, plus measurements of the influx of interplanetary and interstellar dust, are being characterized.

C. Physical Properties of the Dusty Rings

In this section we briefly summarize the properties of each of the dusty rings. The overall architecture of the known planetary ring systems is shown in Fig. 1 which illustrates the intimate association of rings and small ring-moons. Various general characteristics of the dusty rings are listed in Table I.

1. Jupiter's Ring System. Jupiter's ring system was discovered in a single, very-long-exposure (672 sec) image taken during Voyager 1's approach in 1979, and was subsequently imaged in greater detail by Voyager 2 and Galileo. The ring was vastly brighter in the high-phase images from Voyager 2, indicating diffraction by a large population of fine dust. As a result, it was the very first dusty ring to be identified from space. Earlier hints that this faint ring might exist came from a dip in the density of charged particles near Pioneer 11's closest approach to Jupiter (Fillius et al. 1975; Acuña and Ness 1976), as well as impact events recorded by the Pioneer dust detectors (Humes 1976; Fig. 9.1
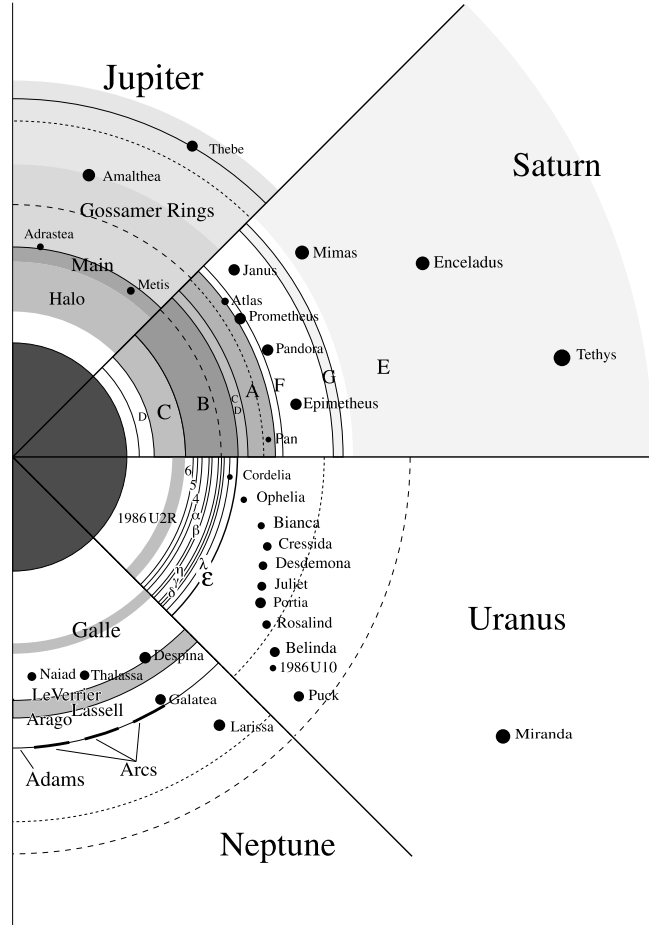
Figure 1. A schematic that compares the four known planetary ring systems (with distinct boundaries shown as solid arcs; radial limits that are poorly defined are not plotted), scaled to a common planetary radius (plotted as the solid central circle); the intimate association with ring-moons (small filled circles) is apparent. Within any planet's ring system, stippling suggests the relative optical depths of different ring components. All the ring systems lie within the Roche zones (tidal break-up, shown as dotted line for $\rho_{sat} = 1$ g·cm^{-3}) of their planets, and all are fairly near the synchronous orbit position (plotted as a dashed line). Courtesy of Judith K. Burns.

in Elliot and Kerr 1985). Multiple explanations for the absorption signature were available at the time, however, although Acuña and Ness did propose a faint ring as a possible cause.

Dust particles, some prograde and some retrograde have been found by Galileo's dust detector to orbit Jupiter (Grün et al. 1997). Clouds of grains are noted near the Galilean moons (Grün et al. 1998a,b; Krüger et al. 1998b),

J.A. BURNS ET AL.

Table I

Characteristics of Dusty Planetary Rings

PLANET	Location[1]; W[2]	Optical Depth τ; D[5]	Dust Fraction f	q[3] ; s[4]	Comments
JUPITER					
Halo	92 000– 122 500	10^{-6}	100	?	12 500 km thick
Main Ring	122 000– 128 980	$3 \cdot 10^{-6}$	~ 50?	$q = 2.5 \pm 0.5$	Brightness dip near Metis' orbit; bounded by Adrastea
Amalthea Gossamer	$\leq 129\,000$– 182 000	10^{-7}	100?	?	2 600 km thick; bounded by Amalthea
Thebe Gossamer	$\leq 129\,000$– 226 000	$3 \cdot 10^{-8}$	100?	?	4400 km thick; bounded by Thebe
SATURN					
D Ring	66 000– 74 500	10^{-3}	50–100	?	Internal structure as fine as 100 km
D72 Ringlet	71 710 $(W \leq 40)$	$D = 0.01$	89 ± 4	$q \leq 2.8$ or $s \geq 10$	
Main (C, B, A) Rings	74 500– 136 800	0.05–2.5	< 3	$q = 2.7 - 3.1$	Much variation
B Ring Spokes	100 000– 116 000	~ 0.03	100	$s = 0.6 \pm 0.2$	Minimum width at R_{syn}
Encke Ringlet	133 580 $(W \simeq 10)$	$D = 1$	100?	?	Shares orbit with Pan
F Ring Inner Sheet	136 780– 140 200	$(1\text{–}2)\cdot10^{-5}$	100?	?	Bounded by F Ring
F Ring	140 200 $(W \simeq 50)$	$D = 5$	≥ 98	$q = 4.6 \pm0.5$	Shepherded by Pandora and Prometheus
G Ring	166 000– 173 000	10^{-6}	> 99	$q = 1.5\text{–}3.5$	
E Ring	180 000– 450 000	peak $(1\text{–}2)\cdot10^{-5}$	100	$s = 1.0 \pm 0.3$	Peak near orbit of Enceladus; thickness 8 000–18 000 km, increasing with radius

Characteristics of Dusty Planetary Rings (continued)

PLANET	Location[1]; W[2]	Optical Depth τ; D[5]	Dust Fraction f	q[3] ; s[4]	Comments
URANUS					
1986U2R	37 000–39 500	10^{-4}–10^{-3}	?	?	
Dust Belts	41 000–50 000	10^{-5}	?	?	Fine internal structure down to < 100 km
Lambda Ring	50 024 ($W \simeq 2$)	10^{-3}	> 95	?	Adjacent to orbit of Cordelia; 5-cycle brightness pattern
NEPTUNE					
Galle Ring	41 000–43 000	4–$10 \cdot 10^{-5}$	?	?	
LeVerrier Ring	53 000 ($W \simeq 10$)	10^{-2}	40–70	?	Adjacent to orbit of Despina
Lassell Ring	53 000–58 000	1–$3 \cdot 10^{-4}$	?	?	Bounded at inner edge by Le Verrier
Adams Ring	62 930 ($W \simeq 50$)	10^{-2}	20–50	?	Adjacent to orbit of Galatea
Adams Arcs	62 930 ($W \simeq 10$)	10^{-1}	40–70	?	Adjacent to orbit of Galatea

[1] Radial Distance from planet's center; in km, [2] W = Radial Width; in km, [3] q = dust power-law index, [4] s = particle radius; in microns, [5] D = Normal Equivalent Depth; in km

presumably ejected during impacts. Horányi (1994) has suggested that some debris might be captured to form a ring and Colwell et al. (1998) have shown how a similar process could lead to Galileo's retrograde grains. Direct evidence of the charged dust interacting with the Jovian magnetosphere is available in these data (Horányi et al. 1997; Grün et al. 1997; Graps et al. 2000), which exhibit a 5 and 10 hr periodicities.

The most complete, post-Voyager, physical characterization of this ring system was performed by Showalter et al. (1985, 1987; Showalter 1989). Earth-based images of very high quality have been acquired by Nicholson and Matthews (1991) at Palomar's 5-m telescope and by de Pater et al. (1999) at Keck's 10-m telescope, the latter during the 1997 ring-plane crossings. These images rival Voyager's in clarity but
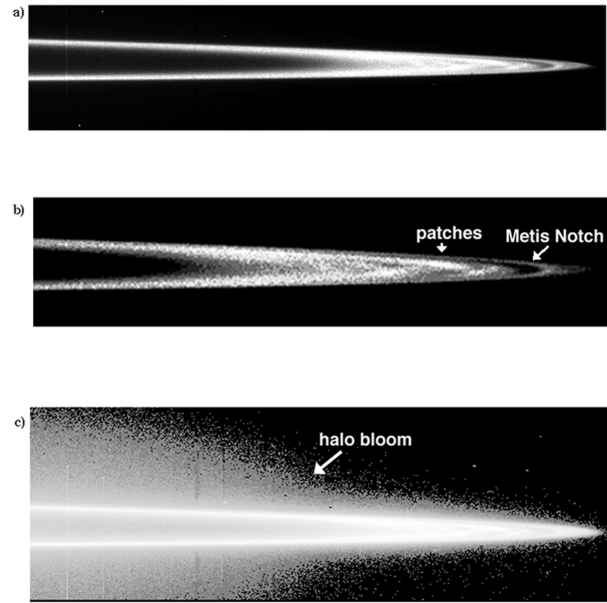
Figure 2. A Galileo view of the Jovian ring's west ansa, showing both the main ring and the halo's outer parts, processed in three different ways to highlight various features. (a) Stretched to contrast the main ring's diffuse inner periphery versus its much crisper outer boundary. (b) A stretch that emphasizes the patchy nature of the main ring's central region and the brightness dip associated with Metis' orbit. (c) A stretch to reveal the halo's development at the main ring's inner edge; it appears that the main ring itself has a faint cloud of material above and below. From Ockert-Bell et al. (1999).

were acquired at unique phase angles and wavelengths. However, a thorough analysis of them is not yet complete. Near-IR images (Meier et al. 1999 and polarimetric data (J. Gougen, private communication, 1998) were obtained by HST. The Galileo orbiter has returned high-resolution images of Jupiter's ring system mainly in forward-scattered light; these images are comparable in number to Voyager's, but the resolution is twice as good and the signal-to-noise and smear characteristics are much superior. A preliminary assessment of the Galileo images (Ockert-Bell et al. 1999) taken during Galileo's nominal mission for the most part confirms and refines Voyager results.

The current analysis of the Jovian ring system (Ockert-Bell et al. 1999) is based on measurements obtained during four orbits of Galileo's nominal mission, when 25 clear-filter images of the rings were taken as planned at spatial resolutions of 23 to 134 km/pixel; the ring appeared fortuitously in an additional 11 images taken during two of the same orbits plus a third. In confirmation of the previous interpretations from Voyager data, the tenuous Jovian rings can be considered to have three components: the main ring, halo, and gossamer ring. The first two of these components have typical normal optical
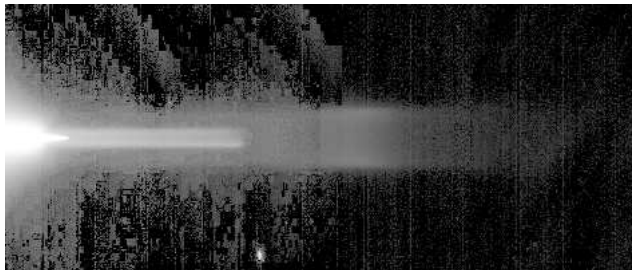
Figure 3. This mosaic of four Galileo images (416088922, 8968, 9022 and 9045), taken through the clear filter (0.611 μm) at an elevation of 0.15°, shows the edge-on gossamer rings of Jupiter across phase angles of 177-179°. The main ring and halo appear at left in white. The Amalthea ring is the narrower and brighter band extending to the right; the Thebe ring is the thicker and fainter band extending further. Each ring is bounded radially by the orbit of the corresponding moon; the crosses show the extreme positions (up/down; in/out) of the two satellites' orbits, which are eccentric and inclined. This image has been enhanced logarithmically to show all the ring components; in reality the Amalthea ring is ten times fainter than the main ring and halo, and the Thebe ring is ten times fainter than the Amalthea ring. The image, with a reprojected radial resolution of 400 km, has been expanded vertically by a factor of two to better show rings' vertical structure.

depths of a few times 10^{-6}, while the third's is one-twentieth or less that amount; all contain large fractions of micron-sized dust. The much better quality of the Galileo images has allowed the nature of these components to be refined and has revealed hints of interesting fine structure.

The innermost component, a toroidal halo (Figs.1 and 2c), extends radially from approximately 92 000 km to about 122 500 km (near the 3:2 Lorentz resonance, which is described in Sec. IV B) and has a full-width, half-maximum thickness of 12 500 km; its brightness decreases with height off the equatorial plane and decreases as the planet is approached. The main ring reaches from the halo's outer boundary across about 6 400 km to 128 940 km, just interior to Adrastea's orbit (128 980 km); at its outer edge, the main ring takes nearly 1 000 km to develop its full brightness. The ring's brightness noticeably decreases around 127 850 km in the vicinity of Metis' semimajor axis (127 980 km) (Fig. 2b). The main ring has a faint, vertically extended component that thickens as the halo region is approached. Brightness variations of $\pm 10\%$ are visible in the central main ring and may be due to vertical corrugations, density clumps or "spokes" in the ring. Unexplained differences between the near- and far-arm brightnesses are visible. Lying exterior to the main ring, the gossamer ring has two primary components (see Fig. 3), each of which is fairly uniform: one originates just interior to Amalthea's orbit (181 000 km) while the other is situated radially interior to Thebe's orbit (222 000 km). Very faint material continues far past Thebe, blending into the background perhaps as far as 250 000 km out. The gossamer rings have thicknesses that match quite well the maximum elevations of these satellites off Jupiter's equatorial plane; from Galileo's nearly equatorial view, the gossamer rings have greater intensities

along their top and bottom surfaces. The rings seem to be derived from the satellites (Burns et al. 1999).

Earth-based images taken at 2.27 μm during ring-plane crossing (de Pater et al. 1999) are generally consistent with this interpretation. These images and those from HST (Meier et al. 1999) show the vertically extended halo in backscattered light, and the halo is substantially fainter relative to the main ring than seen in the Voyager high-phase images. These differences may be attributed as due to dust which dominates the backscattering by the halo (since— in the nominal model—only dust, responding to non-gravitational forces, can be lifted out of the ring plane). However, further dynamical and photometric modeling (cf. Horányi and Cravens 1996), combined with the better data coming from Galileo, Cassini and Earth-based observatories, will be needed to settle this issue.

The photometry to date is based on Voyager measurements only (Showalter et al. 1987). The phase curve of Jupiter's main ring at high phase angles is compatible with a power-law size distribution of dust with index $q = 2.5 \pm 0.5$. The ring is distinctly red at these high phase angles, and its color implies the same index. The RSS atmospheric-occultation track crossed the main ring; since Tyler et al. (1981b) were unsuccessful in detecting the ring, their upper limit on the ring's optical depth was 5×10^{-4}, well above the actual value.

The Jovian ring's phase function is not sufficiently well known to place firm constraints on the population of larger bodies. Showalter et al. (1987) believed that $\lesssim 30\%$ of the ring's I/F in backscatter could be ascribed to the dust population, and that the remainder was caused by macroscopic bodies. However, this could not be proven rigorously. The interpretation that the backscatter is dominated by parent bodies is supported by the fact that the ring's color is very red, virtually identical to that of Adrastea (Meier et al. 1999) and Amalthea (Thomas et al. 1998; Simonelli et al. 2000). Gradie et al. (1980) have proposed that sulfur contamination from Io, combined with charged particles in the Jovian magnetosphere and impacts from micrometeoroids, act to darken and redden Amalthea's surface; if this is so, it stands to reason that parent bodies in the Jovian ring have been reddened similarly.

The analysis to date is inadequate to place severe constraints on the size distribution in the halo and gossamer ring, although the brightening toward high phase and the halo's possibly blue color relative to the ring (Meier et al. 1999) both imply that dust is the major constituent. If one assumes that the dust distribution matches that in the main ring, then the halo has a normal optical depth very similar to that of the main ring, whereas the gossamer ring's $\tau \sim 10^{-7}$ (Showalter et al. 1985, 1987). Showalter et al. (1987) have estimated the exponent in the power-law of the size distribution to be -2.5, but McMuldroch et al. (2000), from an analysis of a single forward-scattered sequence of infrared data, argue for a steeper size distribution.
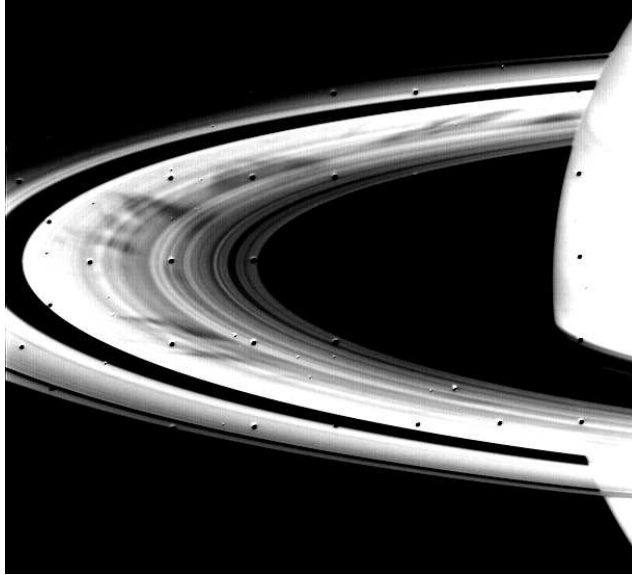
Figure 4. This Voyager 2 image (43643.34) of Saturn's A and B rings has been strongly enhanced in contrast to show spoke activity across the B ring. The phase angle is 7.5°. The Cassini Division is the sharply defined band between the rings.

2. Dust in Saturn's Main Rings and Spokes. Saturn's is the most expansive and most diverse of the planetary ring systems. The two most prominent rings, designated A and B, were discovered by G. Galileo using his first crude telescope in 1612; the inner C or crepe ring was not identified as a separate entity until 1850. The close scrutiny by the Voyagers in 1980 and 1981 revealed a system with remarkable amounts of structure; the closer one looks at Saturn's rings, the more detail one sees. The three main rings have optical depths in the range ~ 0.1–5 (Fig. 1). Photometric models for these rings indicate that all are extremely depleted in dust, with limits on the dust fraction in the A, B and C rings each at $\lesssim 3\%$ (Cooke 1991; Dones et al. 1993; Doyle et al. 1989). Spectra reveal that water ice is the predominant constituent of Saturn's main rings and inner moons (see Cuzzi et al. 1984 and references therein); this is assumed to be the composition of the tinier motes as well.

The so-called "spokes" in Saturn's B ring are the primary sites of dust within the main rings (Fig. 4). As Voyager 1 approached Saturn, its cameras detected dark, wedge-shaped radial markings rotating in the B ring, predominantly on the "morning ansa" where the ring material first emerges from Saturn's shadow (Smith et al. 1981; Grün et al. 1983, 1992a; Porco and Danielson 1982). In forward-scattered light the spokes become brighter than the surrounding B ring, thereby exhibiting the characteristic phase function of dust. Because the spokes are so variable in time, their photometric behavior is rather difficult to model photometrically. Nevertheless, Doyle and Grün (1990) used nearly simultaneous images through multiple filters to measure the spokes' col-

ors. They found that the optical depth increases with wavelength, contrary to what one observes in typical dust size-distributions. They concluded that spoke particles need to be rather narrowly confined to sizes $s = 0.6(\pm 0.2)$ μm to be compatible with these measurements. Similar techniques are being applied to HST observations of the spokes (French et al. 1998).

The dynamical properties of the spokes are also quite peculiar. The spokes occupy the radial zone 100 000–116 000 km, straddling the synchronous orbit location at 112 500 km (Smith et al. 1981, 1982; Grün et al. 1983, 1992a). New spokes seem to develop in periods as brief as a few minutes, and are initially radial. Afterward, most spokes propagate at the local Keplerian velocity, so they tilt away from the radial direction as the inner endpoint orbits faster than the outer. However, portions of some spokes have been found to corotate with the planet, while other spokes have been seen to switch from one orbital rate to the other (Grün et al. 1983, 1992a; Eplee and Smith 1984, 1985).

Porco and Danielson (1982) found that spoke activity has a periodicity matching that of the planet's rotation; in addition, more spokes are created when the magnetic sector associated with Saturn's kilometric radiation (SKR) is aligned with the morning ansa. The spoke particles are widely believed to be lifted out of the ring plane (or at least photometrically separated from parent bodies) to make them so visible; however, Grün et al. (1983) place an upper limit of 80 km on this vertical distance. In most of these dynamical properties, the spokes of Saturn's B ring appear to be unlike any other phenomenon observed in any planetary ring system.

3. Saturn's D Ring.   Saturn's innermost (or D) ring has a peculiar history. The experienced observer Guérin (1973) reported first sighting material interior to Saturn's main rings. For the remainder of the 1970's, numerous astronomers attempted to confirm the D ring's existence, with inconsistent results. In 1979, the imaging photopolarimeter on Pioneer 11 did not detect this ring at a level ten times fainter than the Earth-based reports (Gehrels et al. 1980). Shortly thereafter Voyagers 1 and 2, with their more sensitive cameras, did in fact detect a small amount of material interior to the C ring (Fig. 5; Smith et al. 1981, 1982). Thus, although the earlier reports of the D ring were erroneous, this exceedingly faint region has continued to be known as the D ring. It is too faint to be detected by any occultation experiments or Earth-based images, even with our latest technology. Showalter (1996) recently completed the only detailed analysis of the entire D ring data set. The ring is composed of two major narrow ringlets and a set of fainter wave-like structures surrounding them. The narrow rings are radially unresolved (widths $\lesssim$ 40 km) and are centered at 67 580 km and 71 710 km. The ring vanishes from sight at an inner radius $\sim$ 66 000 km; at its outer edge it merely merges into the much brighter C ring. The brightest of the two ringlets could be detected at a broad range of phase angles, so its size distribution was readily modeled by Showalter (1996). The forward-scattering phase function is characteristic of fine dust and is compatible with a relatively flat size distribution ($q \lesssim 2.8$) or else with particles
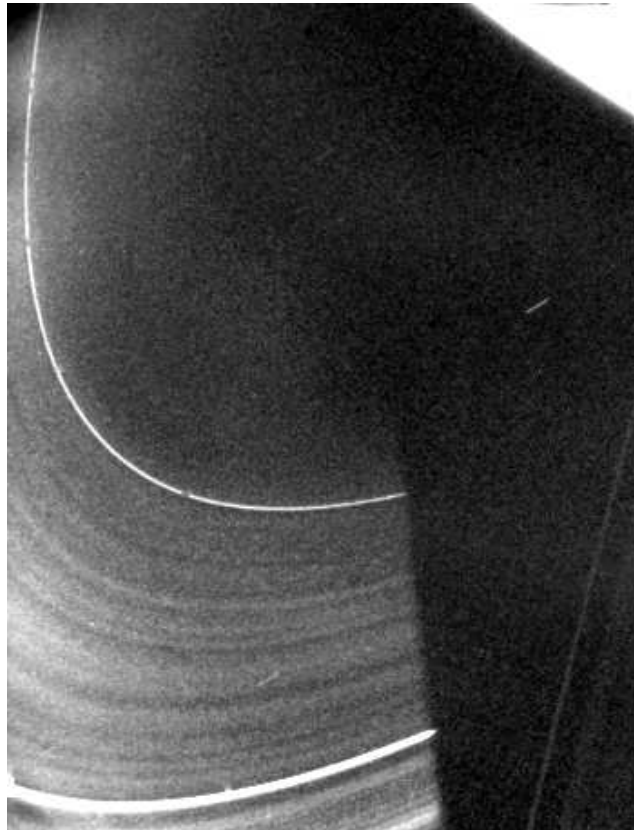
Figure 5. This Voyager 2 image (44007.53) shows the D Ring at a phase angle of 164°. The ring becomes invisible abruptly once it enters Saturn's shadow. Two narrow ringlets, identified as D68 and D72, are surrounded by fainter material which itself contains a great deal of internal structure.

generally larger than ~ 10 μm. Furthermore, an excess of light is definitely detected in backscatter, indicating that macroscopic bodies are present: $f = 89\% \pm 4\%$. The ring has a normal equivalent width of 15 m, so a radial width of ~ 15 km would imply $\tau \approx 10^{-3}$. The D ring's other components were only detected in two images at especially high phase angles (156° and 164°), so their populations are poorly constrained. Surprisingly, however, the ratio of each component's intensity between these two phase angles is highly variable. Although this ratio has no unique interpretation in terms of the dust size distribution, its variations indicate that the dust populations are extremely changeable throughout the D ring. The power-law index q may well range between 2 and 6 within the system.

4. Saturn's F Ring and the Encke Gap Ringlets. Traveling outward, the next major ring to show a preponderance of dust is the narrow, slightly elliptical F ring (Fig. 6), just outside ring A, which is composed of at least four strands
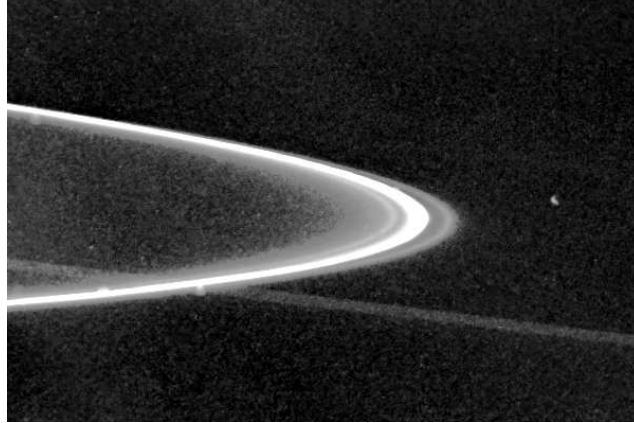
Figure 6.   This Voyager 2 image (44006.49) shows the F ring's ansa and its inner dust
     sheet at a very shallow opening angle of $1°$. Saturn lies just off the left edge of the
     frame. Several of the F Ring's internal ringlets are also visible. The diagonal stripe
     crossing the ring is an artifact of an earlier image.

(Murray et al. 1997). The Ring has an inclination of 0.0067 ± 0.0012 deg (Bash
et al. 2000) and a physical thickness of 21 ± 4 km (Poulet et al. 2000b). Gehrels
et al. (1980) discovered this ring using the imaging photopolarimeter aboard
Pioneer 11, and also noted that the ring was clumpy. The clumpiness was
confirmed and imaged in much greater detail by Voyager's cameras a few years
later (Smith et al. 1981, 1982); the results from various Voyager instruments are
reviewed by Burns et al. (1984) and Mendis et al. (1984). It was, at the time
at least, the archetypical "shepherded" ring, since it appears to be confined by
the two nearby moons Pandora and Prometheus (cf. Goldreich and Tremaine
1979); however, the torques on the ring do not seem to balance as they should
(Showalter and Burns 1982). Furthermore, as measured on HST images taken
during ring plane crossings (Nicholson et al. 1996; McGhee et al. 2000) and
subsequently (French et al. 1999), the orbits of these shepherds are changing
in unexpected ways. High-resolution images from Voyager 1 showed the ring
to hold a variety of surprising internal structures, including strands, kinks, and
the so-called "braids" in addition to the clumps. The braids themselves were
of course illusory, resulting from radial "wiggles" that caused separate strands
to appear to intertwine. Nevertheless, the observed structures continue to
challenge dynamicists almost two decades after the F ring's discovery; unseen,
embedded moonlets may play a pivotal role in the dynamics and variability
of the ring (see Cuzzi and Burns 1988; Murray et al. 1997). Kolvoord et
al. (1990) used Fourier analysis to identify underlying periodicities that are
present in the F ring's longitudinal profile and connected the periodicities with
Prometheus but also a smaller unseen moon. When a moon perturbs a nearby
ring gravitationally, clumps are produced with a characteristic longitudinal
spacing of $3\pi\Delta a$ (Dermott 1981; Showalter and Burns, 1982; Hänninen 1993),

where Δa is the difference between the semimajor axes of the ring and moon.

Showalter (1994, 1998) recently undertook the tedious process of tracking individual clumps in the F ring to see how they evolved over the nine months between the two Voyager encounters. Initial results indicate that the F ring is the most dynamic ring in the Solar System. Clumps appear abruptly, perhaps being produced by impacts of cm-sized interplanetary meteoroids into unseen parent bodies, and disappear over times as brief as days; typical clumps survive for weeks to months. None of the most prominent clumps persisted between the two Voyager encounters. The individual clumps orbit with mean motions that differ by $\sim 0.5°$/day, corresponding to a radial width of 50–100 km. This is comparable to the dimension of the band visible in the most sensitive images and in the PPS profile (Lane et al. 1982).

Observations of Saturn's edge-on rings using HST in May 1995 led to reports of previously undetected moons orbiting just outside the A ring (Bosh and Rivkin 1996). These reports were initially plausible—after all, 13 of Saturn's 18 known moons were discovered during previous ring plane crossings—but the brightnesses indicated that the objects should have been visible to Voyager. The mystery was compounded a few months later when Nicholson et al. (1996) detected additional moon candidates but their positions did not coincide with the May objects. In retrospect, now it is clear that these objects were simply temporary clumps of material in the F ring masquerading as moons. Observations during the Sun crossing in November 1995 settled the issue; under this unique lighting, the F ring was the brightest of Saturn's rings, and numerous clumps could be seen within it (Nicholson et al. 1996; cf. Roddier et al. 2000, Poulet et al. 2000a). The longitudinal distribution of clumps is very reminiscent of that seen 15 years earlier by Voyager; at any given time the ring seems to have 2 or 3 especially bright features plus numerous smaller and fainter ones (Showalter 1998).

Furthermore, Cuzzi and Burns (1988) have studied a set of charged particle absorption signatures near the F ring detected by Pioneer 11, some of which cannot be attributed to known bodies. They infer that a belt of smaller (0.1–10 km) moonlets fills a 2000-km band surrounding the F ring; the additional absorptions can then be explained by microsignatures from temporary clumps of faint debris, arising from collisions within the belt. However, the inferred optical depth of this belt is quite large by the standard of faint rings, $\tau \sim 10^{-4}$– 10^{-3}. Since meteoroid impacts into these bodies and collisions between them will raise clouds of dust continuously, it seems surprising that no broader, fainter band of dust is visible in the Voyager images (see below and Showalter et al. 1998). Some available Voyager images show the much fainter G ring ($\tau \sim 10^{-6}$; see below) but not the dust ring that one would expect from this hypothesized belt.

Photometry by Showalter et al. (1992) indicates that the F ring has a narrow core of relatively high optical depth, surrounded by a skirt composed primarily of dust. This interpretation was based on large-scale longitudinal averaging of the ring images in an attempt to smooth over the variations rep-

resented by the brightness clumps. It also made use of F ring detections by the Voyager PPS and RSS occultation experiments; more recent detections during the 28 Sgr stellar occultation (French et al. 1993; Harrington et al. 1993; Hubbard et al. 1993) have not yet been incorporated in ring photometry, but have been used to define the orbital shape (see Murray et al. 1997). Using an occultation observed by HST's Faint Object Spectrometer, Bash et al. (2000) conclude that the F ring's equivalent depth has no significant dependence on wavelength (0.25-0.74 μm), implying ring particles are greater than s $\sim$ 10 μm. In general terms, the size distribution does not seem to vary radically between the F ring's brightest clumps and its fainter regions; however, more subtle variations may well have been overlooked in the analyses performed so far. The dust appears to obey a rather steep power-law distribution, with $q = 4.6 \pm 0.5$. Interestingly, this phase function matches the ring in backscatter as well as forward-scatter, which severely limits the macroscopic population to $1 - f \lesssim 2\%$. However, a very narrow feature found in the RSS occultation (Tyler et al. 1983) presumably indicates a direct detection of a core of parent bodies. At visual wavelengths, the ring's normal equivalent width is 5.0 ($\pm$ 0.3) km. Poulet et al.'s (2000b) best model to explain thickness measurements during ring-plane crossing has a radial $\tau \sim 0.20$ and a dust fraction f > 0.80.

The F ring's color in HST images is neutral or slightly blue, like its inner shepherd, but unlike Pandora whose color is red, like the main rings (Poulet et al. 1999). Several long exposures at high phase angles reveal a faint inward extension to the F ring (Fig. 6), which is present throughout the entire gap down to the A ring. Burns et al. (1983; cf. Fig. 1 of Murray et al. 1997; Nicholson et al. 2000; Showalter et al. 1998) estimate $\tau \sim (1-2) \times 10^{-4}$, with the large uncertainty caused by the dearth of data. Careful analysis of the Voyager PPS data set showed some baseline variations near the F ring, which Graps et al. (1984, see also Graps and Lane 1986) attributed to fainter ring material. However, the inferred τ of this material is $\sim 10^{-2}$, which is much too large to be compatible with the images. It appears, in retrospect, that these features arose from background variations in the PPS instrument rather than from actual "unseen" ring material; nevertheless, after checking the instrumental light variations, Graps (private communication, 1995) maintains her original interpretation.

The nearest dynamical and physical analog in Saturn's rings to the F ring is a pair of narrow ringlets (see Fig. 19 in Cuzzi et al. 1984) orbiting within the Encke Gap, an opening 320 km wide in the outer third of Saturn's A ring. The gap is apparently shepherded open by the small moon Pan (Showalter 1991), orbiting at 133 583 km near the gap's middle. Two variable ringlets can be seen in the images, one near the inner edge and the other near the center; this latter ringlet appears to occupy the same orbit as Pan itself. The ringlets also appear to be incomplete, since each one is prominent in some images but absent in others, even when the phase angle and spatial resolution are unchanged.

Photometry of these ringlets is extremely difficult owing to their marked variations. Nevertheless, the ringlets brighten significantly at high phase angles
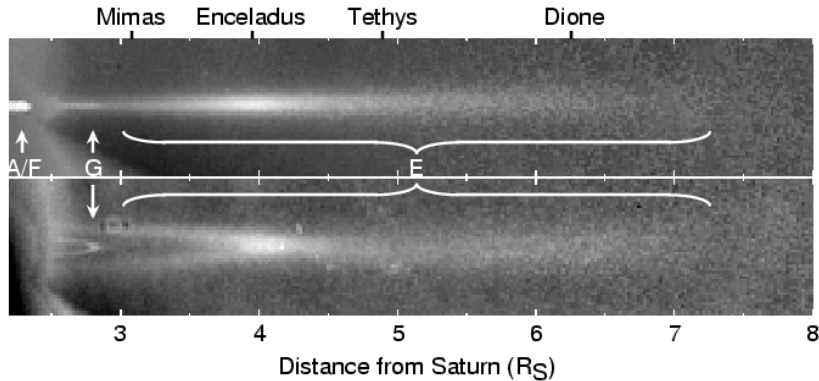
Figure 7. Two HST images that depict Saturn's outer rings: i) when the rings were
nearly edge-on (top, taken on 9 August 1995) and ii) viewed from an elevation
of about 2° (bottom, taken on 28 November 1995). At the left of the top image,
the outermost A/F rings are over-exposed. The G ring is seen to be narrowly
confined whereas the E ring, peaking at Enceladus' orbit, extends across many
satellite paths. The orbital positions of several satellites, as measured at each
frame's center, are shown at top. In order to bring out the G ring from the glare
of the main rings, a smooth background has been subtracted. Follows Nicholson et
al. (1996).

implying a prevalence of dust (Showalter 1991). Neither ringlet appears in
the RSS data, but the middle one is visible in the PPS profile. It has a peak
$\tau \approx 0.1$ and a radial width of $\sim$ 20 km; its equivalent width is $\sim$ 1 km. In
these properties it is quite comparable to the F ring although, given the ring's
marked variations, one cannot know if this section of the ring is atypical. The
ringlets have not been detected in Earth-based occultations.

5. Saturn's G Ring.   Continuing outward, Saturn has two other very faint
rings, designated G and E (Fig. 7). Interest in these two rings has been rekin-
dled recently because of the potential hazard they may pose to the Cassini
orbiter, scheduled to arrive at Saturn in 2004 (Cuzzi and Rappaport 1996).
Cassini will need to pass repeatedly through, or very close to, both of these
rings during its four-year tour. Significant new Earth-based observations of
these outlying rings were acquired during the Saturn ring-plane crossings of
1995-96 (Bauer et al. 1997; de Pater et al. 1996; Nicholson et al. 1996).

The G ring is tenuous ($\tau \approx 10^{-6}$), relatively narrow and centered on orbital
radius 168 000 km, far from any other known ring or moon. In Voyager obser-
vations its radial width is $\sim$ 7 000 km, between 166 000 and 173 000 km, with
no apparent internal structure beyond an inverted "V" profile, in which the
ring brightness decays linearly both inward and outward from a central peak
(Showalter and Cuzzi 1993; Throop and Esposito 1998). In HST observations
(Nicholson et al. 1996) the G ring is roughly uniform in brightness, with a full
radial width of 8 000 ($\pm$2 000) km, with half-flux points at 166 000 and 170 000
($\pm$1 000) km. Its thickness is < 1 300 km. The earliest evidence for this ring
was acquired by Pioneer 11 in 1979, when it detected a high-energy charged

particle absorption signature in the region, that was variously attributed to a new satellite or perhaps to Janus (Simpson et al. 1980; Van Allen et al. 1980). It was later recognized as a ring in only two Voyager images, both at the same high phase angle $\alpha \simeq 160°$. Showalter and Cuzzi (1993) managed to identify it marginally at three other phase angles, yielding a crude phase function. From the four-point phase curve, Showalter and Cuzzi (1993) inferred that the dust size distribution is surprisingly steep, with $q \approx 6.0 \pm 0.2$. This means that the ring's light-scattering is dominated by extremely tiny particles, $s \sim 0.03$ μm.

The G ring was also detected by Voyager's unintended "dust detectors," the PWS and PRA instruments. Showalter and Cuzzi (1993) found that Voyager 2's crossing radius was 172 124 km plus or minus a few km, near but distinctly inside the G ring's outer boundary. Thus, the PWS and PRA noise can be interpreted as direct, *in situ* measurements of the G ring's particles (Aubier et al. 1983; Gurnett et al. 1983; Tsintikidis et al. 1994; Meyer-Vernet et al. 1998). The final interpretation of these data indicates $\tau \approx 10^{-6}$, particles of radii a few microns, $q < 3.5$ and a ring thickness of $\sim 1\,000$ km. The issue of q is not resolved since Showalter and Cuzzi's steep distribution was supported by modeling of the PWS data set by Gurnett et al. (1983; cf. Tsintikidis et al. 1994), although these data are only sensitive to grains in the size range 0.5–5 μm, but not by Meyer-Vernet et al.'s (1998) PWS interpretation.

On the other hand, recent Earth-based images (Nicholson et al. 1996; de Pater et al. 1996; Bauer et al. 1997) reveal the G ring to be neutral to slightly red in color, whereas the color of Showalter and Cuzzi's steep distribution is expected to be blue in backscatter. This seeming contradiction has not yet been reconciled. Throop and Esposito (1998) present a range of particle size distributions in an attempt to satisfy this discrepancy, and favor a power-law q between 1.5 and 3.5. Both Canup and Esposito (1997) and Throop and Esposito (1998) demonstrate that such a size distribution may develop following the disruption of a progenitor satellite.

Regarding the larger particles from which the dust is derived, Van Allen (1983, 1987) modeled the Pioneer 11 absorption signature to demonstrate that the G ring comprises a total cross-section of (10–40) km^2 in bodies larger than 25 cm, the distance needed to stop a high-energy proton Thus, the absorption signature is likely to serve as a direct detection of the parent population within the ring. However, this population corresponds to $\tau \sim 10^{-8}$, much too small to be visible in the images; the G ring's dust therefore dominates its light-scattering at all phase angles. This result is consistent with Hood's (1989) modeling of the absorption signature, which suggests that the parent bodies are confined to a band $\leq 1\,000$ km wide, much narrower than the visible ring.

6. Saturn's E Ring.   The outermost of Saturn's bands, the E ring (Fig. 7), spanning the orbits of Mimas, Enceladus, Tethys and Dione, encompasses an area and a volume larger than those of all other planetary rings put together. This ring was discovered during the 1966 crossing of Saturn's ring-plane (Feibelman 1967) and observed again from Earth during the 1979-1980 and 1995-96 crossings, with substantial improvements of data quality on each occasion. In

addition, both Voyagers imaged the E ring, although the few available images are confined to three narrow ranges of phase angle. Two dust impacts were recorded in this region by the Pioneer 11 detector (Humes et al. 1980).

The properties of Saturn's E ring were reviewed by Showalter et al. (1991) based on the Voyager and pre-1995 Earth-based data. The ring has a distinct peak in brightness near the orbit of Enceladus (Fig. 7), which likely serves as a source for the ring dust in some manner (Hamilton and Burns 1994). The ring is vertically thick compared to most rings, ranging from $\sim$ 6,000 km near its inner limit to $\sim$ 20,000 km near its outer edge; however, it appears to narrow significantly about the orbit of Enceladus. Roddier et al. (1998) claim to have seen a short-lived arc within the E ring, near one of Enceladus' triangular Lagrange points.

The ring is exceedingly faint, with a peak $\tau \sim 10^{-5}$. Several of its photometric properties, including a peculiar blue color in backscattered light (Larson 1984) and a sharp diffraction peak near forward-scatter, led Showalter et al. (1991) to the unexpected conclusion that the ring dust does not obey a power-law size distribution. They found that a narrow size range centered near $s \approx 1$ μm provides the best fit to the available data.

Testing this surprising conclusion was a high priority for the 1995-96 E ring observations from Earth. In general, the old model of the ring's properties held up quite well after the influx of new, higher-quality data. The ring's expanding thickness with radius, plus its local thinning near the orbit of Enceladus, appeared quite clearly in images from HST (Nicholson et al. 1996). Images spanning wavelengths from the infrared to the ultraviolet confirm the ring's distinctive blue color (Nicholson et al. 1996; de Pater et al. 1996; Bauer et al. 1997). This color, when combined with the Voyager measurements, remains incompatible with any power-law size distribution. Although further refinements to the photometric models are needed, it is clear that the size distribution in the E ring is unlike that in other known rings.

Tsintikidis et al. (1995) and Meyer-Vernet et al. (1996) have re-examined PWS and PRA measurements from Voyager 1, which passed through the E ring at $a \sim 368\,000$ km, near the orbit of Dione. Like their Voyager 2 counterparts (Tsintikidis et al. 1994; Oberc 1994), both instruments detected impulsive noise near the ring plane, which can now be attributed to impacts with E ring dust. Meyer-Vernet et al. inferred that the particle size distribution is narrowly peaked near $s \approx 1$ μm, in close agreement with Showalter et al. (1991). However, Tsintikidis et al. inferred $s \approx 5$ μm, a significant discrepancy that has not yet been explained (see Cuzzi and Rappaport 1996). Meyer-Vernet et al. measured the ring's thickness as 12 000 km, comparable to the value in the images. However, they reported a southward offset to the density peak by 5 000 km, something not observed by others.

7. Uranus' Ring System. The nine main Uranian rings are designated, in order of increasing radius, rings 6, 5, 4, α, β, η, γ, δ, and ϵ. All are very narrow; ring ϵ is the broadest with a width ranging between 20–100 km, while every other one is $\lesssim$ 10 km wide. Optical depths are generally of order 0.1-1.0.
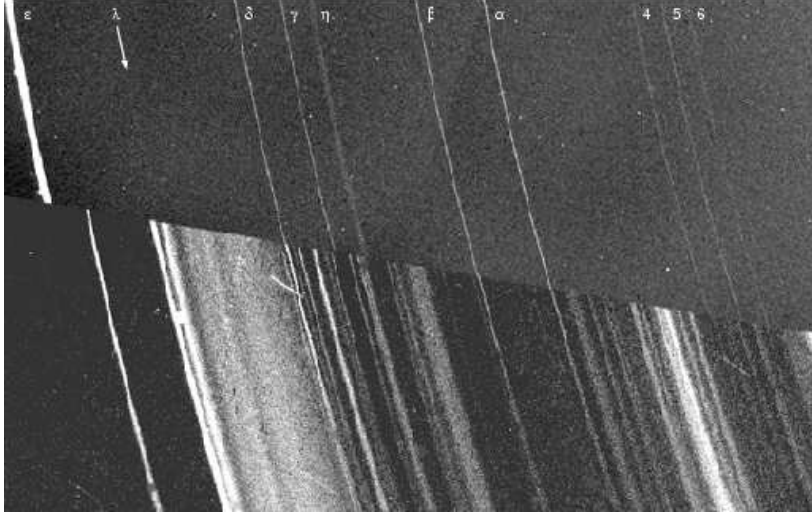
Figure 8. Compare these images of the Uranian ring system. Voyager 2 acquired the
upper one the day before it passed Uranus in January 1986; at the time sunlight
striking the ring particles was reflected back toward the camera (phase angle of
18°). In the lower image, taken somewhat later, the spacecraft was looking almost
directly back toward the Sun (phase angle of 172.5°). This backlighting of the rings
dramatically enhanced the visibility of any micrometer-sized dust particles that the
rings contain. The nine narrow rings discovered in ground-based occultations (note
the poor segment match for the markedly eccentric ϵ ring) can be readily discerned;
they are surrounded by dust belts containing a great deal of internal structure. The
λ ring, so bright in forward-scattered light, is only visible in the top frame if you put
your eye close to the bottom and look toward the arrow. The short linear streaks in
the bottom frame are background stars that smeared during the 96-sec exposure;
even the rings themselves are smeared somewhat, especially near the bottom of the
frame. Courtesy of J. Kelly Beatty.

As with Saturn's denser rings, these rings show very low dust content;
Ockert et al. (1987) inferred $f \lesssim 0.2\%$. French et al. (1991) and Esposito et
al. (1991) review these rings' properties.

One additional narrow ring, λ (1986U1R), was discovered in images as
Voyager approached Uranus (Smith et al. 1986). Unlike the other narrow rings,
this one brightened substantially in forward-scatter, indicating the presence of
dust. In a single image (Fig. 8) acquired at a very high phase angle ($\alpha \sim 173°$),
it is the brightest of Uranus' rings. Photometry by Ockert et al. (1987) revealed
this ring to have significant longitudinal variability. Showalter (1995) used
additional images to determine that these variations are generally periodic, so
that the ring could be better viewed as a set of five uniformly-spaced arcs. This
makes the λ ring one of the few rings with known longitudinal variations, and
the only one in which a single periodicity dominates.

By accounting for these variations in his modeling, Showalter (1993) at-
tempted to infer that ring's size distribution and dust fraction. Using four
phase angles and also τ measurements at four wavelengths (UVS, PPS, RSS

3.6 cm, plus an image measurement where the ring was backlit by the planet), he arrived at an interesting contradiction. A strong wavelength dependence to τ required a steep power law, with $q > 3.5$. On the other hand, the shape of the diffraction peak near forward-scatter required a flatter distribution, with $q < 3$. This led him to the conclusion that at least three different populations are necessary to model the size distribution: a steep "submicron" population to account for the τ dependence, a flatter "micron" population for the phase curve, and finally the usual macroscopic population to explain the backscatter. The best-fit model involved $f \approx 75\%$, with the dust evenly split between the two populations.

Aside from ring λ, the Uranian system contains additional dust distributed widely in radius. At high phase (our Fig. 8, and Figs. 11 and 12 in Esposito et al. 1991) the Uranian system is seen to contain an extraordinary family of dust belts and gaps around and among all the better known narrow rings. Radial structure is visible at a variety of scales from 50 km to $> 1\,000$ km, with the lower limit set by the image's resolution. Unfortunately, these dust belts only appear in this single image, so detailed inferences about their optical depths and particle sizes are not possible. Murray and Thompson (1990) have attempted to connect the orbital distribution of this material to unseen shepherd satellites.

One additional broad ring, designated 1986U2R, is visible in a lone Voyager image at a $90°$ phase angle. This ring is interior to all of the structure discussed above, with a peak at a radius of $38\,000$ km and a radial width of $\sim\ 5\,000$ km. Once again, very little can be determined about the particle properties of this ring from a single view, although a predominance of dust is strongly suspected.

Although no other rings were seen by the Voyager cameras, the PWS and PRA instruments again detected dust impacts during the ring plane crossing at $a \sim\ 118\,000$ km, which is inside the orbit of Miranda but well outside the orbits of the Voyager-discovered moons and rings (Meyer-Vernet et al. 1986; Gurnett et al. 1987). Particles are inferred to be microns in size and have total $\tau \sim 10^{-8}$–10^{-7}. Such a faint ring would not have been visible to the cameras. The data seem to disagree about the thickness of this unseen ring; Meyer-Vernet et al. infer a thickness of 150 km in the PRA data, whereas Gurnett et al. believe $3\,500$ km from the PWS. A difference in particle-size sensitivity seems unlikely to explain fully this discrepancy.

8. Neptune's Ring System.   After the 1977 discovery of the Uranian rings by stellar occultations, Neptune's environs were searched for analogous narrow rings. Initial results were negative, except for a very fortuitous detection of the tiny moon Larissa by Reitsema et al. (1982). However, in 1984 Hubbard et al. (1986) detected an occultation event on one side of Neptune that was not repeated on the other, suggesting that incomplete arcs might be orbiting the planet. Subsequent occultation observations reported occasional events, but it took the closeup images from Voyager 2 in 1989 to settle the issue: 3–5 slender and discontinuous ring arcs are embedded within a narrow, fainter Neptunian ring (Smith et al. 1989).
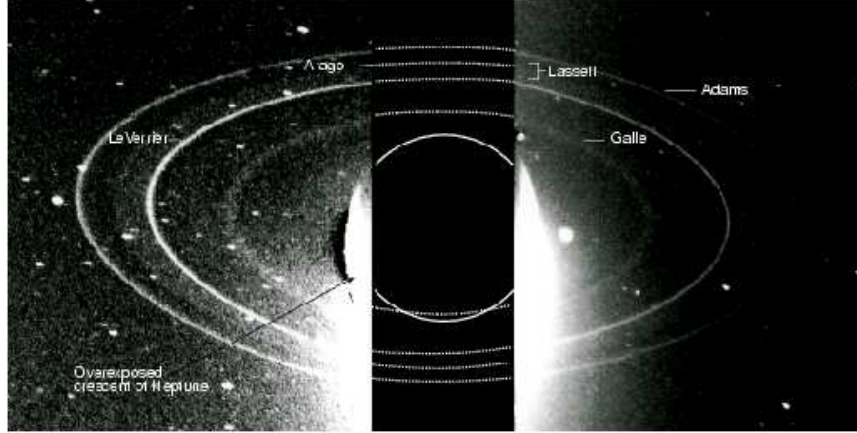
Figure 9.   All of Neptune's major rings are visible in this outbound image from Voyager 2 (11446.21) at a phase angle of 134°. The outermost ring is Adams, whose arcs are not visible here. LeVerrier is the other bright ring, and Lassell is the faint band extending half way out to Adams. The faint inner Galle Ring is also visible. The many bright spots are background stars.

Based on the Voyager images (Fig. 9), Neptune's ring system is now known to comprise several distinct components(Fig. 1). The most prominent narrow ring is Adams, at $a \approx$ 62930 km, with a radial width of ~ 20 km. A 40° segment of this ring contains the aforementioned arcs, now designated Courage, Liberté, Egalité 1 and 2, and Fraternité (Fig. 10). In the images with finest resolution ($\sim$ a few km per pixel) the arcs are composed of much smaller discrete clumps. By comparing these visible arcs with the longitudes of Earth-based detections, Sicardy et al. (1991) and Nicholson et al. (1995) established that these arcs have been stable from the time of their discovery in 1984. Outside the arc region, Adams varies rather little in brightness; however, Showalter and Cuzzi (1992) found that it is faintest at the longitude opposite to the arc region and brightens as the arc region is approached in either direction. At its minimum, the Adams ring is only 10% as bright as it is in the arcs.

A second narrow ring, LeVerrier, falls at $a \approx$ 53 200 km. It is in all respects similar to Adams except for the absence of arc-like structures. A fainter, uniform ring named Lassell extends outward from LeVerrier about half-way to Adams, ending at $a \approx$ 58 000 km. A slight increase in Lassell's brightness at its outer boundary has, perhaps unwisely, been given a different name, Arago. Finally, a much broader ring named Galle has a peak near $a \approx$ 42 000 km and probably reaches all the way down to the planet (Showalter and Cuzzi 1992). Porco et al. (1995) provides a much more detailed review of these rings.

Interspersed among these rings are a number of small moons (Fig. 1). Galatea orbits just inside the Adams ring and its gravitational perturbations are likely to play a significant role in the arcs' confinement (Porco 1991; Horányi and Porco 1993; but see Sicardy et al. 1999; Dumas et al. 1999). Despina traverses just inward from the LeVerrier ring, while Thalassa and Naiad occupy
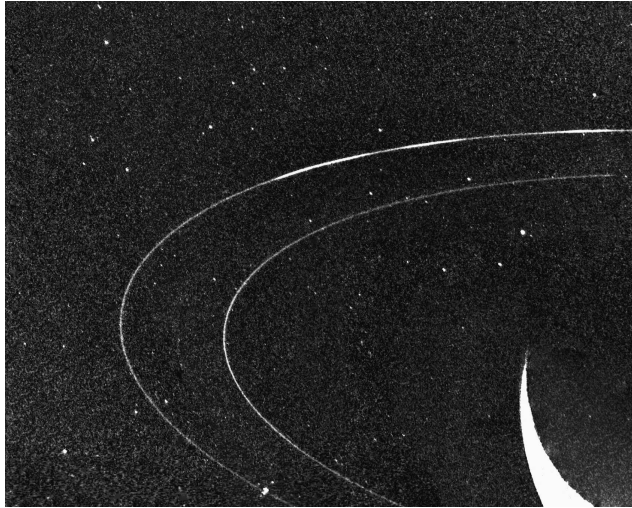
Figure 10.   A long-exposure, forward-scattered image (phase angle of 134°) of Nep-
    tune's outer two rings shows that the ring arcs are in fact clumps of material within
    the outermost (Adams) ring, which is less than 50 km wide; the LeVerrier band is
    about 110 km across. In this image, the direction of orbital motion is clockwise,
    with the longest arc (Fraternité) trailing. Neptune's over-exposed crescent is at
    lower right.

the gap between the LeVerrier and Galle rings. Interestingly, Galatea shares
its orbit with a faint and possibly incomplete dusty ringlet (recall the Encke
ringlet and Pan), but the other moons do not.

Voyager imaged the rings at only four narrow ranges of phase angle near 8°,
15°, 135° and 155°; furthermore, the longitudinal coverage at the two extremes
is very limited. Nevertheless, all of Neptune's rings have been found to brighten
at higher phase angles, indicating that they are dusty. Additional detections of
the arcs in PPS and UVS stellar occultations, plus Earth-based occultations at
$\lambda \approx 2.2 \ \mu$m, serve as direct probes of τ; arc equivalent widths are typically ~ 1
km; given the radial widths of ~ 20 km, this yields τ values of several percent
(Horn et al. 1990). Unfortunately, the RSS occultation profile missed the arc
region of the Adams ring and nothing was sensed (Tyler et al. 1989). In fact,
except for the arcs, the Adams ring has never been detected via occultation,
and only very marginal detections of the LeVerrier ring have been reported
(Horn et al. 1990, Nicholson et al. 1995). The best Earth-based data sets have
placed rather strict upper limits on the equivalent widths of these narrow rings
(Sicardy et al. 1991; Nicholson et al. 1995).

Owing to the very limited data, inferences about the composition and sizes
of Neptune's ring particles are subject to major uncertainties. Nevertheless it is
clear that Neptune's rings are significantly dustier than the main rings of Saturn
and Uranus. Showalter and Cuzzi (1992) and Ferrari and Brahic (1994) have
performed independent analyses; Porco et al. (1995) thoroughly summarize
and tabulate the dust observations. Measurements at the two high phase angles

show that dust properties vary among the rings, and possibly also among the different arcs. Power–law indices $q \approx$ 2–4 are generally implied. Although no ring images were acquired through Voyager's color filters, Showalter and Cuzzi inferred that the Adams ring is very red, using the slightly different passbands of the clear filters on the wide- and narrow-angle cameras. This red color would tend to favor $q < 3$. All photometric models reveal that the dust distribution is inadequate to account for the rings' backscatter I/F, indicating a significant presence of parent bodies. Accepting a broad sweep of assumptions, $0.2 \leq f \leq 0.7$ in the Adams and LeVerrier rings (Smith et al. 1989).

Ferrari and Brahic (1994) suggest that a less dissipative, "dirty ice" composition provides the best fit to the ring photometry. Nonetheless, others have assumed amorphous carbon because this is more consistent with the exceedingly dark surfaces of Neptune's inner moons. Porco et al. (1995) present a method to infer the geometric albedos of the ring particles and find values of 5–7%, comparable to those of the inner moons (Thomas et al. 1995).

As at Uranus, dust impacts were recorded by the PWS and PRA instruments, revealing the presence of a far more widely separated dust population well outside the rings (Gurnett et al. 1991; Pedersen et al. 1991). Ring-plane crossings were at $85\,290$ km and at $103\,950$ km. Inferences from the PWS and PRA data sets are not in perfect agreement, as demonstrated by Table III of Porco et al. (1995). Nevertheless, it is reasonable to conclude that this faint cloud consists of dust a few μm in size with $\tau \sim$ a few $\times\ 10^{-6}$. Furthermore, the cloud is hundreds of km thick and is not centered on the equatorial plane; measured offsets were $\sim$ 150 km northward on the first crossing and $\sim$ 800 km southward on the second; these perhaps merely reflect the position of the warped Laplace plane (Porco et al. 1995). Among the more interesting circumplanetary dust findings are reports by both the PWS and PRA teams of the presence of considerable dust at high latitudes.

Charged–particle absorption signatures have been identified in data from Voyager's low-energy charged particle experiment (Mauk et al. 1991, Paranicas and Cheng 1991). However, Neptune's substantially inclined magnetic field caused Voyager to cross in and out of L shells repeatedly, hindering a straightforward interpretation of these results.

III. PHYSICAL AND DYNAMICAL PROCESSES ACTING ON CIRCUMPLANETARY DUST

As a prelude to looking at the forces that act on the constituents of dusty planetary rings, we first mention that dust motes will be electrically charged. Then we consider some of the forces that act on circumplanetary particles, including electromagnetic forces, radiation pressure, gravity, and various drag forces that cause orbital evolution; typical accelerations due to these forces acting in various ring systems are tabulated. In the middle of this section we describe various processes, including the generation and destruction of grains, interactions with parent bodies, likely size distributions and resonance pro-

cesses; it lists the resultant timescales. The end part of this section discusses the dynamics of particles that are subject to such forces.

A. Electrical Charging

Because objects in space are bathed in plasma and struck by ultraviolet photons, they acquire net electrical charges. The precise charging history for any grain depends on the grain's properties (composition, size and surface character) and on the ambient environment (plasma composition, number density and temperature, plus radiation flux); it also varies according to the grain's past since charging by any process does not occur instantaneously and since, in rare instances, more than one equilibrium state exists (Meyer-Vernet 1982).

To compute the electrical charge q, one tallies the current flows to the grain which, for Maxwellian distributions, are given by Goertz (1989), Northrop (1992), Mendis and Rosenberg (1994), Schaffer and Burns (1995), and Horányi (1996). Usually the grain's charge q is taken to be its equilibrium value, i.e., the charge at which, on average, no net current flows to the grain.

Two limiting cases of electrical charging are instructive. First, consider an isolated grain in vacuum; it will expel photoelectrons when exposed to energetic ultraviolet photons. The loss of these electrons means that the grain becomes positively charged; subsequently, the only photoelectrons that are able to escape are those whose kinetic energies are sufficient to overcome the surface electric potential. Of course, whenever a larger charge develops, a smaller fraction of the ejected photoelectrons have sufficient energy to fully escape the surface. Since photoelectrons exit with energies similar to the work function of the surface material, the equilibrium potential is roughly that work function, or a few volts positive. This limiting case applies to interplanetary dust and circumterrestrial grains where photoelectron currents dominate charging; in such a circumstance, an immediate corollary is that passage through the planetary shadow, where the primary current is absent, will have measurable consequences (cf. Horányi and Burns 1991). However, because the solar flux density decays quadratically with heliocentric distance, photo-charging is less relevant in the outer solar system. Instead, plasmas play the major role in the charging of grains. Each of the giant planets is shielded from the onslaught of the solar wind by a substantial planetary magnetic field that, in the planet's neighborhood, traps magnetospheric plasma.

The second heuristic example considers just ion and electron thermal currents to be present. If a neutral grain is placed in a plasma where, owing to energy equipartition, both components have the same kinetic temperature T, the particle at first will be struck primarily by the less-massive, swifter-moving electrons. As a result, a negative charge will build until the particle's electric potential becomes sufficient to attract enough positive ions to counterbalance the somewhat-repelled electrons. Thus, a particle embedded in a plasma should develop an electric potential ϕ (in eV) like the plasma temperature. In a clas-

sical result, Spitzer (1962) found that

$$\phi_{eq} = -\frac{bkT}{e} \ , \tag{5}$$

where k is the Boltzmann constant, e is the magnitude of the electron charge, and b is a constant that depends on the ion species; typical values are $2-4$. We note that this result, like that for purely photoelectric charging, is independent of particle size.

This treatment is inadequate once the grain moves appreciably with respect to the mean plasma, in which case the currents need modification. What are typical speeds? Slightly charged dust circles the giant planets at nearly the Keplerian speeds, of order tens of km·sec^{-1}. To a very good approximation, magnetospheric plasma near the planet is tied to (and co-rotates with) the planet's magnetic field (Stern 1976); it therefore orbits at speeds ranging from tens to hundreds of km·sec^{-1}, varying linearly with radial distance to the planet's center. Synchronous orbit is located at the radius r^* where a particle's circular orbital period matches the planet's spin period, or

$$r^* = \left(\frac{4\pi G\rho}{3\omega^2} \right)^{\frac{1}{3}} R_p \ , \tag{6}$$

where G is the gravitational constant, ρ is the planet's density, ω its spin rate, and R_p its mean radius. At other radii, uncharged grains drift relative to the plasma; their speeds vary linearly with r^*-r at small and very large r^*-r with typical values ranging up to many tens of km·sec^{-1}. Because electron thermal speeds (for plasma temperatures in typical magnetospheres of ~ 10 eV) are $\sim 10^3$ km·sec^{-1}, the relative drift scarcely alters the electron flux; in contrast, ion thermal speeds are ~ 10 km·sec^{-1}, comparable to the plasma drift, and thus ion fluences may become quite anisotropic; the effect of a grain's charge on current fluences is given by Northrop and Birmingham (1990). At low relative speeds, the positive ion flux is reduced (because Coulomb attraction is less effective at focusing ions), allowing the equilibrium charge to become more negative (cf. Fig. 1 of Burns and Schaffer 1989); eventually at higher relative speeds, ions are rammed onto the grain and the grain's charge grows less negative, linearly with relative speed.

The above calculations are idealized in many regards: i) they assume spherical dust grains despite the expectation that circumplanetary grains will be ejecta fragments or convoluted aggregates, like captured interplanetary dust particles; ii) they consider that all impacting ions/electrons stick on hitting the target, yet some will actually pass totally through and others will be scattered; iii) they take the plasma to contain a single species and to be Maxwellian, contrary to evidence from space probes (Mendis and Rosenberg 1994 also discuss a Lorentzian distribution); iv) they neglect changes to ion and electron currents imposed by local B–fields; and v) finally, secondary electron emission,

most important at higher electron energies (> 50eV), is ignored. In the latter process, bombarding electrons penetrate the target, ionizing some material, after which the liberated electrons diffuse out to the surface; as emphasized by Horányi (1996), the ratio of emitted secondary electrons to incident ones varies sharply with the target's properties and the primary electron's energy, reaching a maximum (a factor of several) when the primary electrons penetrate to depths that are comparable to the target's size.

According to the above discussion, a grain's charge will vary as a grain moves about a planet owing to passage into/out of planetary shadows, non-uniform plasma conditions, and relative velocity changes due, for example, to a noncircular or nonequatorial orbit. Therefore, all three of these effects cause the particle's charge to oscillate with the orbital period; thus to some degree all electromagnetic forces, by their very nature, resonate with the orbital motion and accordingly can profoundly alter the orbit. These evolutionary changes are discussed in the Resonance section below.

It is instructive to realize that the number of excess charges corresponding to typical equilibrium potentials on micron-sized grains is not very large: since the potential $\phi = q/s$, the number of extra charges on an isolated spherical grain can be expressed as

$$N \simeq 700 (\frac{\phi}{\text{Volt}})(\frac{s}{\mu\text{m}}) \; . \tag{7}$$

Because individual plasma particles carry quantized charges and arrive at random but specific times, the charge carried by circumplanetary dust fluctuates stochastically. Schaffer and Burns (1995), by modeling grain-charging as a Markov process, compute the distribution functions to have half-widths of $0.5N^{1/2}$. Thus, the typical fractional charge variation for our nominal 1μm grain in a hydrogen plasma is about 1%. Such a slight jittering of charge, and indeed relatively much larger variations, have minimal effects on orbital resonances (Schaffer and Burns 1995).

Somewhat counter-intuitively, smaller grains take longer than large to achieve equilibrium charges: this occurs because, from (7), the equilibrium charge $q \sim s$, while the currents that lead to this charge are proportional to the grain's surface area or $\sim s^2$; thus the charging time $\sim s^{-1}$. For grains of 1μm radius and typical plasma conditions in the outer solar system, the time to reach equilibrium is 10 to 10^3 sec, much less than the orbital periods of 10^4 to 10^5 sec (Schaffer and Burns 1995). Once charging times become comparable to dynamical timescales, say for 0.1 μm grains or smaller, significant energy and angular momentum can be exchanged between the grain and the magnetosphere. In turn these changes may produce profound orbital modifications (Burns and Schaffer 1989; Northrop et al. 1989; Colwell et al. 1998).

An important issue related to charging is whether the grains may be considered to be "isolated" individuals or whether they form an organized ensemble to repel the bombarding plasma. In the latter case, charges will be significantly reduced (Grün et al. 1984; Mendis et al. 1984; Goertz 1989). Collective

effects must be considered if the typical spacing between particles $d \ll \lambda_D$, the Debye length, which is the distance over which the charge in a plasma is effectively shielded. Goertz (1989) used nominal values of the mean particle size and optical depth to argue that charges are significantly overestimated for the F ring, most Neptunian ring arcs and the spokes. Hartquist et al. (1994) disagree. Goertz et al. (1988) have suggested that electrostatic repulsion may inflate ring thicknesses and, under some circumstances, may lead to a Coulomb lattice in which the grains form a regular array held apart electrostatically.

The general subject of collective effects in dusty plasmas– e.g., waves, instabilities, and wave scattering – has a rapidly expanding literature, much of it not concerning solar system or astrophysical studies; the reviews by Northrop (1992), Hartquist et al. (1994), Mendis and Rosenberg (1994), and Bliokh et al. (1995) provide introductions to the field. Havnes, Morfill, Goertz and their co-workers have proposed that several periodic features in the rings are associated with various instabilities. Goertz et al. (1986) have maintained that submicron dust particles sporadically elevated above Saturn's rings induce angular momentum exchange between the ring and the planet. Goertz and Morfill (1988) argue that this process leads to a radial instability in the ring.

The shape and size distribution of dust grains may be affected at high enough charges. Particles will be disrupted once their strength is unable to withstand electrostatic repulsive stresses; since the electrostatic tension is inversely proportional to the local radius of curvature, surface asperities will become rounded (Burns et al. 1980, 1984, Grün et al. 1984, Mendis et al. 1984, Mendis and Rosenberg 1994). Since most grains have like (negative) charges, the processes of nucleation and coagulation are generally inhibited by Coulomb repulsion (Mendis and Rosenberg 1994). However, small grains occasionally achieve positive potentials (cf. Meyer-Vernet 1982), in which case growth rates accelerate.

Most studies of the electrical charging of circumplanetary dust consider, as we have just discussed, currents to arrive from magnetospheric plasma or photoelectrons. Horányi and Cravens (1996) suggest that jovian ionospheric plasma may play an important role in the charging of members of Jupiter's rings, vastly accelerating the evolution of individual grains.

B. Forces

Since, by definition, circumplanetary dust is small and therefore has a large area-to-mass ratio, it is significantly affected by some forces that are much less important for bigger bodies. We first consider individual ring particles larger than a micron or so in size, typical of circumplanetary dust. By far the dominant force acting on such grains arises from the point-source gravity of the central planet, but several other forces perturb the orbits of these particles; in contrast to the planet's gravity, the latter may change the particle's energy and/or angular momentum and thereby modify the orbital character (Burns 1976).

The strongest gravitational perturbation is from the planet's non-spherical
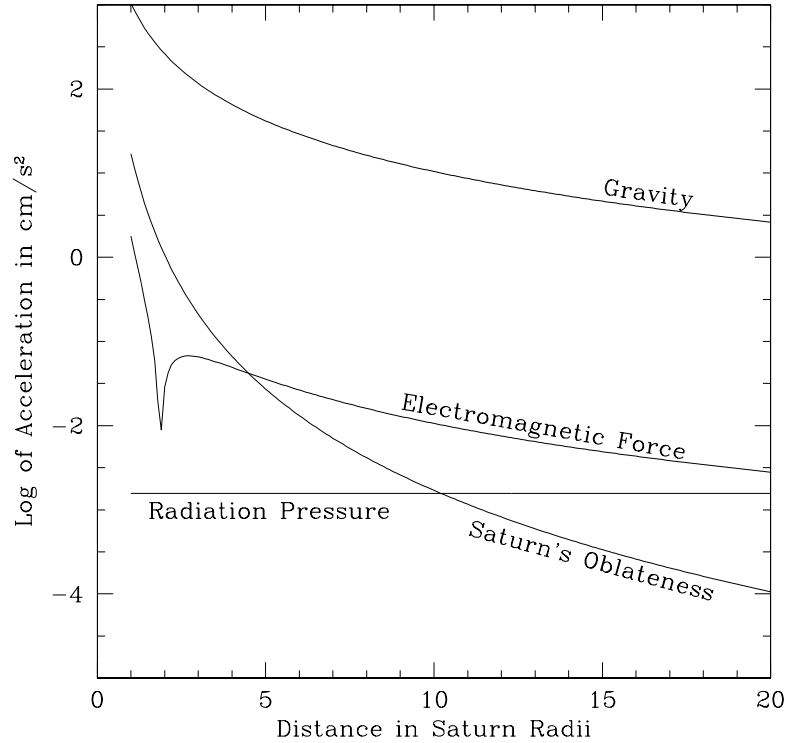
Forces on a 1.0 Micron Grain near Saturn

Figure 11. The strength of some perturbation forces around Saturn for a totally ab-
sorbing ($\beta = 1$) 1μm dust grain charged to -5V. The electromagnetic force vanishes
at synchronous orbit where the grain's velocity relative to the magnetic field is zero.

shape, since most rings are located within a few planetary radii. This per-
turbation, due primarily to the "oblateness" represented by the axially sym-
metric quadrupole (J_2) component in a multipole expansion of gravity (see,
e.g., Danby 1988), is typically 0.1% to 1% the strength of the point-source or
monopole term (Fig. 11). Other gravitational perturbations include: i) solar
gravity, which is weak close to the planet, but dominates oblateness beyond
several tens of planetary radii (exact values depend on the particular planet);
ii) gravity from the other planets which is always small compared to solar grav-
ity; and iii) the attractions of planetary satellites, which are only important
in narrow zones surrounding the satellites and at associated resonant loca-
tions (see the treatments of satellite interactions and of resonances in the next
section). Several non-gravitational forces also perturb particles in planetary
rings. Principal among them are electromagnetic (Lorentz) forces and radia-
tion pressure (Burns et al. 1979). For micron-sized grains, these forces range
from 0.01% to 1% the strength of planetary gravity (Fig. 11). For smaller
submicron-sized grains, however, the strength of these non-gravitational forces

may equal or even exceed that of gravity. The various drag forces - plasma drag, Poynting-Robertson drag, and resonant charge variations - are much weaker ($\sim 10^{-6}$ times gravity), but because they alter orbital energy, often dominate the long term dynamics (see section on timescales).

1. Planetary Gravity. Working in a planet-centered reference frame rotating at the planet's spin rate Ω_p, the gravitational potential Φ outside an arbitrarily shaped body can be shown to satisfy Laplace's equation, $\nabla^2\Phi = 0$ (Danby 1988). Solving Laplace's equation in spherical coordinates yields the standard spherical harmonic expansion of the gravitational potential:

$$\Phi = -\frac{GM_p}{R_p} \sum_{j=0}^{\infty} \left(\frac{R_p}{r}\right)^{j+1} \sum_{k=0}^{j} [C_{j,k}\cos(k\phi_R) + S_{j,k}\sin(k\phi_R)]P_j^k(\cos\theta) \ , \quad (8)$$

where G is the gravitational constant, M_p and R_p are the planetary mass and radius, and r, θ, ϕ_R are the usual spherical coordinates defined in a frame rotating with the planet. The $P_j^k(x)$ are associated Legendre polynomials (Kaula 1966; Schaffer and Burns 1992) and the coefficients $C_{j,k}$ and $S_{j,k}$ are dimensionless quantities whose values are set by the mass distribution within the planet.

The non-axisymmetric terms in a planet's gravitational potential (those with $k \neq 0$) are typically small since the primary result of planetary rotation is an axisymmetric equatorial bulge. Furthermore, away from narrow resonance zones, the non-axisymmetric terms lead to small short-period oscillations that average to zero over several orbital periods. Hence, we can often approximate (8) by

$$\Phi = -\frac{GM_p}{r}\left(1 + \sum_{j=2}^{\infty} J_j \left(\frac{R_p}{r}\right)^j P_j(\cos\theta)\right) \ , \quad\quad\quad (9)$$

where P_j are the Legendre polynomials and only even terms are needed for the fluid giant planets. Choosing the origin of our coordinate system to correspond to the planet's center of mass yields $J_1 = 0$, so there is no gravitational dipole term. For all of the planets except slowly rotating Mercury and Venus, $J_2 \gg J_j$ (with $j > 2$), so in practice we can represent planetary gravitational potentials reasonably accurately by the first two terms (the monopole and quadrupole terms) in Eq. (9). Orbit-averaged equations of motion for the J_2 perturbation are given by Danby (1988) whereas the general problem is discussed more fully by Kozai (1959) and Kaula (1966). The solution to these equations is an ellipse that precesses slowly in space while retaining its size, shape and inclination (see Fig. 12).

2. Radiation Forces. Because photons carry momentum, they impart small forces when they are absorbed, emitted, or scattered by matter. The reaction of a ring particle to these forces causes orbital evolution, but this evolution is usually significant only for small dust particles (tenths to tens of micrometers) which have large surface-area-to-mass ratios. Radiation pressure forces for
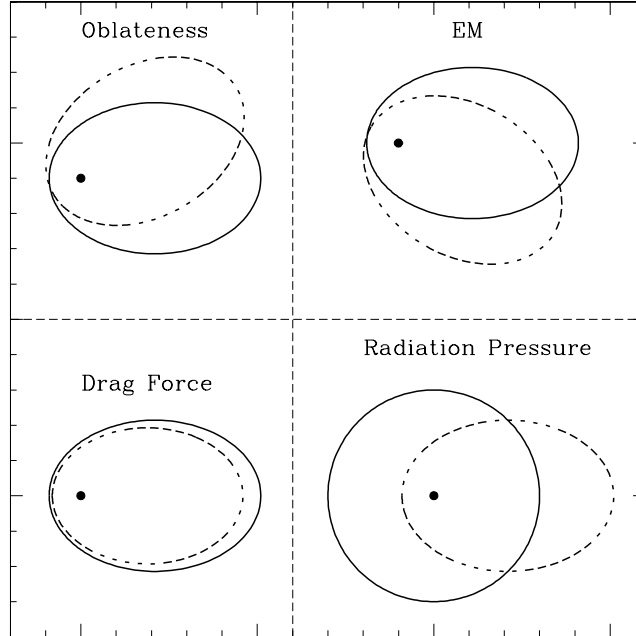
Figure 12. Sketches of orbital evolution under four different secular perturbations: planetary oblateness, electromagnetic force from a dipolar magnetic field, radiation pressure, and drag. In the EM, the drift direction varies within the sign of the particle's charge

spheres of various compositions subject to the solar insolation are given by Burns et al. (1979) and Gustafson (1994), among others.

For a spherical grain, the ratio of the acceleration due to solar radiation pressure vs that due to solar gravity is usually given by

$$\beta = \frac{5.7 \times 10^{-5} \rho s}{Q_{pr}} \ , \tag{10}$$

where Q_{pr} (of order 1) is the radiation pressure coefficient averaged over the solar spectrum, and ρ and s are in cgs units (Burns et al. 1979). Grains of a micron to tenths of microns (where geometric optics fails and Q_{pr} drops) are most affected by solar light. For dust grains orbiting the Sun, the main consequence of radiation pressure is simple to calculate since the force applied to a dust grain is primarily radial and the intensity of radiation emanating from the Sun falls off quadratically with distance, just like solar gravity. Thus the effective gravity felt by an interplanetary dust grain is reduced and these motes take slightly longer to orbit the Sun than they would under gravity alone. For heliocentric particles the only important dynamical outcomes are the arc of a cometary dust tail and the ejection (from the solar system) of small grains, the so-called β- meteoroids, that are released from larger parent bodies near perihelion.

The effects of solar radiation pressure on a dust grain orbiting a planet, however, are much more complex. In the planet's vicinity, a dust grain experiences a solar radiation force that is nearly constant in magnitude, but whose inertial direction varies slowly as the planet orbits the Sun. Since the orbital period of the planet is much longer than that of the ring particle, we usually make the approximation that the solar direction remains constant over one circuit of the ring particle around the planet. Orbit-averaged equations of motion for a circumplanetary particle influenced by radiation pressure were first obtained by Burns et al. (1979) and Chamberlain (1979) by averaging the effects of the perturbing force over one Keplerian orbit. Mignard (1982; Mignard and Henon 1984) later derived equivalent expressions by considering the perturbing potential due to radiation pressure. Hamilton (1993) extended this work to cover the general case of a tilted planet on an eccentric orbit about the Sun, working in equatorial coordinates so that the perturbations due to radiation pressure and planetary oblateness could be combined. Smyth and Marconi (1993), and Ishimoto (1996) give alternate forms of these equations. Solutions to the orbit-averaged equations (Richter and Keller 1995) show that radiation pressure primarily affects an orbit's eccentricity and orientation (see Fig. 12).

When particles pass into the planet's shadow, radiation forces cease. Mignard (1984), however, has demonstrated that the orbital consequences of this periodic interruption are slight.

3. Electromagnetic Forces.   A charged dust grain orbiting through a planetary magnetic field experiences a Lorentz force. Close to the planet, the magnetic field $\mathbf{B}$ rotates at the planet's constant spin rate $\mathbf{\Omega}_p$ and, in a frame rotating at this rate, the Lorentz force is given by:

$$\mathbf{F}_{EM} = \frac{q}{c}(\mathbf{v}_{rel} \times \mathbf{B}) , \tag{11}$$

where q is the charge on the grain, c is the speed of light, and

$$\mathbf{v}_{rel} = \mathbf{v} - (\mathbf{\Omega}_p \times \mathbf{r}) \tag{12}$$

is the velocity relative to the magnetic field, with $\mathbf{v}$ the inertial velocity.

When describing a magnetic field evaluated in a current-free region ($\mathbf{J} \sim \nabla \times \mathbf{B} = 0$), the only remaining constraint that must be satisfied is Maxwell's equation $\nabla \cdot \mathbf{B} = 0$ (Stern 1976). Thus, defining $\mathbf{B} = -\nabla \Phi_{mag}$, $\nabla \times \mathbf{B} = 0$ is automatically satisfied, and we obtain Laplace's equation $\nabla^2 \Phi_{mag} = 0$ with solutions of the same form as (9) above. Hence

$$\Phi_{mag} = R_p \sum_{j=1}^{\infty} \left(\frac{R_p}{r}\right)^{j+1} \sum_{k=0}^{j} [g_{j,k}\cos(k\phi_R) + h_{j,k}\sin(k\phi_R)]P_j^k(\cos\theta) , \quad (13)$$

where the $g_{j,k}$ and $h_{j,k}$ are planetary magnetic field coefficients with units of gauss [Schaffer and Burns (1992) tabulate values for the giant planets and give

additional references; see also Connerney (1993) and Connerney et al. (1996)]. As in the case of planetary gravity, we can capture the dominant secular effects with the lowest order $k = 0$ terms.

We now absorb several of the parameters from Eqs. (11)-(13) into a single dimensionless constant representing the ratio of the Lorentz force to planetary gravity (Schaffer and Burns 1987). We calculate the Lorentz force due to an aligned dipolar magnetic field on a motionless grain in the equatorial plane (i.e., $\mathbf{v} = 0$ and $\theta = 90°$); for this choice the force ratio is independent of the distance from the planet. We define

$$L \equiv \frac{F_{EM}}{F_{GR}} = \frac{qg_{1,0}R_p^3\Omega_p}{cGM_pm_g};$$ (14)

note that the ratio depends both on properties of the grain (the charge-to-mass ratio q/m_g) and properties of the environment (planetary mass, radius, spin rate, and dipole strength).

The Lorentz force can be treated as a perturbation to gravity for grains satisfying $L \ll 1$; thus the particles follow basically Keplerian orbits (with the usual 2:1 epicyclic motions) whose elements gradually evolve. Assuming typical grain potentials of a few volts (see Mendis et al. 1984; Horányi et al. 1992; Horányi 1996), this inequality translates to circumplanetary grains larger than several tenths of a micron in radius. For many applications, including the Jovian ring (Showalter et al. 1987) and the Saturnian E ring (Showalter et al. 1991), dust grains are inferred to be micron-sized and gravitationally dominated; hence their orbital evolution can be handled as a perturbation to a Keplerian orbit. Dust fluences onto the Galileo instrument have been found to exhibit periodicities of 5 hr and 10 hr, demonstrating the important role of Jupiter's magnetic field (rotation period of ∼10 hr; Horányi et al. 1997; Grün et al. 1998).

On the other hand, when $L \gg 1$, these highly charged grains are effectively plasma particles that gyrate about the planet's magnetic field lines (the particles move on 1:1 epicycles; Mendis et al. 1984; Northrop et al. 1989; Horányi 1996); in this case the guiding centers of the paths gradually drift under the perturbing action of gravity.

The precession of orbital pericenter for a charged dust grain on an uninclined orbit in an aligned dipolar magnetic field was first calculated by Horányi and Burns (1991; see Fig. 12). Hamilton (1993) provides orbit-averaged equations for fully three-dimensional orbits in a magnetic field with aligned dipole and quadrupole components.

For values of $|L| \gg 1$ and of the appropriate sign, ejection from the system may occur. Horányi et al. (1993) have suggested that the Jovian dust streams detected in interplanetary space by the Ulysses spacecraft (Grün et al. 1993, 1996a) are composed of particles born deep in the Jovian magnetosphere and flung outwards along the corotation electric field by this process once charges become positive through secondary electron emission. Since all

Table II

Orbital Accelerations and Timescales for 1 Micrometer Dust at 1.8 R_p

	Jupiter	**Saturn**	**Uranus**	**Neptune**
Accelerations (in cm s^{-2})				
Gravity ($\sim r^{-2}$)	800	350	275	350
Oblateness ($\sim r^{-4}$)	5	3	0.5	0.6
Radiation Pressure ($\sim s^{-1}$)	0.1	0.03	0.01	0.003
Electromagnetic ($\sim s^{-2}$)	1	0.05	0.03	0.02
Lifetimes (in years)				
Orbital Evolution				
Poynting-Robertson ($\sim s$)	$\lesssim 10^5$	10^5	$\lesssim 10^6$	10^6
Plasma Drag ($\sim s$)	$[> 10^5]$	$10^{5\pm1}$	$10^{5\pm1}$	$10^{7\pm2}$
Atmospheric Drag ($\sim s$)*	-	-	$10^{2\pm1}$	$10^{5\pm2}$
Resonant Charge Variations	?	?	?	?
Destruction				
Sublimation of pure H_2O ice ($\sim s$)	$10^{3\pm1}$	$10^{5\pm1}$	$\leq \infty$	$\leq \infty$
Sputtering ($\sim s$)	$10^{3\pm1}$	$10^{3\pm1}$	$10^{5\pm2}$	$10^{7\pm2}$
Micrometeoroid Shattering ($\sim s^{-2}$)	$10^{5\pm1}$	$10^{6\pm1}$	$10^{6\pm2}$	$10^{6\pm2}$

* Also depends strongly on r (Herbert et al. 1987)

forces are conservative, the ejection speed (Hamilton and Burns 1993a) can be
readily computed as

$$v_\infty = [2(GM/R)(L - 1/2)]^{1/2} \; ; \tag{15}$$

this yields speeds that range from tens of km/sec to hundreds of km/sec, depending on L's precise value and how deep in the potential well the particles originate.

4. Summary of Forces.   The nature of the various perturbation forces as a function of orbital radius is plotted in Fig. 11. In order to scale this plot to the several ring systems, we have tabulated estimates of the various forces discussed above. Table II gives typical accelerations and their dependence on orbital distance r and particle radius s, as caused by various forces, including the Lorentz force; these apply to 1-micrometer grains placed in the equatorial planes of the giant planets at r=1.8R_p, where R_p is the planet's radius; most entries are from Burns (1991) and Esposito et al. (1991) assuming $Q_{pr} \sim 1$ and $\phi = 1$ V.

Two points must be made. First, accelerations provide at best only a rough idea of the long-term significance of any force since, as described elsewhere in the next section, orbital evolution depends on the phasing of the perturbations (Burns 1976). Second, it is valuable to note how these accelerations vary with

particle size. Any forces, such as drags, that depend on particle cross-sectional area πs^2 have accelerations varying as s^{-1}, whereas electromagnetic accelerations differ as s^{-2} since surface potentials are generally constant for a specific plasma. This of course means that nongravitational accelerations, especially electromagnetic ones, become more important on small grains. It is for this reason that tiny motes, for which electromagnetic forces overwhelm planetary gravity, can be ejected from circumplanetary space if they are charged properly. Horányi et al. (1993) and Hamilton and Burns (1993a) have claimed that this effect can eject dust from the Jupiter system. When grains become very small, the charge-to-mass ratio can be large enough that they no longer follow nearly Keplerian paths but instead can be treated as massive plasma particles that spiral around magnetic field lines (Northrop 1992; Horányi 1996).

5. Drag Forces.   In addition to the perturbation forces described above, relatively weak drag forces also act on dust grains around planets. Although they are usually feeble compared to other perturbations, drags have paramount importance because they, unlike the stronger perturbation forces, can cause secular (monotonic) changes in the orbital energy and angular momentum, and hence in the orbital semimajor axes, eccentricities, and inclinations of dust grains (Burns 1976); in turn, these changes allow grains access to resonant positions (see below) where particles can become trapped and eccentricities/inclinations can be dramatically altered. Over long periods of time, the effects of drag forces are cumulative and noticeable (Fig. 12).

The strongest drag force operating on distant circumplanetary dust is *Poynting-Robertson drag*, which arises from the transfer of momentum from solar radiation to the dust. The effects of Poynting-Robertson drag on dust grains in interplanetary space have been well characterized (Wyatt and Whipple 1950; Burns et al. 1979; Mignard 1984; Gustafson 1994). For circumplanetary particles, however, the effect is more complicated since the primary photon flux does not originate from the body at the orbit's focus. Nevertheless, orbital energy is still dissipated and the semimajor axis of the circumplanetary orbit shrinks with time. Burns et al. (1979) have shown that orbits collapse under Poynting-Robertson drag in approximately the time it takes for a particle (whether in circumplanetary or circumsolar orbit) to absorb the equivalent of its own mass in radiation:

$$T_{PR} \approx 10^3 (a_P/\text{AU})^2 (\rho/\text{g} - \text{cm}^{-3})(s/\text{micrometers}) Q_{\text{pr}}^{-1} \text{yr} , \qquad (16)$$

where a_P is the planet's orbital radius and Q_{pr} is the non-dimensional radiation pressure coefficient (of order 1); this expression is written such that each term in parentheses is non-dimensional. Mignard (1984) has derived expressions for how circumplanetary eccentricities and inclinations evolve due to Poynting-Robertson drag.

Plasma drag and *atmospheric drag* are thought to account for most energy dissipation very close to the giant planets (see two paragraphs below, however); these drags arise due to momentum transfer during the collisions of dust

grains with orbiting charged particles and neutral molecules/atoms, respectively. Both of these forces damp orbital eccentricities and inclinations, causing orbits to eventually adopt the motion of the impacting species, i.e., to move on circular and uninclined paths. Dust orbiting within the synchronous distance moves faster than the plasma, loses energy in collision with the plasma, and spirals in toward the planet. In contrast, dust outside the synchronous distance orbits more slowly than the plasma, and hence gains energy, requiring that it drifts away from the planet. Thorough treatments of plasma drag may be found in Grün et al. (1984) and Mendis et al. (1984); Northrop and Birmingham (1990) improve previous treatments of this problem. The orbital evolution timescale for plasma drag is

$$T_{PD} \approx \frac{2s\rho\zeta}{3\rho_p v} \ , \tag{17}$$

where ρ_p is the mass density of the thermal plasma, v is the grain's speed relative to the plasma; the constant ζ is about 1 for effectively uncharged grains but is much lower, 10^{-2}, once the flow is subsonic and Coulomb attraction must be included.

Broadfoot et al. (1986) have noticed that atmospheric drag, caused by an extended planetary exosphere, will lead to rapid orbital evolution for dust at the inner edge of the Uranian ring system. We express the timescale for loss by atmospheric drag as

$$T_{atm} \approx \frac{\rho s v_{orb}}{\rho_{atm} v^2} \ , \tag{18}$$

where ρ_{atm} is the atmosphere's mass density, v_{orb} is the particle's orbital speed and v is its speed relative to the atmosphere.

Atmospheric drag is concentrated near the planet where it may be most influential in causing dust orbits to collapse. Because of the surprisingly high exospheric temperatures in the outer atmospheres of most giant planets (Broadfoot et al. 1986), atmospheric gases extend to significant altitudes, implying that gas drag may be relevant for the inner parts of many ring systems. Broadfoot et al. (1986) and Herbert et al. (1987) assert that the Uranian exosphere sweeps the inner Uranian ring region clear of material in quite short times. Even with such a rapid exospheric drag, Uranian dust can be replaced by sufficiently active collisions (Colwell and Esposito 1990a).

Even though atmospheric drag and plasma drag have been suspected to determine evolution timescales for circumplanetary dust, neither is well-characterized because the mass densities of the impacting species are basically not known in the region of interest. This has become particularly clear following Galileo's observations of Jupiter's gossamer ring components (Ockert-Bell et al. 1999; Burns et al. 1999; see discussion below) which lie across a region where the orbital evolution due to plasma drag is outward whereas Poynting-Robertson drag leads to orbital collapse. The images strongly suggest that the rings are composed of inward-evolving ejecta from the satellites Amalthea and Thebe;

hence P-R drag must dominate. Yet, earlier calculations (Burns et al. 1984; see Table II) estimate that plasma drag should be orders of magnitude more effective. The implication is that the putative values for plasma density must be wrong by orders of magnitude, which is not implausible in this poorly studied region. This is but one case in which circumplanetary dust may provide a visible probe of magnetospheric conditions; expelled dust from the jovian system also highlights those magnetospheric conditions (Horányi et al. 1993).

Just as collisions with circumplanetary material might account for momentum transfer to circumplanetary grains, the interaction of orbiting material with *mass from outside* the system may also lead to orbital collapse since it brings mass, but no net angular momentum to the grains. This mass drag has been estimated most recently by Stevenson et al. (1986; cf. Cuzzi and Estrada 1998) and is insignificant for our purposes.

Drag resulting from *resonant charge variations* (Burns and Schaffer 1989; Northrop et al. 1989), a process even less quantifiable as to its efficacy than the drags described above, arises because the charge imposed on a grain lags the local equilibrium grain potential, meaning that work can be done on the orbit. Paths evolve toward or away from synchronous orbit at rates that can be rapid. This process is implicit in the remarkably rapid evolution of Jovian ring material identified by Horányi and Cravens (1996). This same energy-transfer is responsible for the magnetospheric capture of interplanetary particles, turning hyperbolic orbits into elliptical ones (Horányi 1994; Colwell et al. 1998).

Timescales for the processes described above are contained in Table II. The plasma drag timescale, listed as $2\times10^{2\pm1}$ yrs by Burns et al. (1984) using a nominal plasma density, has been raised substantially to agree with the absence of features in Jupiter's gossamer ring (Burns et al. 1999; see below). The sublimation timescale is very short ($< 10^4$ yrs) for "dirty" and absorbing water-ice particles at Saturn but much longer for pure ice and refractory materials ($10^3 - 10^5$ yrs) (J. Colwell, personal communication, 1999). Refractory material, more likely relevant to circumplanetary dust, evaporates very slowly.

C. Size Distributions

Populations of natural objects differ in their numbers as a function of radius, depending upon their properties, modes of origin and evolution. Terrestrial rocks, asteroids and interplanetary meteoroids, as well as impact craters, are represented usually by exponential power laws. The exponents will vary, according to whether these laws are written in mass or radius, and whether they are expressed differentially or cumulatively (Fujiwara et al. 1989 gives the algebraic relations between the exponents for these various expressions.). In particular, catastrophic fragmentations have a differential power-law index of -3.5 for the radius (see Eq. (3); Dohnanyi 1972; cf. Durda and Dermott 1997).

Laboratory experiments indicate that the exponent deviates somewhat depending on the conditions of fragmentation; with extensive grinding, small sizes become more common and the slope steepens (Hartmann 1969). However, due to practical constraints, experiments are usually conducted at speeds and with

sizes that differ vastly from those appropriate to many space collisions; thus somewhat-speculative scalings are used to extrapolate results (Fujiwara et al. 1989; Housen and Holsapple 1990). In other natural systems, nucleation or condensation products are often generated near a single size.

Size distributions for circumplanetary dust are generally inferred by trying to match, for assumed optical properties and functional dependences (e.g. power laws in s), ring brightnesses obtained at a discrete number of phase angles; they are thus non-unique. Because the circumplanetary particles that are discussed in this chapter are usually widely separated, these rings are intrinsically very faint. They become most visible when the signal is primarily diffracted light (for example Jupiter's ring is about ten to twenty times brighter in forward-scattered light than back-scattered). Most images of circumplanetary dust were taken when the spacecraft was in the planet's shadow with phase angles of $170-179°$. The particle sizes that most effectively diffract visible light into such angles are microns. Thus most faint rings seem to be composed primarily of micron-sized grains (Burns et al. 1984). Size distributions can also be estimated by interpreting the data from dust detectors (Grün et al. 1992c) and from plasma measurements (Meyer-Vernet et al. 1996, 1998; Oberc 1994).

As listed in the penultimate column of Table I, particles in the various ethereal rings seem to exhibit great variety in their size distributions – some apparently collisionally derived, others monodisperse and yet others with steep power-laws. The typical view is that dust particles are derived from larger bodies by collisional fragmentation, and particles are eventually lost from the system at the small end. Electrostatic bursting has also been suggested to shatter particles and smooth off asperities (Mendis et al. 1984; Burns et al. 1980). Models for the evolution of the size distribution do not include aggregation because collisions occur at high speeds. Observed size distributions are not those that particles are born with whenever the lifetime of particles differs with particle size; for example, if small particles are rapidly eliminated, the observed size distribution will be flatter than that introduced (the power-law index is lowered, Burns et al. 1984). And, as described in the earlier sections on orbital evolution and grain destruction, lifetimes of circumplanetary grains do change with particle sizes; not surprisingly, smaller grains survive less time in the system.

Few attempts have been made to explain the observed size distributions. The Jovian main ring and Saturn's D ring, with exponents somewhat shallower than the expected fragmentation result of -3.5 may be collisional debris that has evolved; the shallow slope of Jupiter's size distribution, -2.5 (+/-0.5), may indicate orbital evolution that is faster in inverse proportion to particle radius (Burns et al. 1984). The steep values for Saturn's F ring (Showalter et al. 1992) and perhaps its G ring (Showalter and Cuzzi 1993, cf. Throop and Esposito 1998) are not understood. The monodisperse sizes of Saturn's spokes (Doyle and Grün 1990) and its E ring (Showalter et al. 1991) speak to unique origins. Goertz et al. (1983), Mendis et al. (1984), Grün et al. (1984) and Tagger et al. (1991) argue that spokes form when sub-micron grains are

ejected by electrostatic forces from larger grains. Hamilton and Burns (1994) aver that Saturn's E ring grains are naturally selected as those having sizes that allow a resonance condition to be satisfied (Horányi et al. 1992; see next section); others believe that this condition incriminates vapor condensation near Enceladus. The most thorough treatments of the evolution of the size distribution of dusty rings have been carried out numerically at the University of Colorado, where the dust is viewed as the end product of collisional processes in ring-moon systems. Colwell and Esposito (1990a,b) have combined calculations of dust supply with Markov chain models for dust transport between the Uranian/Neptunian rings and their moons to generate radial profiles of dust optical depth (see concluding section). The most recent applications of these simulations are contained in review chapters about the Uranian (Esposito et al. 1991) and Neptunian (Porco et al. 1995) rings. These find that the extant systems can be matched fairly well with reasonable parameter choices.

D. Destruction and Generation of Grains

Circumplanetary grains are swept out of systems by the orbital evolution described above (see Table II), and simultaneously are destroyed by the fierce environments in which most reside. Depending on their composition, some particles may sublimate away but, more likely, they will vanish because of the mass flux striking them, either being shattered apart in hypervelocity collisions with bombarding interplanetary micrometeoroids (Cuzzi and Estrada 1998) or sputtered away by the impinging magnetospheric flux, many of the same particles that account for the electric charges that the grains acquire (Johnson 1990; Johnson et al. 1993; Jurac et al. 1995). We will learn below that lifetimes of extant grains are remarkably short, albeit not very well constrained. In turn, since faint rings are visible about all the giant planets, grains must also be born so that the ethereal rings are continually resupplied: the play remains the same even as its characters change. Most authors consider that tiny grains are born in collisions, the same violent events as those that ultimately account for their demise. Fine debris may be sloughed off moonlets (Cuzzi and Burns 1988; Colwell and Esposito 1990a,b; Esposito et al. 1991) following mutual collisions. Gentle versions of these same occurrences may temporarily remove grains from independent orbit.

Sputtering by energetic ions and electrons is surprisingly capable of destroying ring particles because the ejection process is efficient, and because large fluxes of energetic particles populate planetary magnetospheres. This process has substantial variations and uncertainties, owing to our incomplete knowledge of the impinging particle fluxes and to large differences in the sputtering yield depending upon target properties and impacting particle energy (Johnson 1990; Jurac et al. 1998). The sputtering lifetime T_s of a grain can be estimated by simply dividing its mass M by the mass loss rate $(\dot{M})$: thus

$$T_s \sim \frac{M}{\dot{M}} \sim \frac{Ns}{\left(\sum_i F_i \zeta_i\right)} \; , \tag{19}$$

where N is the number density of molecules in the grain and a sum is taken over all ions present of the product F_i (flux of the ith ion) times ζ_i (the sputtering yield per impact of the ith ion). Obviously these sputtering lifetimes depend on knowing yields accurately from laboratory experiments (Johnson 1990), where it may be difficult to duplicate conditions in space, and on having comprehensive information available as to the bombarding magnetospheric fluxes. The latter are generally based on very limited measurements (often merely a single spacecraft passage at best). Nevertheless the lifetimes, given in Table II and likely to be accurate to perhaps no more than an order of magnitude or so, are meaningful insofar as they are very brief on cosmic timescales. Also the fluences of damaging ions may depend sharply on location, so that lifetimes may vary substantially across a broad ring, especially if the ring absorbs the magnetospheric particles.

Collisions with micrometeoroids (Cuzzi and Estrada 1998) destroy circumplanetary dust effectively because interplanetary material acquires very high speeds as it is gravitationally accelerated towards the giant planets. If there is a lower cut-off in the sizes of dust grains that can penetrate a magnetosphere (see Colwell and Horányi 1996), then catastrophic fragmentation, in which a grain is shattered by a single impact, dominates over progressive erosion (see Burns et al. 1980). This implies that *number* fluxes (and not *mass* fluxes) of projectiles govern grain lifetimes and, depending on the size of the lower cut-off, that small particles might survive longer than large ones. Typical estimates (see Burns et al. 1984) are collisional lifetimes of $T_c \approx 10^5(1 \quad \mu m/s)^2$ yrs around all the giant planets. The identification of some interstellar projectiles within the impinging flux (Grün et al. 1993; Baguhl et al. 1994) will not alter this timescale much.

Other processes have been invoked to generate some ring material. At one time volcanic dust from Io was considered a viable source for the jovian ring; even today it is a primary contender to produce the dust that forms the Jovian dust streams (Horányi et al. 1993; Grün et al. 1996a; Graps et al. 2000) and some other material that inhabits the Galilean satellite region (Grün et al. 1997, 1998a; Krüger et al. 1999). A small fraction of interplanetary and interstellar dust may be captured by the giant planets, and could account for the few retrograde particles discovered by Galileo (Colwell et al. 1998). Minute grains of a narrow size distribution, such as those in Saturn's E ring, could have been launched by volcanoes or geysers. Particles may even condense directly from the local gas (Johnson et al. 1989).

Small ring-moons are almost always intimately intermingled with ethereal rings (see Fig. 1). In particular, all the faint rings that are clumpy or time-variable suffer significant satellite perturbations. This association is evident in most of the ring systems: Saturn's Pan (Showalter 1991) was discovered within the Encke gap where an incomplete arc of filamentary material is located; Cordelia abuts Uranus' dust-laden λ ring; Galatea, which was found skimming along the inner edge of Neptune's Adams ring and may be kinematically connected to its arcs (Porco et al. 1995), resides in an unnamed

dusty (perhaps discontinuous) ringlet (Ferrari and Brahic 1994); the activity in the F ring's environs as seen during Saturn's 1995-96 ring-plane crossings (Nicholson et al. 1996) may be related to perturbations by the shepherd satellites; other clumping is due to systematic tags by the satellites (Showalter and Burns 1982; Kolvoord et al. 1990) and micrometeoroid impacts (Showalter 1998); and Jupiter's gossamer rings are clearly derived from its heavily bombarded satellites Amalthea and Thebe (Ockert-Bell et al. 1999, Burns et al. 1999).

Even though not directly visible, parent bodies – from which the rings are derived – are assumed to be present in most faint rings. Modelers have inferred their presence from the short lives of individual dusty ring particles; more direct evidence is contained in the back-scattering opacity of rings and in the ability of diaphanous rings to absorb energetic charged particles (Van Allen 1982, 1983). In particular, Showalter et al. (1987) argue, from the Jovian ring's phase function, that the parent bodies have an opacity like that of the visible ring; a preliminary comparison (Burns et al. 1999) of back-scattered Keck images (de Pater et al. 1999) with forward-scattered Galileo images (Ockert-Bell et al. 1999) also finds that the Jovian ring contains "large" bodies, in agreement with charged particle absorptions measured in this neighborhood by Pioneer 11 (Fillius et al. 1975) and the Galileo entry probe (Fischer et al. 1996). The presence of parent bodies has been inferred for Saturn's G ring (Van Allen 1983, 1987). Saturn's F ring must contain some large objects to have affected the Voyager radio signal (Tyler et al. 1983b). Pioneer 11 absorptions in the neighborhood of Saturn's F ring have been interpreted to be localized "microsignatures", caused by clouds of ejecta from mutual collisions of parent bodies (Cuzzi and Burns 1988).

The destruction section above mentions that most circumplanetary dust is probably *generated through meteoroid impacts* with visible or unseen parent bodies. This process has been observed by the Galileo dust detectors as the spacecraft flew past various Galilean satellites (Krüger et al. 1999b), and was inferred from brightness bursts measured in Saturn's F ring (Showalter 1998). The current ring mass in small grains, M_{ring}, will be produced by a meteoroid mass flux density Φ in a time T_Φ according to

$$M_{ring} = Y\Phi A_p T_\Phi f \; , \qquad (20)$$

where Y is the yield (i.e., the mass excavated/impacting mass) from a typical hypervelocity impact, A_p is the cross-sectional area of the parent bodies, and f is the mass fraction of ejecta that are micron-sized. This assumes that all ejecta escape from the parent bodies. In the case of impact ejecta leaving the larger of the ring-moons, this may not be a good assumption because typical launch speeds from hypervelocity events are comparable to the escape speeds from these bodies (cf. Fig. 17 of Burns et al. 1984; Table 1 in Burns et al. 1999). Then the nature of the surface (which determines the launch characteristics) becomes important as does the size, shape and orbital location of the ring moon (which affect the escape speed from various locales of the moons).

Source satellites of a specific size produce the most impact ejecta (Burns et al. 1984, 1999): satellites need to be as big as possible up until they become so large that they are able to retain ejecta. The latter size for an isolated satellite is that at which the moon's escape speed matches the slowest speed at which ejecta leave a hypervelocity impact site. For a soft regolith, this corresponds to an object about 5-10 km in radius, i.e., the size of the smallest of the known ring-moons (e.g., Adrastea). Furthermore escape from the ring-moon closest to the planet is generally favored because, due to tides and non-spherical shapes, escape over much of its surface requires no impulse whatsoever (Burns et al. 1999); loss of all surface debris will inevitably lead to a "hard" regolith.

E. Interactions with Nearby Satellites

As the jovian gossamer ring's connection to its nearby moons demonstrates, the erosion of satellites through impacts with interplanetary projectiles may be the principal supplier of ring material. In this section we discuss additional effects of satellites on rings. Once released, the dust that comprises the ethereal rings continues to interact significantly with the largest of the parent bodies: through long-range gravity, ring-particle orbits are perturbed and these tugs will shift individual orbits but can also shepherd rings in ensemble. Grains whose orbits cross the satellites will eventually collide with these targets: some grains may be absorbed, but the most energetic impacts will generate new ring debris.

What are the initial paths of ejecta launched from ring-moons? The gross nature of these orbits depends solely upon the velocities of the sources and the relative velocities at which the ejecta leave the sources.

When considering the speed distribution of the ejecta, and averaging over it, typical departure speeds from small, isolated spherical objects turn out to be comparable to the classical escape speed, which as a rough rule of thumb is that the escape speed (in m s^{-1}) is roughly equal to the object's radius in kilometers. Once shape and tidal effects are included, escape generally only becomes easier. Thus most escaping debris from a typical ring moon, even when the causative impact took place at many tens of km s^{-1}, happens at $10 - 10^2$ m s^{-1}. Since orbital speeds are many tens of km s^{-1}, after departing the satellite, typical orbits of ejecta have very small eccentricities and inclinations, $\sim v_{esc}/na$. That is to say, the ejecta will form a narrow tube about the source satellite. This tube will precess and smear out under the action of oblateness as discussed below.

The departure trajectories along which ejecta leave moons in the Roche zone (Fig. 1) are quite convoluted by tidal forces, the influence of aspherical moons and non-inertial effects. Burns et al. (1980; their Fig. 4) show a jovian example, while the complex interplay of a stream of particles shearing past a moon embedded in the Saturn's F ring is animated by Weidenschilling et al. (1984; their flip-chart figures running between pp. 379-413).

Since the dust grain originated at the satellite (of radius R_{moon}), its orbit (ignoring perturbations) will forevermore cross the moon's (taken to be

a low-eccentricity orbit at radial distance a_{moon}). Using a particle-in-a-box formalism, the e-folding collisional timescale is

$$T_{col} \sim \pi \left((sin \ i_{dust})^2 + (sin \ i_{moon})^2 \right)^{\frac{1}{2}} \left(\frac{a_{moon}}{R_{moon}} \right)^2 \left(\frac{U_r}{U} \right) T_{orb} \ ,$$

where $T_{orb} = 2\pi a_{dust}/v_{dust}$ is the dust grain's orbital period with a_{dust} its semimajor axis and v_{dust} its orbital speed; U is the relative velocity between the moon and the dust grain; U_r is its radial component; and the orbital inclinations of the dust and ring-moon are measured relative to the planet's equatorial plane (Soter 1971; Hamilton and Burns 1994). The ratio U_r/U is nearly independent of e_{dust} and, to within $< 20\%$, equals one.

Grain-moon collisions occur on a very rapid timescale, typically a few years to a decade for impacts into ring-moons by zero-inclination particles. Once inclinations make the problem three-dimensional, the collisional lifetimes of grains become much longer; e.g., in the Jovian case, grains crossing the orbits of large Thebe and Amalthea (whose inclinations are $1.09°$ and $0.37°$, respectively) will strike the satellites in $\sim 10^2$ to 10^3 yrs; collisions with the much smaller ring-moons happen in $\sim 10^5$ yrs. A totally different and more sophisticated approach (Canup and Esposito 1995) to recollision finds similar times.

The relative speed between a particle traveling on a low-inclination, arbitrarily sized eccentric orbit and a moon moving along a circular, nearly equatorial path is about

$$v_{col} \sim ev_{moon} \ ,$$

a result accurate to about 10% for particle orbits of all sizes and shapes, as long as the collision does not occur near an orbital turning point (Hamilton and Burns 1994). Since orbital speeds are several tens of km/sec, impact speeds for orbits with $e > 0.01$ generally vastly exceed the escape speed of the ring-moon or parent body, and thus impact trajectories are little modified by the "massive" target.

Impacts become hypervelocity (exceed the speed of sound) once orbital eccentricities reach modest values. Yields, $Y \sim 5v^2$ with v in km s^{-1} (Grün et al. 1984), achieve values $\gg 1$ (i.e., impacts generate much more ejecta than the impactor's mass) at speeds above a km s^{-1}. With such values, systems may be self-sustaining.

The few collisions that occur at gentle speeds do not necessarily lead to absorption since these systems usually lie within or near the Roche zone (Fig. 1). Re-accretion is quite complicated and depends on the surface properties, spin rate, orbital location and morphology of the target, and on the relative masses of the target/projectile (Weidenschilling et al. 1984; Colwell and Esposito 1992).

Even if grains do not collide directly with the source moons, those that pass nearby will be scattered during their close flybys. Of course, these gravity-assists occur on shorter timescales than direct collisions but are less potent too.

As a rough rule of thumb, maximal scatterings are like the local v_{esc}, or at most tens of m s^{-1}. Thus the eccentricities and inclinations of ring particles should random-walk with typical stepsizes like v_{esc}/v_{orb}, and so produce hardly any long-range effects, although they do mean that ring-moons scatter particles to a few times their own size. This should lead to diffuse ring edges (see Burns and Gladman 1998).

The accelerations due to ring-moons drop off like d^{-2} and so are relevant only within a narrow region surrounding the moon (Goldreich and Tremaine 1982). However, as the next section mentions, even small forces, if they resonate with a ring particle's preferred motions, can have important consequences.

As described above, ejecta from continual collisions with a moon will form a debris tube surrounding the orbital path of the source moon. Because of the planet's oblateness and electromagnetic effects, orbital planes precess swiftly (a few months to a few years; see Fig. 12), whereas inclinations are preserved. Thus, after differential precession, grains launched in a single event soon lie on a hoop of height $2a[sin\, i + (v_{esc}/v_{orb})]$ and width $2a[e + (v_{esc}/v_{orb})]$. This hoop will be brighter along its top and bottom edges, as well as the inner and outer radial boundaries, because the individual particles making up the distribution undergo epicyclic motions, spending more time in these regions. Burns et al. (1999) argue that this process accounts for the form of the Jovian gossamer ring (Fig. 3).

The global dynamics of tenuous rings have been investigated by Lissauer and Espresate (1998) who show that low-opacity rings can be shepherded much like their denser compatriots as long as constituents can be properly mixed before their next encounter with the satellite. For this reason, when the Jovian ring moons were located precisely at the ring edge, questions were raised whether these objects were sources or shepherds of ring material (Showalter et al. 1987; Showalter 1989). In the Jovian case, because of the close similarity of the gossamer ring thickness with the elevations of the satellites off the equatorial plane, Burns et al. (1999) are confident that the ring is derived from the moons, and, by Occam's Razor, they argue that the main ring is similarly born from Adrastea, the tiniest of the known Jovian inner satellites.

IV. CELESTIAL MECHANICS AND ORBITAL EVOLUTION

A. Introduction

Recall our working definition of a ring as an ensemble of individual particles orbiting a planet. Ring particles are created, their orbits evolve, and they are destroyed, often on very short timescales. To understand the structure and dynamics of a ring as a whole, it is necessary to first appreciate the orbital evolution of the individual ring particles. We then build detailed models from realistic ensembles of individual orbits. The quality of a ring model is judged by two criteria: i) how well the model's predictions match actual observations and ii) how plausible the model's physical assumptions are.

In this section, we focus on faint dusty rings for which the methods of single-particle dynamics may be applied. First we introduce a simple way to describe an orbit.

If a ring particle orbits a spherical planet (point-mass gravity), it follows a bound Keplerian ellipse around the central planet (Danby 1988). Knowledge of the six quantities that specify a ring particle's position and velocity in space at a given time is sufficient to determine uniquely its Keplerian path. In other words, there exists a one-to-one correspondence between phase space (x, y, z, $\dot{x}$, $\dot{y}$, and $\dot{z}$, where the dot signifies differentiation with respect to time) and *orbital elements* (geometric quantities that specify the size, shape, and orientation of - as well as the particle's position along - an elliptic orbit). Many choices of orbital elements are possible; the ones that we use here are a, e, i, Ω, ω, and ν. The semimajor axis a is one-half the largest dimension of an orbit, the eccentricity e characterizes the orbit's ellipticity, the inclination i indicates the tilt of the orbit relative to the equatorial plane, the longitude of the ascending node Ω describes the orientation of the orbital plane, the argument of pericenter ω determines the angular position of the ellipse's shortest radius within the orbital plane, and the true anomaly ν identifies where the ring particle is located along its elliptic path. The particle's mean motion, or average angular speed,

$$n = \left(\frac{GM_p}{a^3} \right)^{1/2} \tag{21}$$

and its orbital period, $\tau_{Kep} = 2\pi/n$, are determined solely by the planetary mass M_p, the orbital size a, and the gravitational constant G. Further description of the orbital elements is given in basic celestial mechanics texts (e.g., Burns 1976; Danby 1988) and by Hamilton (1993, his Fig. 1).

The use of orbital elements offers several advantage over working with co-ordinates. For an unperturbed elliptical orbit, all coordinates and velocities are functions of time $[x(t)$, $y(t)$, $z(t)$, $\dot{x}(t)$, $\dot{y}(t)$, and $\dot{z}(t)]$, while for orbital elements all of the time dependence is contained in $\nu(t)$. The other elements a, e, i, Ω, and ω are simple constants which determine the invariant size, shape, and three-dimensional orientation of the elliptical orbit in space. Thus a description of an orbit in terms of the orbital elements allows one to visualize how the orbit actually appears much better than does a description in terms of time-dependent coordinates.

Given the physical properties of a dust grain (its size, shape, charge, and light-scattering properties), the details of the various forces that act upon it, and its initial conditions, we can use Newton's second law, $\mathbf{F} = m\mathbf{a}$, to track the particle's position at all times. The resulting second-order differential equation cannot usually be solved analytically, and is often difficult to solve numerically because of the large differences in the strengths of the strongest and weakest forces.

For large ensembles of ring particles, however, we are generally not interested in the details of how a single ring particle's position and velocity change,

but only in the general character of its orbit. Accordingly, we can, in many
cases, make use of an orbit-averaging procedure which utilizes the geometrical
orbital elements. Orbit-averaging is a perturbation technique that requires that
the planet's gravity be the dominant force acting on the particle. There are
three advantages to this approach: i) orbital elements give a geometric picture
of how a ring particle's orbit evolves; ii) the orbit-averaged equations of motion
are 500–1 000 times faster to integrate than the original equations (Hamilton
1993); and iii) in many cases, approximate analytic solutions to interesting
problems can be found.

Before discussing orbit-averaged equations of motion, we first detour to
describe resonances, which dominate the dynamics in certain ring regions.

B. Resonances

Dusty rings at Jupiter, Saturn, and Uranus cover broad radial swaths that
often include one or more major resonances, those narrow regions of circum-
planetary space where the frequencies of perturbations are commensurate with
orbital frequencies (see Murray and Dermott 1999). In these locales, orbit-
averaging, which is described below as a generally effective method for treating
small perturbations, misses virtually all of the dynamics. Because of the rel-
ative scarcity of resonances, it is tempting to dismiss them as unimportant
in determining the structure of planetary rings - this however is an erroneous
conclusion! Moreover, drag forces, which secularly alter orbital semimajor axes
(Table III), are effective at transporting material from non-resonant zones into
resonant locations.

Adjacent to resonant locations, small periodic perturbations can produce
large effects by adding together in phase. Typically, one or more slowly-varying
"resonant arguments" – in addition to the secular perturbations discussed above
– can have important dynamical consequences. The most well-studied resonant
perturbations in celestial mechanics arise from the gravitational perturbations
between two orbiting bodies (see, e.g., Murray and Dermott 1999).

Resonances, however, need not be gravitational; they arise any time a
periodic perturbation force drives an orbit at one of its natural frequencies.
The periodically varying electromagnetic force on an orbiting dust grain is one
such example (Burns et al. 1985); resonances with electromagnetic forces have
been dubbed *Lorentz resonances* and for micron-sized dust in the jovian ring
these resonances are far stronger than their gravitational cousins. Resonant
charge variations (Burns and Schaffer 1989; Northrop et al. 1989) and shadow
passage (Horányi and Burns 1991) also cause resonant perturbations.

Hamilton (1994) showed that the same mathematical formalism governs all
types of resonances – gravitational and non-gravitational – and used this fact to
derive resonant strengths for the most important electromagnetic resonances.
In this section, we show how a generic resonance affects the orbital properties
of a dust grain.

An orbiting dust grain is near a resonance when $d\Psi/dt \approx 0$ with the general

resonant argument given by

$$\Psi = A\phi + B\phi' + C\varpi + D\Omega \ . \tag{22}$$

Here ϕ is the mean longitude of the particle, ϖ and Ω are the particle's longitudes of pericenter and the ascending node, respectively, ϕ' is the mean longitude of the perturber, and A, B, C, D are integer constants. This resonant argument applies equally well to many different types of resonances including those due to the gravitational perturbations from a satellite on a circular orbit as well as those due to electromagnetic perturbations. Valid resonances must satisfy the relation $A+B+C+D = 0$, because the choice of direction for the zero point of longitude (from which all longitudes are measured) is arbitrary (Hamilton 1994). The strongest resonances are typically the first-order resonances, whether in inclination $(C = 0, D = \pm1)$ or eccentricity $(C = \pm1, D = 0)$. These resonances occur at places given roughly by:

$$\frac{n}{n'} = \frac{A}{A \pm 1} \ , \tag{23}$$

where the mean motion n is expressed by Eq.(21) above and n' is the frequency of the perturbation, be it from another satellite or a rotating planet's gravity and magnetic fields. The locations of first-order Lorentz resonances in the Jovian ring system are displayed in Fig. 13. We focus here on the 2:3 inclination resonance that Burns et al. (1985) believe causes the transition between Jupiter's main ring and its vertically extended interior halo. The appropriate resonant argument is

$$\Psi_{2:3} = 2\phi - 3\phi' + \Omega \ . \tag{24}$$

The orbital elements most strongly affected by an inclination resonance are a, i, and Ω. Hamilton (1994) derives the following expressions for the effects of the resonance:

$$\frac{da}{dt} = 2nai\beta \cos \Psi_{2:3} + \dot{a}_{drag} \tag{25a}$$

$$\frac{di}{dt} = -\frac{n\beta}{2} \cos \Psi_{2:3} \tag{25b}$$

$$\frac{d\Omega}{dt} = \frac{n\beta}{2i} \sin \Psi_{2:3} \ . \tag{25c}$$

Here t is time and β, the resonance strength, is nearly constant across the width of the resonance.

We include the drag term in the first of the above equations because i) orbital evolution due to drag brings dust grains to resonant locations, and ii) the drag term primarily affects the semimajor axis (Table III) which is important in determining the outcome of a resonant interaction. Drag effects on the inclination and other orbital elements are less important and usually lead only to periodic wiggles; these are ignored here for simplicity.

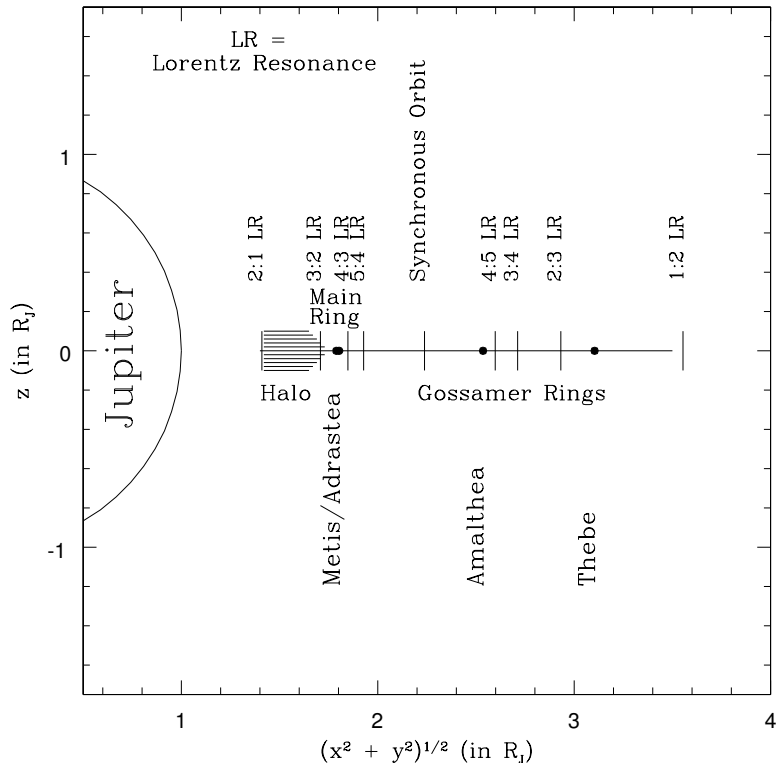## Rings, Moons, and Lorentz Resonances

Figure 13. Location of the Lorentz resonances in the Jovian system. For evolutions
that are slow enough, resonant trapping will occur when grains move toward syn-
chronous orbit; resonant jumps in eccentricity and inclination are expected when
particles leave the vicinity of synchronous orbit.

Depending on the sign of the drag term, either of two outcomes can occur
at a resonance: resonant trapping or a resonant jump. In the first case, if
evolution due to the drag is slow enough, then the two terms in the da/dt
equation can balance and the evolution of the semimajor axis due to the drag
term can be halted; this is *resonant trapping*, which occurs only when the
evolution is toward the synchronous location (Fig. 13). In this case, we can
take $da/dt = 0$ in Eq. (25 a), solve for $\cos\Psi_{2:3}$, and eliminate this variable
from Eq. (25 b). After integration (assuming an initially uninclined orbit) we
have:

$$i = \sqrt{\frac{\dot{a}_{drag}t}{2a}} \ . \tag{26}$$

The evolution of the semimajor axis is arrested by the resonance, but the in-
clination grows as the square root of time to compensate (Fig. 14). This is
a general feature of resonant trapping and follows from the constancy of the
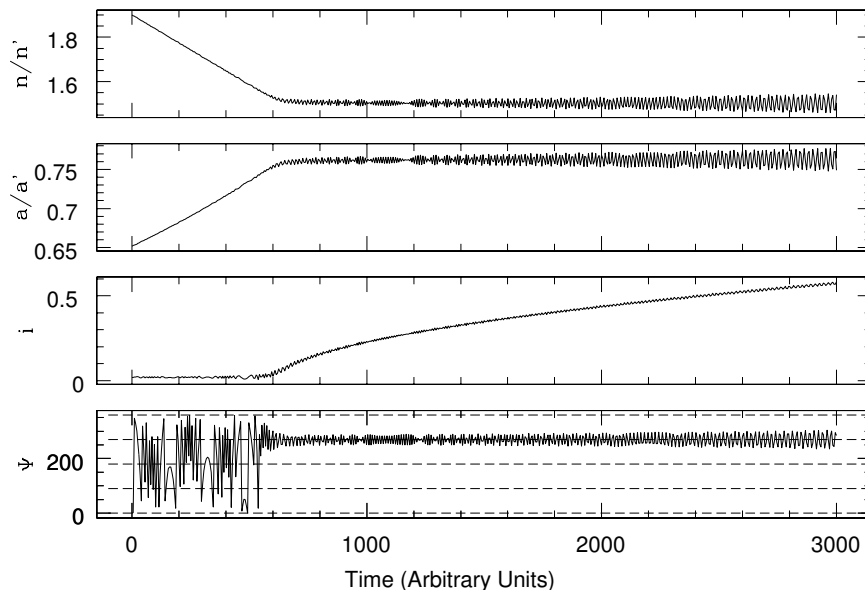
Figure 14. The trapping of a hypothetical ring particle that drifts outward through the 3:2 vertical Lorentz resonance; the orbit becomes trapped when the ratio between the particle's mean motion n and the planet's spin rate n' is $3/2$. During trapping, the evolution of a halts, while the inclination i grows at a rate that is independent of the resonant strength. Until the capture takes place, the resonant argument Ψ takes on all values, but once trapping occurs, it oscillates around $270°$. Compare to Fig. 15.

Jacobi integral (Hamilton 1994). Note that the resonant strength does not enter into Eq. (26).

Resonant jumps occur when the evolution is away from the synchronous location (Fig. 15). Small resonant jumps also occur anytime the resonant strength is slight compared to the drag term, because then the resonant term in Eq.(25 a) cannot balance the drag term for any value of $\Psi_{2:3}$. These particles do not become trapped into resonance, but rather are "kicked" across the resonance. Both the semimajor axis and inclination experience jumps, whose overall amplitudes are determined by the resonance strength (Fig. 15). The relative jumps in a and i, however, are related by the Jacobi constant.

Both types of behavior are expected to be important in the jovian ring (Fig. 2). Drag evolution in the ring is dominated by the Poynting-Robertson effect (Burns et al. 1999) which acts inward toward the planet. Inside synchronous orbit, this moves dust away from synchronous orbit and, accordingly, resonant jumps are to be expected. The vertically extended jovian halo appears downstream from the 2:3 Lorentz resonance (Fig. 15), and it disappears (perhaps widened to the point of invisibility) near the 1:2 Lorentz resonance (Fig. 2; Schaffer and Burns 1992; Hamilton 1994; cf. Horányi and Cravens 1996).See also Fig. 20 later.
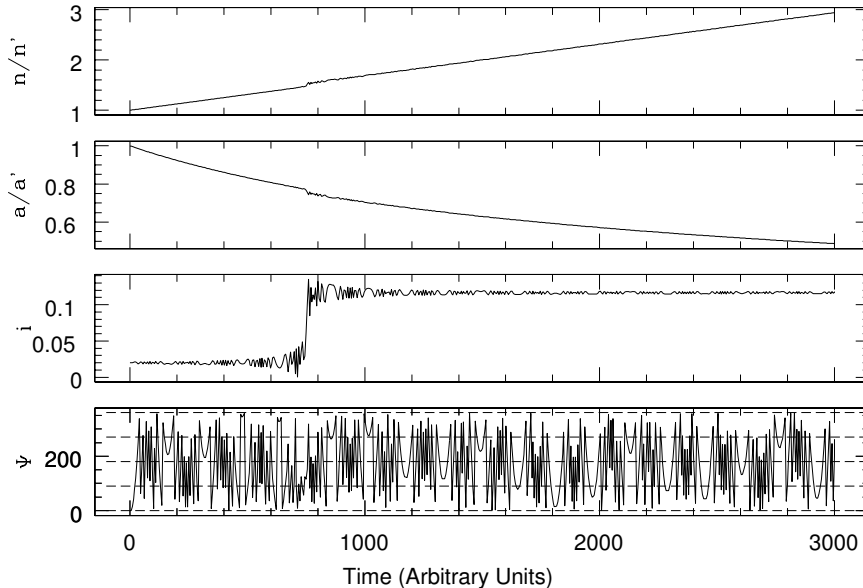
Figure 15. The history of a particle that evolves through the same 3:2 resonance as shown above, but now in the inward direction expected for jovian ring particles. When the ratio n/n' reaches $3/2$, the orbital elements a and i experience sharp kicks. The size of the kick depends on the strength of the Lorentz resonance which, in turn, depends on particle size. Compare to Fig. 14.

Beyond synchronous orbit, in the faint gossamer rings, orbital evolution is primarily toward synchronous orbit, so resonant trapping is expected for particles smaller than about 2-5 microns. Larger grains, for which electromagnetic forces are weak, will pass through the resonances relatively unscathed. This is probably what is happening in the gossamer rings where Galileo seems to have observed the large particles that evolve inward but not the small particles that are spread into a diffuse background halo by resonant trapping. In numerical simulations of the evolution of charged dust through this region (Burns et al. 1999), grains smaller than tens of micrometers become trapped.

C. Orbit-Averaged Equations of Motion

We now consider how an orbit, described in terms of its orbital elements (see above), changes when non-resonant perturbation forces act. If these perturbation forces are small compared to the planet's point-source gravity the first five orbital elements will change but only slowly. All will vary on characteristic timescales τ_{pert} which are long compared to the unperturbed Kepler period ($\tau_{pert} \gg \tau_{Kep}$). Thus we can separate timescales: over short times ($t \sim \tau_{Kep}$) a ring particle follows a nearly Keplerian path, the properties of which slowly vary over the longer timescale ($t \sim \tau_{pert}$).

The perturbations that act on circumplanetary dust grains larger than about a micron in size are much weaker than the gravity of the central planet;

thus, as just discussed, over short intervals the actual orbit does not differ greatly from a Keplerian ellipse. We can take advantage of this fact by averaging the perturbations to an orbit over one Kepler period, making the explicit assumption that the particle follows an *unperturbed* Kepler ellipse during this time. This technique, which is accurate to first order in the small parameters that determine the perturbations, is called orbit-averaging. Orbit-averaged equations of motion tell us how the orbital elements change in time over intervals much longer that the orbital period.

1. Coupled Equations of Motion In circumplanetary environments, the various perturbation forces (Sec. III) operate simultaneously. In this section we present a coupled set of orbit-averaged equations that describe the orbital evolution of a dust grain under the simultaneous influences of planetary oblateness, radiation pressure, the electromagnetic force, and an unspecified drag force. In order to simplify the equations, we assume that the orbital inclination i and the planetary obliquity γ are both less than about 30°. Ring inclinations all satisfy the first assumption, and only Uranus and Pluto do not satisfy the second. In addition, since rings are composed of a great ensemble of particles, we are usually only interested in the gross character of how these orbits change with time, not in the details of where the particles are along their paths. Accordingly, we consider changes to a, e, i, Ω and ω but not those of the sixth orbital element ν. We work in a non-rotating equatorial coordinate system and, after lengthy orbit-averaging calculations (see Hamilton 1993), we find:

$$\left\langle \frac{da}{dt} \right\rangle_{Total} = 0 + \dot{a}_{drag} \ , \tag{27}$$

$$\left\langle \frac{de}{dt} \right\rangle_{Total} = \alpha(1 - e^2)^{1/2} \sin\phi_\odot + \dot{e}_{drag} \ , \tag{28}$$

$$\left\langle \frac{di}{dt} \right\rangle_{Total} = Z \cos\omega \ , \tag{29}$$

$$\left\langle \frac{d\Omega}{dt} \right\rangle_{Total} = Z \frac{\sin\omega}{\sin i} + \dot{\Omega}_{xy} \ , \tag{30}$$

and

$$\left\langle \frac{d\omega}{dt} \right\rangle_{Total} = -Z \frac{\sin\omega}{\sin i} + \frac{\alpha(1 - e^2)^{1/2}\cos\phi_\odot}{e} + \dot{\omega}_{xy} \ , \tag{31}$$

where perturbations due to drag forces have been left unspecified. Here α is a frequency that parameterizes the strength of radiation pressure; the dimensionless ratio of solar radiation pressure to planetary gravity is $2\alpha/(3n)$ (Hamilton 1993) with the mean motion n given by Eq. (21). For problems in which radiation pressure is important, it is useful to define the solar angle:

$$\phi_\odot = \Omega + \omega - n_\odot t - \delta, \tag{32}$$

Table III

Dynamical Outcomes from Orbital Perturbations[1] in Planetary Rings

Orbital Perturbation Force	Semimajor Axis	Eccentricity and Inclination	Node and Pericenter
Planetary Oblateness	No	No	MD[2]:Strong
Solar Gravity	No	Weak	MD:Weak
Lorentz Force away from Resonance	No	Weak	MD:Strong
Lorentz Force at Resonance	Weak	Strong	Strong
Radiation Pressure w/o shadowing	No	Strong	Strong
Radiation Pressure w/ shadowing	Weak	Strong	Strong
All Drags (Plasma, Poynting-Robertson, Neutral)	MD:Weak	MD:Weak	MD:Weak

[1] Assumes micrometer-sized grain with -5V potential [2] MD = monodirectional. This enhances the effect over time.

where $n_\odot$ is the planet's mean motion, t is time, and δ is a constant (Hamilton 1993). For orbits with $i \lesssim 30°$, $\phi_\odot$ is roughly the angle between orbital pericenter and the Sun as seen from the planet. The frequencies $\dot{\Omega}_{xy}$ and $\dot{\omega}_{xy}$ are the rates at which the node and pericenter change due to oblateness and the assumed dipolar magnetic field. They are given by

$$\dot{\Omega}_{xy} = -\frac{3nJ_2R_p^2}{2a^2(1-e^2)^2} + \frac{nL}{(1-e^2)^{3/2}}\left(1 - e^2 - \frac{n}{\Omega_p}\right) \tag{33}$$

and

$$\dot{\omega}_{xy} = \frac{3nJ_2R_p^2}{a^2(1-e^2)^2} - \frac{nL}{(1-e^2)^{3/2}}\left(1 - e^2 - \frac{3n}{\Omega_p}\right). \tag{34}$$

with L from Eq. (14). Combining Eqs.(30–34) yields the rate at which the solar angle $\phi_\odot$ changes:

$$\left\langle\frac{d\phi_\odot}{dt}\right\rangle_{Total} = \frac{\alpha(1-e^2)^{1/2}\cos\phi_\odot}{e} + \frac{3nJ_2R_p^2}{2a^2(1-e^2)^2}$$

$$+\frac{2nL}{(1-e^2)^{3/2}}\left(\frac{n}{\Omega_p}\right) - n_\odot. \tag{35}$$

Finally, Z is a frequency determined by the sum of the vertical components of radiation pressure (first term in the expression below) plus the electromagnetic force (second term):

$$Z = \frac{\alpha e[\sin\gamma\sin(n_\odot t + \delta) + \sin i\sin(\Omega - n_\odot t - \delta)]}{(1-e^2)^{1/2}} +$$

$$\frac{3nLe}{2(1-e^2)^{5/2}}\left(\frac{g_{2,0}}{g_{1,0}}\right)\left(\frac{R_p}{a}\right)\left(\frac{n}{\Omega_p}\right), \tag{36}$$

where $g_{1,0}$ and $g_{2,0}$ are the aligned dipolar and quadrupolar components of the planetary magnetic field.

Despite the simplifying assumptions made at the beginning of this section, the above set of equations is imposing. Most of the complexity, however, is contained in the frequencies $\dot{\Omega}_{xy}$, $\dot{\omega}_{xy}$, and Z. The contributions of the oblateness force, radiation pressure, and the electromagnetic force can be readily identified by the terms containing J_2, α, and L, respectively. For problems in which one of these forces is known to be unimportant, the appropriate terms can be simply set to zero.

With the approximations $i \lesssim 30°$ and $\gamma \lesssim 30°$, the changes in the orbital elements that determine azimuthal structure $(e, \phi_\odot)$ are independent of those that determine vertical structure (i, Ω). We will invoke this property to make simple analytic approximations in the next section. First, however, we combine the results of our orbit-averaged derivations with typical strengths of the perturbation forces to determine how strongly the various forces influence each of the orbital elements. The results are summarized in Table III. If the perturbation force does not affect a given orbital element, we put a "No" in the appropriate bin of Table III; otherwise we classify the effect as "Weak", or "Strong".

In addition, we note when a force causes an orbital element to increase or decrease secularly instead of simply oscillating by putting "MD" for monodirectional in the appropriate column. So, for example, in the orbit-averaged approximation, the oblateness force does not affect the semimajor axis (Eq. (27)), the eccentricity (Eq. (28)), or the inclination (Eq. (29)), but causes monodirectional changes in Ω (Eq. (33)) and ω (Eq. (34)). Under the influence of planetary oblateness, the longitude of pericenter $\Omega + \omega$ precesses (increases with time) as long as $i < 63°$ (Fig. 12). Monodirectional changes in the orbital elements are important because even small variations will build up to have noticeable effects over time. The consequences of periodic perturbations, by contrast, tend to average out in time. Thus not only are the strongest perturbations to each orbital element important, but the strongest *monodirectional* perturbations are often relevant too.

Most entries in Table III are taken from the orbit-averaged rates in the perturbation equations (27)–(31) above. The effects of planetary oblateness, radiation pressure (without shadowing by the planet), and the two drag forces are inferred directly from these equations (the effects of drag on the orbital node and pericenter are neglected in Eqs. (30)–(31) since other forces produce much stronger monodirectional outcomes). The fully three-dimensional, orbit-averaged equations for the Lorentz force away from resonance predict small oscillations in eccentricity and inclination that we neglected in the low-inclination approximation made above. Perturbations from solar gravity can

also be orbit-averaged (Hamilton and Krivov 1996, 1997), but because the resulting expressions are long, we did not reproduce them here. Nevertheless, we show in Table III that the primary result of solar gravity on ring particles is to cause a slow orbital precession. We also include some effects that cannot be orbit-averaged: shadowing by the planet for radiation pressure (Mignard 1984) and Lorentz resonances (Hamilton 1994). The main consequence of shadowing is to produce small periodic changes in the semimajor axis (Horányi and Burns 1991), while Lorentz resonances strongly alter eccentricities, inclinations, and semimajor axes (see earlier discussion and Figs. 14 and 15).

2. Visualizing Orbital Evolution   The time histories of the orbital elements come from integrating Eqs. (27)–(36) numerically. In this section, we describe how plots of these time histories can be employed to visualize orbital evolution. We use dust around Mars as our example. The small satellites of Mars, Phobos and Deimos, are continually bombarded by interplanetary grains. Most micron-sized ejecta from these microcollisions is expelled from the satellites and goes into circumplanetary orbit around Mars, forming a very faint—and as yet undetected—ring system (Soter 1971; Horányi et al. 1990, 1991; Ip and Banaszkiewicz 1990; Juhász et al. 1993; Juhász and Horányi 1995; Hamilton 1996; Krivov and Hamilton 1997). Although Martian rings are currently theoretical constructs, the predicted evolution of dust from Deimos provides a simple example of circumplanetary dust dynamics. The strongest two perturbation forces affecting Deimos dust are Mars' oblateness and solar radiation pressure. Mars' magnetic field is weak enough that electromagnetic effects may be safely ignored and drag forces, primarily Poynting-Robertson drag, are too weak to cause significant consequences over timescales of a few tens or hundreds of years.

Figure 16, obtained by numerical integration of Eqs. (27)–(36), shows the evolution of a 20 μm particle launched from Deimos. When we integrate $\mathbf{F} = m\mathbf{a}$ in coordinates, and translate into orbital elements, we obtain a nearly identical orbit, thereby validating the averaging approximation; for a detailed comparison of these two approaches, see Hamilton (1993). The orbital semimajor axis, a, remains constant in agreement with Eq. (27) and Table III. The orbital eccentricity oscillates sinusoidally with a period near Mars' orbital period of 1.88 years, while the solar angle $\phi_\odot$ regresses nearly linearly from roughly $90°$ to $-90°$ over one eccentricity oscillation. Since the perturbation forces are small, the orbit can be well approximated by a Keplerian ellipse at each instant in time. At any moment we can visualize the full orbit of Fig. 16 by using the instantaneous values of the slowly-varying orbital elements. We notice that the points in Fig. 16 where the solar angle is zero are also the positions where the eccentricity is maximum. Since a is constant, these are also the locations where the orbital pericenters and apocenters of the instantaneous Kepler orbit are at their closest and furthest distances from Mars, respectively.
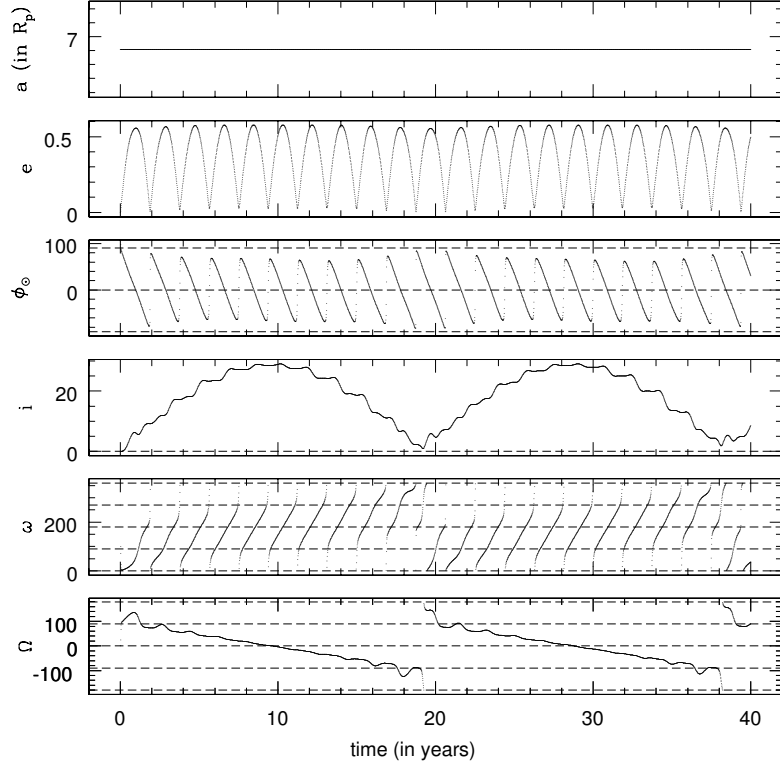
Figure 16. The evolution of the orbital elements of a 20μm particle launched from Mars' moon Deimos onto an initially circular, uninclined orbit about Mars ($J_2 = 0.001960$). The active perturbation forces are planetary oblateness and solar radiation pressure. For this initial condition, we have $\alpha = 1.078$ rad/yr, $L = 0$, and $\gamma = 25.2°$. For $e = 0$, we calculate $\dot{\varpi}_T = -3.228$ rad/yr, $\dot{\omega}_{xy} = -2\dot{\Omega}_{xy} = 0.2239$ rad/yr, and $\dot{\Omega}_T = 0.2921$ rad/yr.

Now, for low inclinations, the solar angle, $\phi_\odot$, is nearly the angle between the Sun and pericenter as seen from Mars. So the closest material to Mars should be found in the solar direction while the most distant material should be located in the anti-solar direction. To check this assertion, we transform the orbit elements of Fig. 16 into cartesian coordinates and project them into the rotating xy plane; the results are shown in Fig. 17. The points form an annular region which is offset in the antisolar direction from Mars, and the closest and furthest material from Mars is found in the expected directions.

We can also use the orbital elements to help picture the vertical structure of the Deimos ring. The inclination in Fig. 16 varies roughly sinusoidally over a 20-year period, and the longitude of the ascending node Ω regresses linearly from $90°$ to $-90°$ over one inclination oscillation. The maximum inclination out of
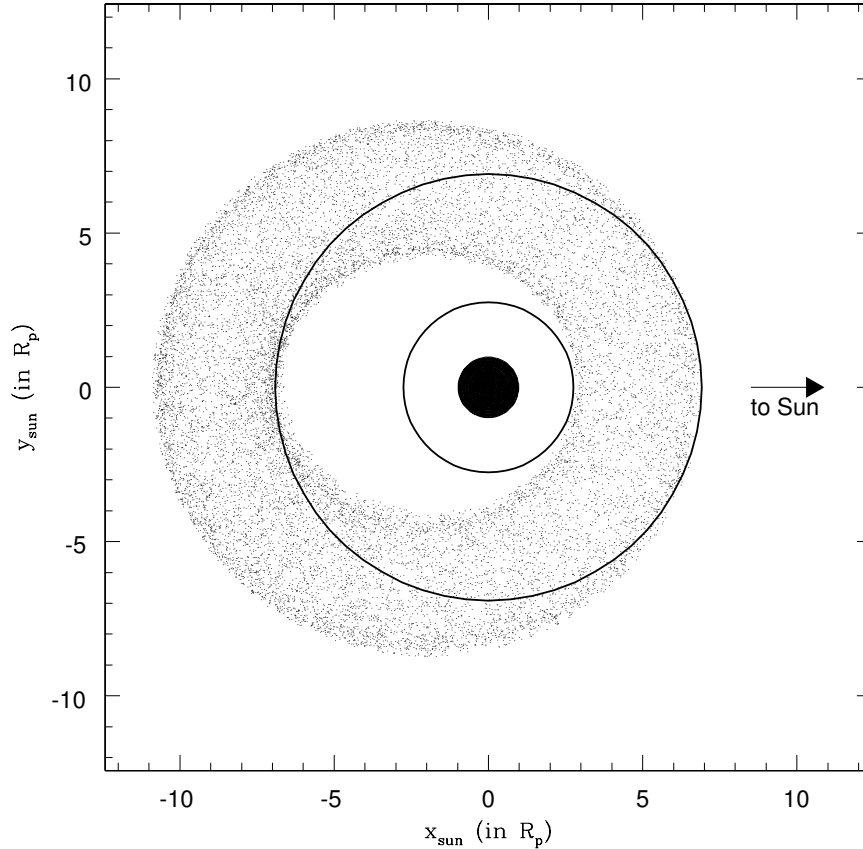
Figure 17. The positions of a particle whose orbital history is shown in Fig. 16
projected onto rotating xy coordinates. Mars (solid circle), the orbit of Phobos
(inner ring), and the orbit of Deimos (outer ring) are shown for comparison. Note
that the distribution of the dust grains forms an annular region that is offset in the
antisolar direction.

Mars' equatorial plane occurs when $\Omega = 0$ (this is the ascending node of ecliptic
plane on the equatorial plane). If we view the dust distribution from along the
line where $\Omega = 0$, to the right we should find material most elevated out of the
equatorial plane (since these dust grains have just passed the ascending node).
Similarly, to the left, ring material should be depressed (since the dust grains
are just approaching the ascending node). More generally, the distribution of
dust should be tilted so that most material to the right is elevated while that
to the left is depressed. Figures 17 and 18 show the results of transforming and
projecting the data in Fig. 16; the resulting distribution of dust is significantly
tilted as expected. The perturbations of planetary oblateness and radiation
pressure cause Deimos' dusty ring to be offset away from the Sun and tilted
out of the equatorial plane. This example shows how the time histories of the
orbital elements can be used to visualize the actual orbit.

D. Approximate Analytic Solutions

One of the major advantages of the orbit-averaged equations discussed in section IV.C is that, in many situations, approximate analytic solutions can be found. For example, the nearly sinusoidal oscillations of e and i, and the almost linear behavior of $\phi_\odot$ and Ω in Fig. 16 hint at underlying analytic solutions. In this section, we discuss several simple analytic solutions to approximations of the full equations of motion, Eqs. (27–36).

1. Azimuthal Structure; Forced Eccentricity   We begin the search for analytic solutions by taking advantage of the fact that Eqs. (28) and (35) decouple from the other equations for small inclinations. In addition, we make the further approximation that e remains small. Following Hamilton (1996; see Horányi and Burns 1991) we find that, with the initial condition $e = 0$ at $t = 0$, Eqs. (28) and (35) have the solution:

$$e = \frac{2\alpha}{\dot\varpi_T} \sin \frac{\dot\varpi_T t'}{2} \tag{37}$$

and

$$\phi_\odot = \frac{\dot\varpi_T t'}{2} + \frac{\pi}{2} \tag{38}$$

with

$$\dot\varpi_T = \dot\Omega_{xy} + \dot\omega_{xy} - n_\odot. \tag{39}$$

Here $\dot\varpi_T t' = (\dot\varpi_T\, t\ \text{modulo}\ 2\pi)$ and t is time. The solution states that during one sinusoidal oscillation of e, $\phi_\odot$ will change linearly from $-90°$ to $90°$ crossing through either $\phi_\odot = 0°$ or $\phi_\odot = 180°$ when $e = e_{max}$, depending on the sign of $\dot\varpi_T$. As the eccentricity returns to zero, the solar angle "jumps" back to $90°$ to restart the cycle. The jump in $\phi_\odot$ is physical (since $e \sim 0$) and arises from radiation pressure (the first term on the right-hand side of Eq. (35) which rapidly drives $\phi_\odot$ to $90°$. Figure 16 provides a stringent test of our analytic solution, since the values of e and i are not always low as we assumed (in Fig. 16, $i_{max} \sim 30°$ and $e_{max} \sim 0.56$). Qualitatively, the approximate analytic solution agrees reasonably well with the behaviors of the eccentricity and solar angle in Fig. 16, although some deviations can be seen. For instance, the angle $\phi_\odot$ and, to a lesser extent, e are modulated at the 20-year oscillation period of the orbital inclination. These effects arise because we neglected the inclination dependence of $\phi_\odot$ in our solution; the fact that the deviations are greatest at points in Fig. 16 where the inclination is largest supports this claim.

We measure $e_{max} = 0.56$ off Fig. 16. Using the numerical values given in Fig. 16's caption, Eqns. (37) and (38) predict an oscillation period $2\pi/|\dot\varpi_T|$ of 1.95 years and $e_{max} = 2\alpha/\dot\varpi_T = 0.6$. Our simple theory does well at predicting the period, but overestimates e_{max} by $\sim 15\%$ larger than this value; this discrepancy arises from the fact that e is not always small in Fig. 16, as was assumed in the derivation of the equations.
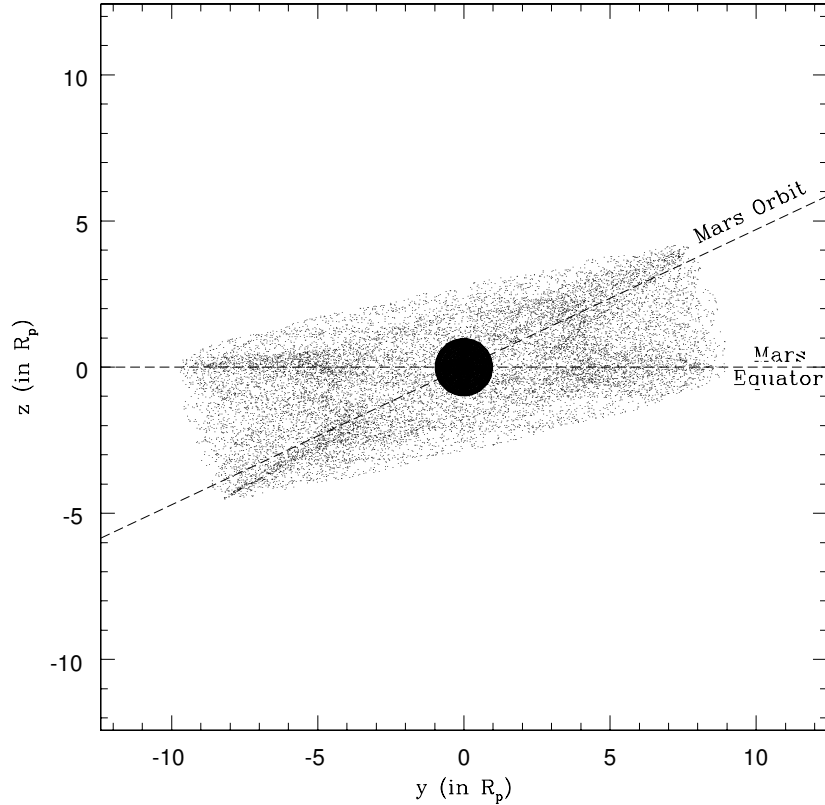
Figure 18. The positions of a particle whose orbital history is shown in Fig. 16 projected onto non-rotating yz coordinates viewed from along the positive x axis (the intersection of Mars' equatorial and orbital planes). Mars is shown to scale as a solid circle. Note that the distribution of dust grains in this projection is rectangularly shaped and tilted out of Mars' equatorial plane. The amount of tilt depends on the particle size; larger particles form a narrower distribution which is tilted less steeply from Mars' equation.

The analytic solution given by Eqs. (37)–(38) can be understood geometrically in terms of free and forced eccentricities (see Horányi and Burns 1991, Fig. 2). The forced eccentricity is simply the eccentricity at the stationary point of Eqs. (28) and (35) which depends solely on the strengths of the perturbation forces. It can be found numerically for arbitrary eccentricity and reduces to

$$e_{forced} = \frac{\alpha}{|\dot{\varpi}_T|} \qquad (40)$$

for $e \ll 1$. The free eccentricity is the amplitude of the oscillation about this value and is determined by starting conditions. With our choice of initial condition ($e = 0$ at $t = 0$), $e_{free} = e_{forced} = e_{max}/2$. The forced eccentricity causes the ring of dust in Fig. 17 to be centered about a point located a distance ae_{forced} away from Mars in the antisolar direction (Hamilton 1996).
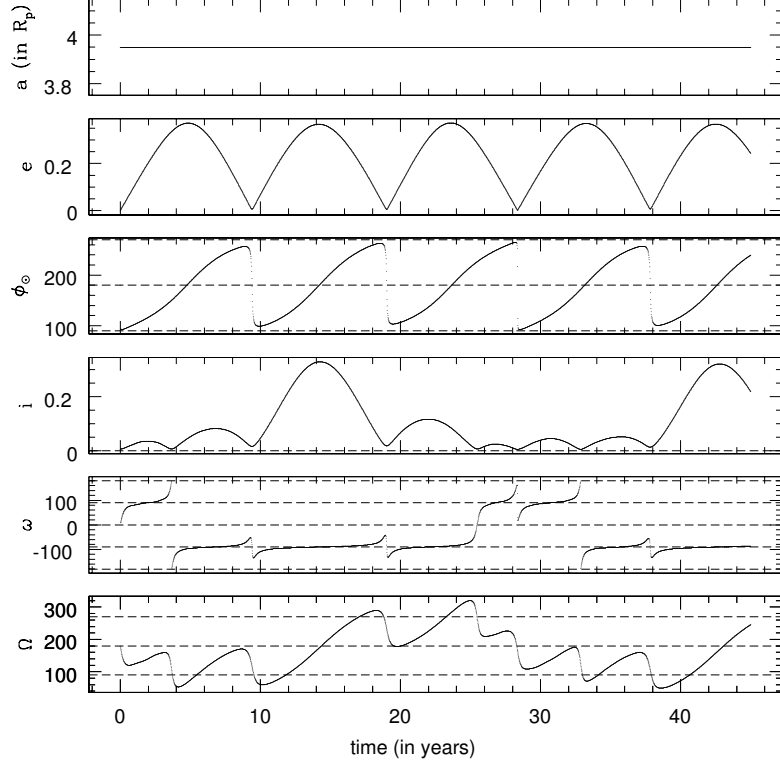
Figure 19. The orbital evolution of a $1.2\mu m$ particle launched from Saturn's moon Enceladus onto an initially circular uninclined orbit. The perturbation forces are solar radiation pressure, planetary oblateness, and electromagnetism. For this initial condition, we have: $J_2 = 0.01630$, $\alpha = 0.1169$ rad/yr, $L = -0.001875$, and $\gamma = 26.7°$. For a characteristic $e = 0.3$, we calculate $\dot{\varpi}_T = 0.6093$ rad/yr and $\dot{\omega}_{xy} = 5.329$ rad/yr.

2. Vertical Structure; Forced Inclination The inclination and node time histories of Fig. 16 appear to be longer-period and noisier versions of the eccentricity and solar angle traces. Accordingly, we look for a solution like Eqs. (37)–(38) and ignore the short-period jitter. Mathematically, we use the solution for e and $\phi_\odot$, and average Eqs. (29)–(30) over the eccentricity-oscillation period. Following Hamilton (1993), we find:

$$i_{long} = -\frac{\alpha^2 \sin\gamma}{\dot{\Omega}_T \dot{\varpi}_T} \sin\frac{\dot{\Omega}_T t'}{2} \qquad (41)$$

and

$$\Omega_{long} = \frac{\dot{\Omega}_T t'}{2} + \frac{\pi}{2} \qquad (42)$$

with

$$\dot{\Omega}_T = \frac{\alpha^2}{2\dot{\varpi}_T} + \dot{\Omega}_{xy}. \qquad (43)$$

As expected, the solution is of the same form as that for the azimuthal structure with i taking the role of e, and Ω acting like $\phi_\odot$. Quantitatively, Eqs. (41)–(43) predict a maximum inclination of 30° and an oscillation period of 21.5 years, values in reasonable agreement with Fig. 16.

By analogy to the forced eccentricity, we define a forced inclination:

$$i_{forced} = \frac{\alpha^2 \sin\gamma}{2|\dot{\Omega}_T \dot{\varpi}_T|}. \tag{44}$$

This has a direct interpretation in terms of the Laplace plane (see Hamilton 1996). For orbits that begin with $i = 0$, we have $i_{free} = i_{forced} = i_{max}/2$.

3. Vertical Structure; Locked Pericenter Figure 19 shows the evolution of a 1.2-μm E ring particle originally started on a circular orbit at Enceladus' distance (Fig. 7). Over the fifty years displayed in the plot, the dominant perturbations are Saturn's oblateness, solar radiation pressure, and the electromagnetic force (Fig. 11). The eccentricity and solar-angle time-histories are similar to those of Fig. 16 for Deimos dust, but here the solar angle precesses rather than regresses which follows from the fact that $\dot{\varpi}_T$ is positive in (43). In addition, the $n_\odot$ term doesn't dominate Eq. (39) here as it did for Deimos; instead the other two terms are large and nearly equal in magnitude. This causes $\dot{\varpi}_T$ to be very sensitive to e. Using $e \sim 0.3$ as a representative value to calculate $\dot{\varpi}_T$, we predict the amplitude and period of the eccentricity oscillation for Fig. 19: $e_{max} \sim 0.38$ and $\tau \sim 10.3$ years, respectively.

The out-of-plane history of this E ring grain is quite different than that of the Deimos grain (Fig. 16). The most striking feature is that the argument of pericenter appears to try to lock to $\pm 90°$ at all times when $e \neq 0$ and $i \neq 0$. Although the inclination remains small ($i \lesssim 0.4°$), this behavior predicts a distinctive vertical structure for the ring. For most of the time, the argument of pericenter is locked to $-90°$, which means that the location of pericenter is as far below Saturn's equatorial plane as possible. So at times when $\omega = -90°$, the inner parts of the ring are depressed below the equatorial plane while the outer parts of the ring are elevated above the plane. At instants when $\omega = 90°$ the opposite occurs, although since the inclination is very small at those times, the effect is less pronounced.

The forced inclination solution discussed above does not apply to the dust grain of Fig. 19 because here we are interested in explaining changes that occur on timescales comparable to the eccentricity-oscillation period. Accordingly, we cannot average over one eccentricity-oscillation as we did in the previous section. Instead, we find an approximate analytic solution for pericenter-locking by assuming $\omega = \pm 90°$, solving for the other orbital elements, and showing that the solution is stable against small perturbations. Following Hamilton (1993), we find

$$\sin i_{eq} = \left| \frac{Z}{\dot{\omega}_{xy}} \right|, \tag{45}$$

$$\frac{d\Omega}{dt}\bigg|_{eq} = \dot{\Omega}_{xy} + \dot{\omega}_{xy}, \tag{46}$$

and

$$\omega_{eq} = \frac{\pi}{2}\left(\text{sign}\left(\frac{\dot{\omega}_{xy}}{Z}\right)\right). \tag{47}$$

Not surprisingly, the vertical structure of the E ring is governed by the term Z, which contains the effects of the vertical forces in this problem. Since $\dot{\omega}_{xy}$ is positive for the parameters of Fig. 19, Eq. (47) implies that the sign of ω_{eq} follows that of Z. The term Z is dominated by the negative contribution from the aligned magnetic quadrupole. As the Sun moves above and below the ring plane, its contribution to Z changes sign (Eq. (36)), and occasionally dominates the electromagnetic contribution. The inclination is not free; Eq. (45) shows that it is linearly proportional to e for small e, a feature that can be clearly seen in Fig. 19.

V. PUTTING IT TOGETHER

This chapter began by recalling the techniques used to observe planetary rings and then summarized our knowledge about the dust that circles the giant planets. These sections were followed by a review of the physical and dynamical processes that act on isolated circumplanetary grains, and a survey of some relevant celestial mechanics. Now we connect all of these topics by explaining briefly how the physics that we've discussed might lead to the observed character of three dust-rich systems: the Jovian rings, Saturn's E ring and the dust bands of Uranus and Neptune. As we will see, these three systems exemplify three different modes of origin: Jupiter's rings are likely to be debris from impacts into the moons by interplanetary meteoroids, while the E ring may be self-sustained as high-speed impacts of ring dust generates new material, and the dust in the Uranian/Neptunian rings may be merely the small-size tail of a continually evolving mix of satellites and ring material.

A. Jovian Rings

The several distinctive structures that are visible in Jupiter's ring system provide strong circumstantial clues as to how this system works. In particular, observations by the Galileo spacecraft show that Jupiter's thickened gossamer bands are precisely circumscribed by the orbits of the ring-moons Amalthea and Thebe (Fig. 3; Ockert-Bell et al. 1999; de Pater et al. 1999; Burns et al. 1999). Voyager images had earlier hinted that very tiny and equatorial Adrastea skims the flattened main ring's periphery and that the Jovian ring's halo arises at the 3:2 Lorentz resonance (Figs. 2, 13 and 15); higher-quality Galileo frames have now confirmed and refined these findings. The gossamer rings' unique morphology—especially the rectangular end profiles
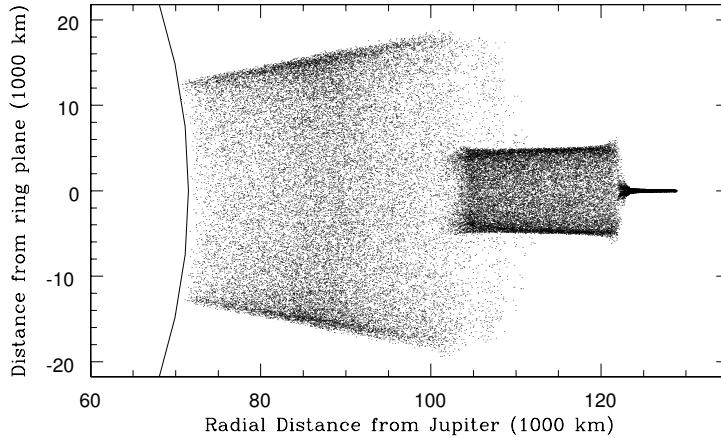
Figure 20. Orbital evolution of a 2 micron dust grain released from the small jo-
vian satellite Metis (a=128 000 km) on an initially circular uninclined orbit. The
grain evolves under the combined forces of gravity, radiation pressure, the Lorentz
force (ϕ=+5V, L=0.002735), and an artificially enhanced drag force. Using an
enhanced drag force speeds up the numerical integrations without introducing spu-
rious effects; a plot made with much slower Poynting-Robertson drag would look
much the same as this one. The drag force pulls the dust grain in toward Jupiter
across the strong 2:3 and 1:2 Lorentz resonances, where the inclination and eccen-
tricities of the dust grain receive strong kicks (see Fig. 15). The thin main ring
(between 123,000km and 129,000km) and the diffuse halo (between 100,000km and
123,000km) are clearly visible in spacecraft images (Fig. 2). The extremely diffuse
"second halo" interior to the first has not yet been observed; it is a prediction of
this model.

at the satellites' orbits with half-thicknesses that match the satellites' excur-
sions above/below the planet's equator and the enhanced brightnesses along the
top/bottom ring edges (see Fig. 3)—can be understood if all gossamer ring par-
ticles are ejecta lost from the satellites when high-speed meteoroids strike them
(see section on Generation of Grains; Eq. (20)) and this debris then evolves
inward toward Jupiter (Burns et al. 1999). Apparently this orbital drift is
due to Poynting-Robertson drag (Eq. (16), rather than caused by plasma drag
(Eq. (17)) and/or resonant charge variations, because the rings appear uniform
across synchronous orbit, where these latter drags would change sign (see Ta-
ble II). Following impacts into tiny satellites within the Roche limit, all impact
ejecta will escape. Hence, despite equatorial Adrastea being a much smaller
target than Thebe and Amalthea, which lie beyond the Roche limit and whose
gravities are strong enough to retain substantial amounts of ejecta, the inner
moonlet might be a more prolific supplier of collisional debris than the others.
This suggests that the thin main ring is composed primarily of Adrastea's de-
tritus (Burns et al. 1999). Once again, as a result of Poynting-Robertson drag,

the orbits of this material decay inward, across the main ring where some of it will be absorbed by Metis (see the section on interactions with satellites); the remainder will eventually reach the 3:2 Lorentz resonance (Eq. (23); Schaffer and Burns 1992; Hamilton 1993; cf. Horányi and Cravens 1996; see Fig. 2) where its inclination will be raised substantially (see Fig. 15), thereby accounting for the ring's expansion into the vertically extended halo (Fig. 20). Since grains with large charge-to-mass will be most affected in such a manner, this scenario is supported by the fact that halo particles are smaller than those in the main ring (de Pater et al. 1999). By the time that particles drift in as far as the 2:1 resonance, the orbits of many of them will have become highly elongated and/or inclined, meaning that some are lost to the planet's atmosphere. Although many of the Jovian rings' unique features can now be understood, questions remain—e.g., the nature of the main ring's patchiness, the cause of the exterior gossamer material and whether the known ring-moons are the primary parent bodies. Some of these may be resolved by Cassini's observations during its flyby of Jupiter at the close of 2000.

B. Saturn's E Ring

This diaphanous entity (Fig. 7) has two distinguishing features: first, nearly all of its particles are roughly the same size, about a micrometer in radius; and, second, the system's brightness peaks sharply at the satellite Enceladus' orbit, just where this vertically thickened ring is its narrowest. A dynamical simulation by Horányi et al. (1992) hinted at a possible connection between these facts, finding that micron-sized grains launched from Enceladus satisfy an orbital resonance condition. For a simple 2-D model (circular orbits, dipolar magnetic field and constant grain charge determined by the expected magnetospheric conditions) the precession of the orbit driven by Saturn's oblateness (Fig. 12) roughly matches—and thereby approximately cancels—the orbit's regression caused by the corotational electric field (Fig. 12); see also Eq. (35). Thus the $\phi_\odot$ term varies slowly, allowing radiation pressure to drive orbits to large eccentricities (Fig. 12, Eq. (28)); the variation in eccentricity is periodic on longer timescales (Figs. 19 and 21). Once the orbit achieves moderate eccentricities, particles travel along paths that cross the orbits of other Saturnian satellites, resulting in occasional collisions. Since these impacts occur typically at several km sec^{-1}, they generate significant debris (see Eq. (20)); indeed enough may be kicked off for the E ring to be self-sustained at its current optical depth. With several reasonable assumptions, this model can be shown to naturally select Enceladus as the primary source of ring material and to favor micrometer-sized grains (Hamilton and Burns 1994). The prevalence of highly eccentric orbits and the consequent energetic collisions may explain the generation of the unusual amount of submicrometer dust in the neighboring F and G rings, the excess of OH molecules observed within the E ring (Hamilton and Burns 1993b) and the orbital brightness variations of nearby satellites (Buratti et al. 1998).
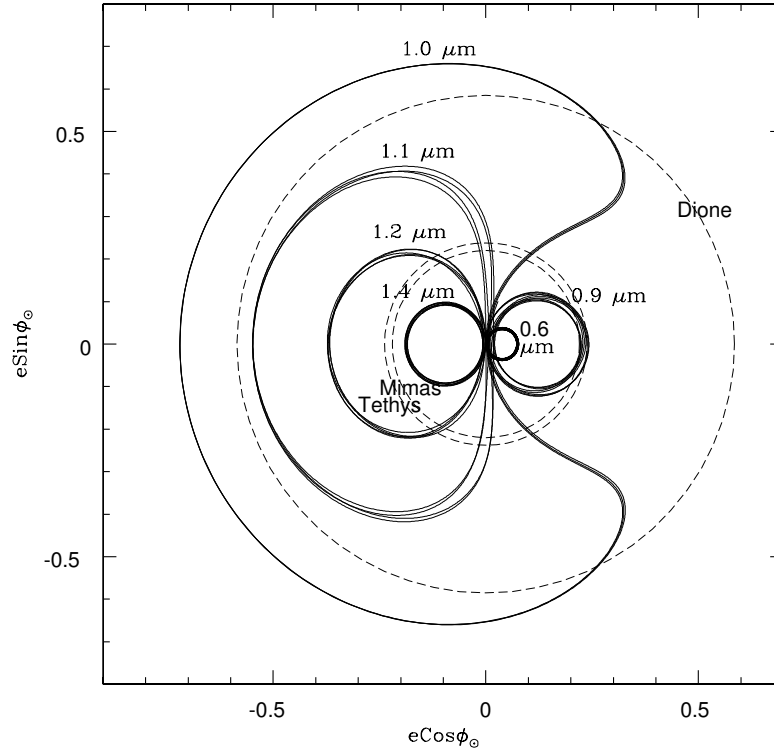
Figure 21.   Evolution of the orbital eccentricity and solar angle for different-sized E-
   ring dust grains. Particles are launched from Enceladus, and assumed to be charged
   to a potential of -5V. Note the large differences in orbital eccentricities for similar
   grain sizes (the radial distance of a point from (0,0) gives its eccentricity); this
   behavior is caused by a secular resonance that occurs when the sum of the three
   terms on the right-hand side of (39) is near zero. Eccentricities of 0.25 are sufficient
   for crossing orbits with the nearby satellites Mimas and Tethys; these eccentricities
   are attained by particles with sizes between 0.9 and 1.4 microns. Particles of $1\mu m$
   reach Dione. Large particles are offset away from the Sun (toward $\phi_\odot = 180°$ as
   was the case for dust from Deimos (see Figs. 16 and 18); the orbital histories of
   very large grains are nested inside the $1.4\mu m$ curve. The pericenters of smaller
   grains regress due to strong electromagnetic forces (see Fig. 12), which causes the
   distribution of these grains to be offset toward the Sun ($\phi_\odot = 0$). The cluster of
   curves shown for a few of the particle sizes depict the results for different orbital
   inclinations. The regular appearance of the plot is due to an underlying integral of
   the motion (Hamilton and Krivov 1996).

C. The Dust Bands of Uranus and Neptune

The Uranian system, with its dust sheet punctuated by bright strands and
gaps (Fig. 8), and the Neptunian rings, with its unusually large fraction of
dust (Fig. 9), are good testing grounds for ideas on the operation of dusty
rings. As Fig. 1 shows, each of the ring systems has several embedded and
nearby ring-moons. Because small moons near the giant planets are shattered

by cometary impacts in cosmogonically short times (Smith et al. 1989) and because the rings themselves seem to have lifetimes much less than the solar system's age (Goldreich and Tremaine 1982; Esposito et al. 1991; Porco et al. 1995), one must ask whether the intimate mix of small satellites and dusty rings that we observe today is being continually destroyed but then recreated. Cuzzi and Burns (1988) developed such a scenario to generate hypothetical debris clouds, which they claim populate the region interior to Saturn's F ring, through the sloughing off of regoliths when moonlets collide.

The most detailed collisional histories of the small Uranian and Neptunian satellites and their associated dusty ring systems have been carried out by Colwell and Esposito (1990a, b, 1992, 1993; Esposito et al. 1991; Porco et al. 1995; Canup and Esposito 1995). These authors use both Monte Carlo and Markov approaches to follow the process of satellite disruption from an initial distribution through subsequent fragmentations. The Colorado team has modeled the creation of dust in these ring systems from macroscopic bodies suffering mutual collisions and being impacted by extrinsic meteoroids. Their models include the loss of dust due to sweep-up onto the parent bodies as well as drag (exospheric and Poynting-Robertson). Using believable parameter choices, their simulations reproduce the dust contents of the Uranian and Neptunian rings as well as the impact rates at ring-plane crossings. Snapshots giving typical radial profiles of the dust optical depth are generated by combining steady-state calculations of dust within the rings with a Markov chain model for transport between the rings. These models demonstrate that vigorous inter-particle collisions are an essential ingredient to produce the high dust content, especially in light of the rapid evolution caused by the Uranian exosphere. Similar mechanisms seem likely to dominate Saturn's F ring and Encke ringlet. These results imply that all dusty ring systems must continually change their appearance.

VI. EXPECTED ADVANCES

Our knowledge about circumplanetary dust and its dynamical attributes has expanded remarkably in the last two decades. Space missions, notably Voyager to the outer solar system, first brought dusty planetary rings to the attention of scientists. But many Voyager observations of dust (imaging and plasma detections) occurred by chance, when the imaging field-of-view caught part of the "blank" background in the planet's neighborhood or when "noise" in the plasma-wave/radio data was especially prevalent as ring planes were pierced. A much more systematic survey of Jupiter's environs was planned for Galileo to carry out but it has been severely hampered by the spacecraft's damaged antenna.

The next opportunity for significant advances in our knowledge of circum-planetary dust will be in late December 2000 during Cassini's flyby of Jupiter. This mission, which carries an excellent complement of instruments (ultravio-let through infrared imaging, a sophisticated dust detector and magnetospheric

imaging), is expected to unravel much about magnetospheric interactions, the nature of the Jovian ring particles and whether these diaphanous rings show any time-variability. On Cassini's arrival at Saturn, a system that displays the widest (both geometrically and phenomenologically) array of circumplanetary dust, its observations should clarify the symbiosis believed to exist between circumplanetary dust and the other inhabitants of the magnetosphere: plasma, satellites and main rings.

Perhaps the greatest progress in the next decade will be made through terrestrial laboratory and theoretical studies on the behavior of dusty plasmas. This may be driven by an entirely different motivation: the increasing commercial interest in charged dust, owing to its role in the manufacture of microchips. Insofar as theoretical studies of circumplanetary dust, fresh numerical schemes, often incorporating non-gravitational forces into symplectic orbital integrations, are starting to be developed (Hamilton et al. 1999) and will prove useful in following the complex physics of circumplanetary dust. These improvements will be necessary to reap the harvest of puzzling data likely to be revealed during the Cassini years.

ACKNOWLEDGMENTS

REFERENCES

Acuña, M. H., and N. F. Ness 1976. The complex main magnetic field of Jupiter. J. Geophys. Res. 81, 2917–2922.

Aubier, M. G., N. Meyer-Vernet, and B. M. Pedersen 1983. Shot noise from grain and particle impacts in Saturn's ring plane. Geophys. Res. Lett. 10, 5–8.

Baguhl, M., E. Grün, G. Linkert, D. Linkert and N. Siddique 1993. Identification of "small" dust impacts in the Ulysses dust detector data. Planet. Space Sci. 41, 1085–1098.

Baguhl, M., E. Grün, D. P. Hamilton, G. Linkert, R. Riemann, P. Staubach and H. A. Zook 1994. Galileo dust. Space Sci. Rev. 72, 471–476.

Baguhl, M., D.P. Hamilton, E. Grün, S.F. Dermott, H. Fechtig, M.S. Hanner, J. Kissel, B.-A. Lindblad, D. Linkert, G. Linkert, I. Mann, J.A.M. McDonnell, G.E. Morfill, C. Polanskey, R. Riemann, G. Schwehm, P. Staubach and H.A. Zook 1995. Dust measurements at high ecliptic latitudes. Science, 268, 1016-1019.

Banaszkiewicz, M., and A. V. Krivov 1997. Hyperion as a dust source in the Saturn system. Icarus 129, 289–303.

Bauer, J., J. J. Lissauer, and M. Simon 1997. Edge-on observations of Saturn's E and G Rings in the near-IR. Icarus 125, 440–445.

Bliokh, P. V., V. Sinitsin and V. Yaroshenko 1995. Dusty and Self-Gravitation-al Plasmas in Space. Dordrecht, Boston.

Bosh, A. S., and A. S. Rivkin 1996. Observations of Saturn's inner satellites during the May 1995 ring-plane crossing. Science 272, 518–521.

Bosh, A.S., C.B. Olkin, R.G. French and P.D. Nicholson 2000. Saturn's F ring: Kinematics and particle sizes from stellar occultation studies. Icarus, submitted.

Broadfoot, A. L., F. Herbert, J. B. Holberg, D. M. Hunten, S. Kumar, B. R. Sandel, D. E. Shemansky, G. R. Smith, R. V. Yelle, D. F. Strobel, H. W. Moos, T. M. Donahue, S. K. Atreya, J. L. Bertaux, J. E. Blamont, J. C. McConnell, A. J. Dessler, S. Linick, and R. Springer 1986. Ultraviolet Spectrometer observations of Uranus. Science 233, 74–79.

Broadfoot, A. L., S. K. Atreya, J. L. Bertaux, J. E. Blamont, A. J. Dessler, T. M. Donahue, W. T. Forrester, D. T. Hall, F. Herbert, J. B. Holberg, D. M. Hunten, V. A. Krasnolpolsky, S. Linick, J. I. Lunine, J. C. McConnell, H. W. Moos, B. R. Sandel, N. M. Schneider, D. E. Shemansky, G. R. Smith, D. F. Strobel, and R. V. Yelle 1989. Ultraviolet Spectrometer observations of Neptune and Triton. Science 246, 1459–1466.

Buratti, B. J., J. A. Mosher, P. D. Nicholson, C. A. McGhee and R. G. French 1998. Near-infrared photometry of the Saturnian satellites during ring plane crossing. Icarus 136, 223–231.

Burns, J. A. 1976. An elementary derivation of the perturbation equations of celestial mechanics. Am. Jnl. Phys. 44, 944–949 (Erratum: 45, 1230).

Burns, J. A. 1991. Physical processes on circumplanetary dust. In The Origin and Evolution of Interplanetary Dust (A.-C. Levasseur-Regourd and H. Hasegawa, eds.), Kluwer Academic Publisher, Dordrecht, pp. 341–348.

Burns, J. A. 1999. Planetary rings. In The New Solar System, 4th ed. (J. K. Beatty, C. C. Petersen and A. Chaikin, eds.), Sky Publishing, Cambridge MA, pp. 221–240.

Burns, J. A., and B. J. Gladman 1998. Dynamically depleted zones near Saturn for Cassini's safe passage. Planet. Space Sci. 46, 1401–1407.

Burns, J. A., and L. Schaffer 1989. Orbital evolution of circumplanetary dust by resonant charge variations. Nature 337, 340–343.

Burns, J. A., P. L. Lamy, and S. Soter 1979. Radiation forces on small particles in the solar system. Icarus 40, 1–48.

Burns, J. A., M. R. Showalter, J. N. Cuzzi and J. B. Pollack 1980. Physical processes in Jupiter's ring: Clues for an origin by Jove! Icarus 44, 339–360.

Burns, J. A., J. N. Cuzzi, and M. R. Showalter 1983. Discovery of gossamer rings. Bull. Amer. Astron. Soc. 15, 1013–1014.

Burns, J. A., M. R. Showalter and G. Morfill 1984. The ethereal rings of Jupiter and Saturn. In Planetary Rings (R. Greenberg and A. Brahic, eds.), University of Arizona Press, Tucson, pp. 200-272.

Burns, J. A., L. Schaffer, R. J. Greenberg and M. R. Showalter 1985. Lorentz resonances

and the structure of Jupiter's rings. Nature 316, 115–119

Burns, J. A., D. P. Hamilton, F. Mignard and S. Soter 1996. The contamination of Iapetus by Phoebe dust. In Physics, Chemistry and Dynamics of Interplanetary Dust (B. A. S. Gustafson and M. S. Hanner, Eds.), Kluwer, Dordrecht, pp. 179–182.

Burns, J. A., M.R. Showalter, D. P. Hamilton, P.D. Nicholson, I. de Pater, M. Ockert-Bell and P.C. Thomas 1999. The formation of Jupiter's faint rings. Science 284, 1146–1150.

Canup, R. M., and L.W. Esposito 1995. Accretion in the Roche zone. Coexistence of rings and ring moons. Icarus 113, 331–352.

Canup, R. M., and L.W. Esposito 1997. Evolution of the G ring and the population of macroscopic ring particles. Icarus 126, 28–41.

Chamberlain, J.W. 1979. Depletion of satellite atoms in a collisionless exosphere by radiation pressure. Icarus 39, 286–294.

Cheng, A. F., P. K. Haff, R. E. Johnson and L. J. Lanzerotti 1986. Interactions of planetary magnetospheres with icy satellite surfaces. In Planetary Satellites (J. A. Burns and M. S. Matthews, eds.) University of Arizona Press, Tucson, pp. 403–430.

Colwell, J. E., and L. W. Esposito 1990a. A numerical model of the Uranian dust rings. Icarus 86, 530–560.

Colwell, J. E., and L. W. Esposito 1990b. A model of dust production in the Neptune ring system. GRL. 17, 1741–1744.

Colwell, J. E., and L. W. Esposito 1992. Origin of the rings of Uranus and Neptune. 1. Statistics of satellite disruptions. JGR 97, 10,227–10,241.

Colwell, J. E., and L. W. Esposito 1993. Origin of the rings of Uranus and Neptune. 2. Initial distribution of disrupted satellite fragments. JGR 98, 7387–7401.

Colwell, J. E., and M. Horányi 1996. Magnetospheric effects on micrometeoroid fluxes. JGR-Planets 101, 2169–2175.

Colwell, J. E., and 12 colleagues 1990. Voyager photopolarimeter observations of Uranian ring occultations. Icarus 83, 102–125.

Colwell, J. E., M. Horányi and E. Grün 1998. Capture of interplanetary and interstellar dust by the Jovian magnetosphere. Science 280, 88–91.

Connerney, J.E.P. 1993. Magnetic fields of the outer planets. J. Geophys. Res. 98, 18,659–18,679.

Connerney, J.E.P., M.H. Acuna and N.F. Ness 1996. Octupole model of Jupiter's magnetic field from Ulysses observations. J. Geophys. Res. 101, 27,453–27,458.

Cooke, M. L. 1991. Saturn's Rings: Radial Variation in the Keeler Gap and C Ring Photometry. Ph. D. dissertation, Cornell University, xii + 206 pp.

Cuzzi, J. N. 1985. Rings of Uranus: Not so thick, not so black. Icarus 63, 312–316.

Cuzzi, J. N., and J. A. Burns 1988. Charged particle depletion surrounding Saturn's F Ring: Evidence for a moonlet belt? Icarus 74, 284–324.

Cuzzi, J.N., and P. R. Estrada 1998. Compositional evolution of Saturn's rings due to meteoroid bombardment. Icarus 132, 1–35.

Cuzzi, J.N., and N. Rappaport 1996. Report to Cassini Project on Possible Ring Hazard. JPL internal document.

Cuzzi, J. N., J. J. Lissauer, L. W. Esposito, J. B. Holberg, E. A. Marouf, G. L. Tyler, and A. Boischot 1984. Saturn's rings: Properties and processes. In Planetary Rings (R. J. Greenberg and A. Brahic, Eds.), University of Arizona Press, Tucson, pp. 73–199.

Danby, J.M.A. 1988. Fundamentals of Celestial Mechanics (2nd ed.). Willmann-Bell, Richmond, VA.

de Pater, I., M. R. Showalter, J. J. Lissauer, and J. R. Graham 1996. Keck infrared observations of Saturn's E and G Rings during Earth's 1995 ring plane crossings. Icarus 121, 195-198.

de Pater, I., M. R. Showalter, J. A. Burns, P. D. Nicholson, M. Liu, D. P. Hamilton and J. R. Graham 1999. Keck infrared observations of Jupiter's ring system near Earth's 1997 ring-plane crossing. Icarus 138, 214–223.

Dermott, S.F. 1981. The braided F ring of Saturn. Nature 290, 454–457.

Dohnanyi, J. S. 1972. Interplanetary objects in review: Statistics of their masses and dynamics. Icarus 17, 1–48.

Dones, L., J. N. Cuzzi, and M. R. Showalter 1993. Voyager photometry of Saturn's A Ring. Icarus 105, 184–215.

Doyle, L. R., and E. Grün 1990. Radiative transfer modeling constraints on the size of

Saturn's spoke particles. Icarus 85, 168–190.

Doyle, L. R., L. Dones, and J. N. Cuzzi 1989. Radiative transfer modeling of Saturn's outer B Ring. Icarus 80, 104–135.

Dubinin, E.M., R. Lundin, N.F. Pissarenko, S.V. Barabash, A.V. Zakaharov, H. Koskinen, K. Schwingenshuh and Ye. G. Yeroshenko 1990. Indirect evidence for a dust/gas torus along the Phobos orbit. GRL 17, 861–864.

Dumas, C., R.J. Terrile, B.A. Smith, G. Schneider and E.E. Becklin 1999. Stability of Neptune's ring arcs in question. Nature, 400, 733-735.

Durda, D. D., and S. F. Dermott 1997. The collisional evolution of the asteroid belt and its contribution to the zodiacal cloud. Icarus 130, 140–164.

Elliot, J., and R. Kerr 1985. Rings: Discoveries from Galileo to Voyager. MIT Press, Cambridge, Mass.

Elliot, J. L., E. W. Dunham, and D. J. Mink 1977. The rings of Uranus. Nature 267, 328–330.

Elliot, J. L., A. S. Bosh, M. L. Cooke, R. C. Bless, M. J. Nelson, J. W. Percival, M. J. Taylor, J. F. Dolan, E. L. Robinson, and G. W. van Citters 1993. An occultation of Saturn's rings on 1991 October 2-3 observed with the Hubble Space Telescope. Astron. J. 106, 2544–2572, 2598.

Eplee, R. E., Jr., and B. A. Smith 1984. Spokes in Saturn's rings: Dynamical and reflectance properties. Icarus 59, 188–198.

Eplee, R. E., Jr., and B. A. Smith 1985. Radial growth of an extended spoke in Saturn's B Ring. Icarus 63, 304–311.

Esposito, L. W., A. Brahic, J. A. Burns, and E. A. Marouf 1991. Particle properties and processes in Uranus' rings. In Uranus (J. T. Bergstralh, E. D. Miner, and M. S. Matthews, Eds.), University of Arizona Press, Tucson, pp. 410–465.

Farinella, P., R. Gonczi, Ch. Froeschlé and C. Froeschlé 1993. The injection of asteroid fragments into resonances. Icarus 101, 174–187.

Feibelman, W. A. 1967. Concerning the "D" Ring of Saturn. Nature 214, 793–794.

Ferrari, C., and A. Brahic 1994. Azimuthal brightness asymmetries in planetary rings I. Neptune's arcs and narrow rings. Icarus 111, 193–210.

Fillius, R. W., C. E. McIlwain, and A. Mogro-Campero 1975. Radiation belts of Jupiter: A second look. Science 188, 465–467.

Fischer, H. M., E. Pehlke. G. Wibberenz, L. J. Lanzerotti and J. D. Mihalov 1996. High-energy charged particles in the innermost jovian magnetosphere. Science 272, 856–858.

French, R. G., P. D. Nicholson, C. C. Porco, and E. A. Marouf 1991. Dynamics and structure of the Uranian rings. In Uranus (J. T. Bergstralh, E. D. Miner, and M. S. Matthews, Eds.), University of Arizona Press, Tucson, pp. 327-409.

French, R. G., C. A. McGhee, P. D. Nicholson, L. Dones and J. Lissauer 1999. Saturn's wayward shepherds: Pandora and Prometheus. BAAS 31, 1228

French, R. G., P. D. Nicholson, M. L. Cooke, J. L. Elliot, K. Matthews, O. Perkovic, E. Tollestrup, P. Harvey, N. J. Chanover, M. A. Clark, E. W. Dunham, W. Forrest, J. Harrington, J. Pipher, A. Brahic, I. Grenier, F. Roques, and M. Arndt 1993. Geometry of the Saturn system from the 3 July 1989 occultation of 28 Sgr and Voyager observations. Icarus 103, 163–214.

French, R. G., F. Roques, P. D. Nicholson, C. A. Mc Ghee, P. Bouchet, S. A. Maene, E. C. Mason, K. Matthews and I. Mosqueira 1996. Earth-based detection of Uranus' lambda ring. Icarus 119, 269–284.

French, R. G., J. Cuzzi, R. Danos, L. Dones and J. Lissauer 1998. Hubble Space Telescope observations of spokes in Saturn's rings. Nantes abstract, p. 36.

Fujiwara, A., P. Cerroni, D. Davis, E. Ryan, M. diMartino, K. Holsapple and K. Housen 1989. Experiments and scaling laws for catastrophic collisions. In Asteroids II (R. P. Binzel, T. Gehrels and M. S. Matthews, Eds.), Univ. Arizona Press, pp. 240–265.

Gehrels, T., R. L. Baker, E. Beshore, C. Blenman, J. J. Burke, N. D. Castillo, B. DaCosta, J. Degewij, L. R. Doose, J. W. Fountain, J. Gotobed, C. E. KenKnight, R. Kingston, G. McLaughlin, R. McMillan, R. Murphy, P. H. Smith, C. P. Stoll, R. N. Strickland, M. G. Tomasko, M. P. Wijesinghe, D. L. Coffeen, and L. Esposito 1980. Imaging Photopolarimeter on Pioneer Saturn. Science 207, 434–439.

Goertz, C. K. 1989. Dusty plasmas in the solar system. Rev. Geophys. 27, 271–292.

Goertz, C. K., and G. E. Morfill 1983. A model for the formation of spokes in Saturn's ring. Icarus 53, 219–229.

Goertz, C. K., and G. E. Morfill 1988. A new instability of Saturn's ring. Icarus 74, 325–330.

Goertz, C. K., G. E. Morfill, W.-H. Ip, E. Grün and O. Havnes 1986. Electromagnetic angular momentum transport in Saturn's ring. Nature 320, 141–143.

Goertz, C. K., L. Shan and O. Havnes 1988. Electrostatic forces in planetary rings. Geophys. Res. Ltrs. 15, 84–87.

Goldreich, P., and S. Tremaine 1979. Towards a theory for the Uranian rings. Nature 277, 97–99.

Gradie, J., P. Thomas, and J. Veverka 1980. The surface composition of Amalthea. Icarus 44, 373–387.

Graps, A. L., and A. L. Lane 1986. Voyager 2 photopolarimeter experiment: Evidence for tenuous outer ring material at Saturn. Icarus 67, 205–210.

Graps, A. L., A. L. Lane, L. J. Horn, and K. E. Simmons 1984. Evidence for material between Saturn's A and F Rings from the Voyager 2 photopolarimeter experiment. Icarus 60, 409–415.

Graps, A.L., E. Grün, H. Svedhem, H. Krüger, M. Horányi, A. Heck, and S. Lammers 2000. Io as a source of the jovian dust streams. Nature, 405, 48–50.

Grün, E., G. E. Morfill, R. J. Terrile, T. V. Johnson, and G. Schwehm 1983. The evolution of spokes in Saturn's B Ring. Icarus 54, 227–252.

Grün, E., G. E. Morfill and D. A. Mendis 1984. Dust-magnetosphere interactions. In Planetary Rings (R. J. Greenberg and A. Brahic, eds.), University of Arizona Press, Tucson, pp. 275–332.

Grün, E., C. K. Goertz, G. E. Morfill and O. Havnes 1992a. Statistics of Saturn's spokes. Icarus 99, 191–201.

Grün, E., M. Baguhl, H. Fechtig, M.S. Hanner, J. Kissel, B.A. Lindblad, D. Linkert, G. Linkert, I.B. Mann, J.A.M. McDonnell, G.E. Morfill, C. Polanskey, R. Riemann, G. Schwehm, N. Siddique, and H.A. Zook 1992b. Galileo and Ulysses dust measurements: From Venus to Jupiter. Geophys. Res. Let. 19, 1311–1314.

Grün, E., H. Fechtig, M. S. Hanner, J. Kissel, B.-A. Lindblad, D. Linkert, D. Maas, G. E. Morfill, and H. A. Zook 1992c. The Galileo dust detector. Space Sci. Rev. 60, 317–340.

Grün, E., H.A. Zook, M. Baguhl, A. Balogh, S.J. Bame, H. Fechtig, R. Forsyth, M.S. Hanner, M. Horanyi, J. Kissel, B.-A. Lindblad, D. Linkert, G. Linkert, I. Mann, J.A.M. McDonnell, G.E. Morfill, J.L. Phillips, C. Polanskey, G. Schwehm, N. Siddique, P. Staubach, J. Svestka, and A. Taylor 1993. Discovery of jovian dust streams and interstellar grains by the Ulysses spacecraft. Nature 362, 428–430.

Grün, E., M. Baguhl, D.P. Hamilton, R. Riemann, H.A. Zook, S.F. Dermott, H. Fechtig, B.A. Gustafson, M.S. Hanner, M. Horanyi, K. Khurana, J. Kissel, M. Kivelson B.-A. Lindblad, D. Linkert, G. Linkert, I. Mann, J.A.M. McDonnell, G.E. Morfill, C. Polanskey, G. Schwehm, and R. Srama 1996a. Constraints from Galileo observations on the origin of jovian dust streams. Nature, 381, 395–398.

Grün, E., D.P. Hamilton, R. Riemann, S.F. Dermott, B.A. Gustafson, H. Fechtig, M.S. Hanner, A. Heck, M. Horanyi, J. Kissel, H. Krüger, B.-A. Lindblad, D. Linkert, G. Linkert, I. Mann, J.A.M. McDonnell, G.E. Morfill, C. Polanskey, G. Schwehm, R. Srama, and H.A. Zook 1996b. Dust measurements during Galileo's approach to Jupiter and Io encounter. Science, 274, 399–401.

Grün, E., Krüger, H., Dermott, S., Fechtig, H., Graps, A. L., Gustafson, B. A., Hamilton, D. P., Hanner, M. S., Heck, A., Horanyi, M., Kissel, J., Lindblad, B.A., Linkert, D., Linkert, G., Mann, I., McDonnell, J. A. M., Morfill, G. E., Polanskey, C., Schwehm, G., Srama, R., and Zook, H. A.. 1997. Dust measurements in the Jovian magnetosphere. GRL 24, 2171–2174

Grün, E., H. Krüger, A.L. Graps, D.P. Hamilton, A. Heck, G. Linkert, H.A. Zook, S. Dermott, H. Fechtig, B.A. Gustafson, M.S. Hanner, M. Horanyi, J. Kissel, B.A. Lindblad, D. Linkert, I. Mann, J.A.M. McDonnell, G.E. Morfill, C. Polanskey, G. Schwehm and R. Srama. 1998. Galileo observes electromagnetically coupled dust in the jovian magnetosphere. JGR 103, 20011–20022.

Guérin, P. 1973. Les anneaux de Saturne en 1969. Etude morpholo-gique et photométrique I. Obtention et dépouillement des photographies. Icarus 19, 202–211.

Gurnett, D. A., E. Grün, D. Gallagher, W. S. Kurth, and F. L. Scarf 1983. Micron-sized particles detected near Saturn by the Voyager Plasma Wave instrument. Icarus 53, 236–254.

Gurnett, D. A., W. S. Kurth, F. L. Scarf, J. A. Burns, J. N. Cuzzi, and E. Grün 1987. Micron-sized particle impacts detected near Uranus by the Voyager 2 Plasma Wave instrument. J. Geophys. Res. 92, 14,959–14,968.

Gurnett, D. A., W. S. Kurth, L. J. Granroth, S. C. Allendorf, and R. L. Poynter 1991. Micron-sized particles detected near Neptune by the Voyager 2 plasma wave instrument. J. Geophys. Res. 96, 19,177–19,186.

Gustafson, B. A. S. 1994. Physics of zodiacal dust. Ann. Rev. Earth Planet. Sci. 22, 553–595.

Hänninen, J. 1993. Numerical simulations of moon-ringlet interaction. Icarus, 103, 104–123.

Hamilton, D.P. 1993. Motion of dust in a planetary magnetosphere: Orbit-averaged equations for oblateness, electromagnetic, and radiation forces with application to Saturn's E ring. Icarus 101, 244–264. Erratum: Icarus 103, 161.

Hamilton, D.P. 1994. A comparison of Lorentz, planetary gravitational, and satellite gravitational resonances. Icarus 109, 221–240.

Hamilton, D.P. 1996. The asymmetric time-variable rings of Mars. Icarus 119, 153–172.

Hamilton, D. P. and J. A. Burns 1993a. The ejection of dust from Jupiter's gossamer ring. Nature 364, 695–699.

Hamilton, D. P., and J. A. Burns 1993b. OH from Saturn's rings. Nature 365, 498.

Hamilton, D.P., and J.A. Burns 1994. The origin of Saturn's E ring: Self-sustained, naturally. Science 264, 550–553.

Hamilton, D.P., and A.V. Krivov 1996. Circumplanetary dust dynamics: Effects of solar gravity, radiation pressure, planetary oblateness, and electromagnetism. Icarus 123, 503–523.

Hamilton, D.P., and A.V. Krivov 1997. Dynamics of distant moons of asteroids. Icarus 128, 141–149.

Hamilton, D.P., K. Rauch and J. A. Burns 1999. Electromagnetic resonances in Jupiter's rings. BAAS 31, 1223.

Hansen, J. E. 1969. Radiative transfer by doubling very thin layers. Astrophys. J. 155, 565–573.

Harrington, J., M. L. Cooke, W. J. Forrest, J. L. Pipher, E. W. Dunham, and J. L. Elliot 1993. IRTF observations of the occultation of 28 Sgr by Saturn. Icarus 103, 235–252.

Hartmann, W. K. 1969. Terrestrial, lunar and interplanetary rock fragmentation. Icarus 10, 201–213.

Hartquist, T. N., O. Havnes and G.E. Morfill 1992. The effects of dust on the dynamics of astronomical and space plasmas. Fund. Cosmic Physics 15, 107–142.

Havnes, O., G.E. Morfill, and F. Meland. 1992. Effects of electromagnetic and plasma drag forces on the orbit evolution of dust in planetary magnetospheres. Icarus 98, 141–150.

Herbert, F., B. R. Sandel, R. V. Yelle 1987. The upper atmosphere of Uranus- EUV Occultations observed by Voyager 2. JGR 92, 15093–15109.

Hood, L. L. 1989. Investigation of the Saturn dust environment from the analysis of energetic charged particle measurements. JPL PD 699-11, Vol. XIII.

Horányi, M. 1994. New Jovian ring. GRL 21, 1039–1042.

Horányi, M. 1996. Charged dust dynamics in the solar system. Ann. Rev. Astron. Astrophys. 34, 383–418.

Horányi, M., and J.A. Burns 1991. Charged dust dynamics: Orbital resonance due to planetary shadows. J. Geophys. Res. 96, 19,283–19,289.

Horányi, M. and T. E. Cravens 1996. Structure and dynamics of Jupiter's ring. Nature 381, 293–295.

Horányi, M. and C. C. Porco 1993. Where exactly are the arcs of Neptune? Icarus 106, 525–535.

Horányi, M., J. A. Burns, M. Tátrallyay and J. G. Luhmann 1990. On the fate of dust lost from the Martian satellites. GRL. 17, 853–856.

Horányi, M., M. Tátrallyay, A. Juhász and J. G. Luhmann 1991. The dynamics of sub-micron dust lost from Phobos. Jnl. Geophys. Res. 96, 11,283–11,290.

Horányi, M., J. A. Burns and D. P. Hamilton 1992. The dynamics of Saturn's E ring particles. Icarus 97, 248–259.

Horányi, M., G. Morfill and E. Grün 1993. Mechanism for the acceleration and ejection of dust grains from Jupiter's magnetosphere. Nature 363, 144–146.

Horányi, M., E. Grün and A. Heck 1997. Modeling the Galileo dust measurements at Jupiter.

GRL 24, 2175–2178.

Horn, L. J., J. Hui, A. L. Lane, and J. E. Colwell 1990. Observations of Neptunian rings by the Voyager photopolarimeter experiment. GRL. 17, 1745–1748.

Hubbard, W. B., A. Brahic, B. Sicardy, L.-R. Elicer, F. Roques, and F. Vilas 1986. Occultation detection of a Neptunian ring-like arc. Nature 319, 636–640.

Hubbard, W. B., C. C. Porco, D. M. Hunten, G. H. Rieke, M. J. Rieke, D. W. McCarthy, V. Haemmerle, R. Clark, E. P. Turtle, J. Haller, B. McLeod, L. A. Lebofsky, R. Marcialis, J. B. Holberg, R. Landau, L. Carrasco, J. Elias, M. W. Buie, S. E. Persson, T. Boroson, S. West, and D. J. Mink 1993. The occultation of 28 Sgr by Saturn: Saturn pole position and astrometry. Icarus 103, 215–234.

Humes D.H. 1976. The Jovian meteoroid environment. In Jupiter (T. Gehrels, ed.), pp. 1052–1067. Univ. Arizona Press; Tucson.

Humes, D. H. 1980. Results of Pioneer 10 and 11 meteoroid experiments: Interplanetary and near-Saturn. J. Geophys. Res. 85, 5841–5852.

Humes, D. H., J. M. Alvarez, R. L. O'Neal and W. H. Kinard 1974. The interplanetary and near-Jupiter meteoroid environments. J. Geophys. Res. 79, 3677–3684.

Ip, W.-H. 1995a. The exospheric system of Saturn's rings. Icarus 115, 295–303.

Ip, W.-H. 1995b. Implications of meteoroid-ring interaction for observations of the 1995 Saturn ring-plane crossing. Icarus 117, 212–215.

Ip, W.-H., and M. Banaszkiewicz 1990. On the dust-gas tori of Phobos and Deimos. Geophys. Res. Ltrs. 17, 857–860.

Ishimoto, H. 1996. Formation of Phobos/Deimos dust rings. Icarus 122, 153–165.

Johnson, R. E. 1990. Energetic Charged-Particle Interactions with Atmospheres and Surfaces. Springer-Verlag: New York, 232pp.

Johnson, R. E., D. E. Grosjean, S. Jurac and R. A. Baragiola 1993. Sputtering, still the dominant source of plasma at Dione? EOS 74, 569, 572–73.

Johnson, R. E., M. K. Pospieszalska, E. G. Sitter, A. F. Cheng, L. J. Lanzerotti and E. M. Sieveka 1989. The neutral cloud and heavy ion inner torus at Saturn. Icarus 77, 311–329.

Juhász, A., and M. Horányi 1995. Dust torus around Mars. Jnl. Geophys. Res. 100, 3277–3284.

Juhász, A., M. Tátrallyay, G. Gévai and M. Horányi 1993. On the density of the dust halo around Mars. Jnl. Geophys. Res. 98, 1205–1211.

Jurac, S., A. Baragiola, R. E. Johnson, and E. C. Sittler, Jr. 1995. Charging of ice grains by low-energy plasmas- application to Saturn's E ring. Jnl. Geophys. Res. 100, 14,821–14,835.

Jurac, S., R. Johnson and B. Donn 1998. Monte Carlo calculations of the sputtering of grains: Enhanced sputtering of small grains. Ap. J. 503, 247–252.

Kaula, W.M. 1966. Theory of Satellite Geodesy. Blaisdell Publishing Co., Waltham, MA.

Kolvoord, R. A., J. A. Burns, and M. R. Showalter 1990. Periodic features in Saturn's F ring. Nature 345, 695–697.

Kozai, Y. 1959. The motion of a close Earth satellite. Astron. J. 64, 367–377.

Krivov, A. V., and D. P. Hamilton 1997. Martian dust belts: Waiting for discovery. Icarus 128, 335–353.

Krüger, H., E. Grün, D.P. Hamilton, M. Baguhl, S. Dermott, H. Fech-tig, B.A. Gustafson, M.S. Hanner, A. Heck, M. Horanyi, J. Kissel, B.A. Lindblad, D. Linkert, G. Linkert, I. Mann, J.A.M. McDonnell, G.E. Morfill, C. Polanskey, R. Riemann, G. Schwehm, R. Srama, and H.A. Zook. 1999a. Three years of Galileo dust data: II. 1993 to 1995. Planet. Space Sci. 47, 85–106.

Krüger, H., A. V. Krivov, D. P. Hamilton, and E. Grün 1999b. Detection of an impact-generated dust cloud around Ganymede. Nature 399, 558–560.

Lane, A. L., C. W. Hord, R. A. West, L. W. Esposito, D. L. Coffeen, M. Sato, K. E. Simmons, R. B. Pomphrey, and R. B. Morris 1982. Photopolarimetry from Voyager 2: Preliminary results on Saturn, Titan and the rings. Science 215, 537–543.

Lane, A. L., C. W. Hord, R. A. West, L. W. Esposito, K. E. Simmons, R. M. Nelson, B. D. Wallis, B. J. Buratti, L. J. Horn, A. L. Graps, and W. R. Pryor 1986. Photopolarimetry from Voyager 2: Initial results from the Uranian atmosphere, satellites, and rings. Science 233, 65–70.

Lane, A. L., R. A. West, C. W. Hord, R. M. Nelson, K. E. Simmons, W. R. Pryor, L. W.

Esposito, L. J. Horn, B. D. Wallis, B. J. Buratti, T. G. Brophy, P. Yanamandra-Fisher, J. E. Colwell, D. A. Bliss, M. J. Mayo, and W. D. Smythe 1989. Photopolarimetery from Voyager 2: Initial results from the Neptunian atmosphere, satellites, and rings. Science 246, 1450–1454.

Larson, S. 1984. Summary of optical groundbased E Ring observations at the University of Arizona. In Anneaux des Planètes/Planetary Rings (A. Brahic, Ed.), Cepadues-Editions, Toulouse, France, pp. 111–113.

Lissauer, J. J., and J. Espresate 1998. Resonant satellite torques on low optical depth particulate disks. I. Analytic development. Icarus 134, 155–162.

Maravilla, D., K. R. Flammer and D. A. Mendis 1995. On the injection of fine dust from the Jovian magnetosphere. Astrophys. Jnl. 438, 968–974.

Marouf, E. A., G. L. Tyler, H. A. Zebker, and V. R. Eshleman 1983. Particle size distributions in Saturn's rings from Voyager 1 radio occultation. Icarus 54, 189–211.

Marouf, E. A., G. L. Tyler, and P. M. Rosen 1986. Profiling Saturn's rings by radio occultation. Icarus 68, 120–166.

Mauk, B. H., E. P. Keath, M. Kane, S. M. Krimigis, A. F. Cheng, M. H. Acuña, T. P. Armstrong, and N. F. Ness 1991. The magnetosphere of Neptune: Hot plasmas and energetic particles. J. Geophys. Res. 96, 19,061–19,084.

McGhee, C. A., P. D. Nicholson, R. G. French and K. J. Hall. 2000. HST Observations of Saturnian satellites during the 1995 ring plane crossings. Icarus, submitted.

McMuldroch, S. , S. H. Pilorz, G. E. Danielson and the NIMS science team 2000. Galileo NIMS near-infrared observations of Jupiter's ring system. Icarus 146, 1–11.

Meier, R., B.A. Smith, T.C. Owen, E.E. Becklin and R.J. Terrile 1999. Near infrared photometry of the jovian ring and Amalthea. Icarus 141, 253-262.

Mendis, D. A., and M. Rosenberg 1994. Cosmic dusty plasma. Ann. Rev. Astron. Astrophys. 32, 419–463.

Mendis, D. A., J. R. Hill, W.-H. Ip, C. K. Goertz and E. Grün 1984. Electrodynamic processes in the ring system of Saturn. In Saturn (T. Gehrels and M. S. Matthews, eds.), University of Arizona Press, Tucson, pp. 546–589.

Meyer-Vernet, N. 1982. Flip-flop of electric potential of dust grains in space. Astron. Astrophys. 105, 98–106.

Meyer-Vernet, N., M. G. Aubier, and B. M. Pedersen 1986. Voyager 2 at Uranus: Grain impacts in the ring plane. GRL. 13, 617–620.

Meyer-Vernet, N., A. Lecacheux, and B. M. Pedersen 1996. Constraints on Saturn's E ring from the Voyager 1 radio astronomy experiment. Icarus 123, 113–128.

Meyer-Vernet, N., A. Lecacheux and B. M. Pedersen 1998. Constraints on Saturn's G ring from the Voyager radio astronomy instrument. Icarus 132, 311–320.

Mignard, F. 1982. Radiation pressure and dust particle dynamics. Icarus 49, 347–366.

Mignard, F. 1984. Effects of radiation forces on dust particles in planetary rings. In Planetary Rings (R. Greenberg and A. Brahic, Eds.), Univ. of Arizona Press, Tucson, pp. 333–366.

Mignard, F., and M. Hénon 1984. About an unsuspected integrable problem. Cel. Mech. 33, 239–250.

Morfill, G. E., E. Grün and T. V. Johnson 1980. Dust in Jupiter's magnetosphere: Physical processes. Planet. Space Sci. 28 1087-.

Morfill, G. E., E. Grün, T. V. Johnson and C. K. Goertz 1983. On the evolution of Saturn's spokes: Theory. Icarus 53, 230–235.

Murray, C. D., and R. P. Thompson 1990. Orbits of shepherd satellites deduced from the structure of the rings of Uranus. Nature 348, 499–502 (Erratum: 350, 90).

Murray, C. D., and S. F. Dermott 1999. Solar System Dynamics, Cambridge University Press.

Murray, C. D., M. Gordon and S. M. Giulatti-Winter 1997. Unraveling the strands of Saturn's F ring. Icarus 129, 304–306.

Nicholson, P. D., and K. Matthews 1991. Near-infrared observations of the Jovian ring and small satellites. Icarus 93, 331–346.

Nicholson, P. D., I. Mosqueira, and K. Matthews 1995. Stellar occultation observations of Neptune's rings: 1984-1988. Icarus 113, 295–330.

Nicholson, P. D., M. R. Showalter, L. Dones, R. G. French, S. M. Larson, J. J. Lissauer, C. A. McGhee, P. Seitzer, B. Sicardy, and G. E. Danielson 1996. Observations of Saturn's ring plane crossings in August and November 1995. Science 272, 509–515.

Northrop, T. G. 1992. Dusty plasmas. Physica Scripta 45, 475–490.

Northrop, T. G., and T. J. Birmingham 1990. Plasma drag on a dust grain due to Coulomb collision. Planet. Space Sci. 38 319–326.

Northrop, T. G., D. A. Mendis and L. Schaffer 1989. Gyrophase drift and the orbital evolution of dust at Jupiter's ring. Icarus 79, 101–115.

Oberc, P. 1994. Dust impacts detected by Voyager 2 at Saturn and Uranus: A post-Halley view. Icarus 111, 211–226.

Ockert, M. E., J. N. Cuzzi, C. C. Porco, and T. V. Johnson 1987. Uranian ring photometry: Results from Voyager 2. J. Geophys. Res. 92, 14,969–14,978.

Ockert-Bell, M. E., J. A. Burns, I. J. Daubar, P. C. Thomas, J. Veverka, M. J. S. Belton and K. P. Klaasen 1999. The structure of Jupiter's ring system as revealed by the Galileo imaging system. Icarus 138, 188–213.

Paranicas, C. P., and A. F. Cheng 1991. Theory of ring sweeping of energetic particles. J. Geophys. Res. 96, 19,123–19,129.

Pedersen, B. M., N. Meyer-Vernet, M. G. Aubier, and P. Zarka 1991. Dust distribution around Neptune: Grain impacts near the ring plane measured by the Voyager Planetary Radio Astronomy experiment. J. Geophys. Res. 96, 19,187–19,196.

Pollack, J. B., and J. N. Cuzzi 1980. Scattering by nonspherical particles of size comparable to a wavelength: A new semi-empirical theory and its application to tropospheric aerosols. J. Atmos. Sci. 37, 868–881.

Porco, C. C. 1991. An explanation for Neptune's ring arcs. Science 253, 995–1001.

Porco, C. C., and G. E. Danielson 1982. The periodic variation of spokes in Saturn's rings. Astron. J. 87, 826–833.

Porco, C. C., P. D. Nicholson, J. N. Cuzzi, J. J. Lissauer, and L. W. Esposito 1995. Neptune's ring system. In Neptune and Triton (D. P. Cruikshank, Ed.), University of Arizona Press, Tucson, pp. 703–804.

Poulet, F., E. Karkoschka and B. Sicardy 1999. Spectrophotometry of Saturn's small satellites and rings from Hubble Space Telescope images. JGR 104, 24095–24110.

Poulet, F., B. Sicardy, P. D. Nicholson, E. Karkoschka and J. Caldwell 2000a. Saturn's ring-plane crossings of August and November 1995: A model for the new F-ring objects. Icarus 144, 135–148.

Poulet, F., B. Sicardy, C. Dumas, L. Jorda and D. Tiphéne 2000b. The crossings of Saturn's ring-plane by the Earth in 1995: Ring thickness. Icarus 145, 147–165.

Reitsema, H. J., W. B. Hubbard, L. A. Lebofsky, and D. J. Tholen 1982. Occultation by a possible third satellite of Neptune. Science 215, 289–291.

Richter, K., and H. U. Keller 1995. On the stability of dust particle orbits around cometary nuclei. Icarus 114, 355–371.

Roddier, C., F. Roddier, J. E. Graves and M. J. Northcott 1998. Discovery of an arc of particles near Enceladus' orbit: A possible key to the origin of the E ring. Icarus, 136, 50–59.

Roddier, F., C. Roddier, A. Brahic, C. Dumas, J. E. Graves, M.J. Northcott and T.C. Owen 2000. Adaptive optics observations of Saturn's ring-plane crossing in August 1995. Icarus 143, 299–307.

Sandel, B. R., D. E. Shemansky, A. L. Broadfoot, J. B. Holberg, G. R. Smith, J. C. McConnell, D. F. Strobel, S. K. Atreya, T. M. Donahue, H. W. Moos, D. M. Hunten, R. B. Pomphrey, and S. Linick 1982. Extreme ultraviolet observations from the Voyager 2 encounter with Saturn. Science 215, 548–553.

Schaffer, L., and J. A. Burns 1987. The dynamics of weakly charged dust: Motion through Jupiter's gravitational and magnetic fields. Jnl. Geophys. Res. 92, 2264–2280.

Schaffer, L.E., and J. A. Burns 1992. Lorentz resonances and the vertical structure of dusty rings: Analytical and numerical results. Icarus 96, 65–84.

Schaffer, L. E., and J. A. Burns 1994. Charged dust in planetary magnetospheres: Hamiltonian dynamics and numerical simulations for highly charged grains. Jnl. Geophys. Res. 99, 17,211–17,223.

Schaffer, L. E., and J. A. Burns 1995. Stochastic charging of dust grains in planetary rings: Diffusion rates and their effect on Lorentz resonances. Jnl. Geophys. Res. 100, 213–234.

Showalter, M. R. 1989. Anticipated time variations in (our understanding of) Jupiter's ring system. In Time-Variable Phenomena in the Jovian System (M. J. S. Belton, R. A. West, and J. Rahe, eds.), NASA-SP 494, pp. 116–125.

Showalter, M. R. 1991. Visual detection of 1981S13, Saturn's eighteenth satellite, and its role in the Encke Gap. Nature 351, 709–713.

Showalter, M. R. 1993. Longitudinal variations in the Uranian lambda Ring. Bull. Amer. Astron. Soc. 25, 1109.

Showalter, M. R. 1994. Tracking clumps in Saturn's F Ring. Bull. Amer. Astron. Soc. 26, 1150–1151.

Showalter, M. R. 1995. Arcs and clumps in the Uranian λ Ring. Science 267, 490–493.

Showalter, M. R. 1996. Saturn's D Ring in the Voyager images. Icarus 124, 677–689.

Showalter, M. R. 1998. Detection of centimeter-sized meteoroid impact events in Saturn's F Ring. Science 282, 1099–1102.

Showalter, M. R., and J. A. Burns 1982. A numerical study of Saturn's F ring. Icarus 52, 526–544.

Showalter, M. R., and J. N. Cuzzi 1992. Physical properties of Neptune's ring system. Bull. Amer. Astron. Soc. 24, 1029.

Showalter, M. R., and J. N. Cuzzi 1993. Seeing ghosts: Photometry of Saturn's G Ring. Icarus 103, 124–143.

Showalter, M. R., J. A. Burns, J. N. Cuzzi, and J. B. Pollack 1985. The discovery of Jupiter's 'gossamer' ring. Nature 316, 115–119.

Showalter, M. R., J. A. Burns, J. N. Cuzzi, and J. B. Pollack 1987. Jupiter's ring system: New results on structure and particle properties. Icarus 69, 458–498.

Showalter, M. R., J. N. Cuzzi, and S. M. Larson 1991. Structure and particle properties of Saturn's E Ring. Icarus 94, 451–473.

Showalter, M. R., J. B. Pollack, M. E. Ockert, L. Doyle, and J. B. Dalton 1992. A photometric study of Saturn's F Ring. Icarus 100, 394–411.

Showalter, M.R., J.A. Burns and D.P. Hamilton 1998. Saturn's "gossamer" ring: The F ring's inner sheet and its interaction with Prometheus BAAS 30, 1044.

Sicardy, B., F. Roques and A. Brahic 1991. Neptune's rings 1983-1989 Ground-based stellar occultation observations I. Ring-like arc detections. Icarus 89, 220–243.

Sicardy, B., F. Roddier, C. Roddier, E. Perozzi, J.E. Graves, O. Guyon and M.J. Northcott 1999. Images of Neptune's ring arcs obtained by a ground-based telescope. Nature 400, 731–733.

Simonelli, D.P., L. Rossier, P.C. Thomas, J. Veverka, J.A. Burns and M.J.S. Belton 2000. Leading-trailing albedo asymmetries of Thebe, Amalthea and Metis. Icarus, in press.

Simpson, J. A., T. S. Bastian, D. L. Chenette, R. B. McKibben, and K. R. Pyle 1980. The trapped radiations of Saturn and their absorption by satellites and rings. J. Geophys. Res. 85, 5731–5762.

Smith, B. A., L. A. Soderblom, T. V. Johnson, A. P. Ingersoll, S. A. Collins, E. M. Shoemaker, G. E. Hunt, H. Masursky, M. H. Carr, M. E. Davies, A. F. Cook, II, J. Boyce, G. E. Danielson, T. Owen, C. Sagan, R. F. Beebe, J. Veverka, R. G. Strom, J. F. McCauley, D. Morrison, G. A. Briggs, and V. E. Suomi 1979a. The Jupiter system through the eyes of Voyager 1. Science 204, 951–972.

Smith, B. A., L. A. Soderblom, R. Beebe, J. Boyce, G. Briggs, M. Carr, S. A. Collins, A. F. Cook, II, G. E. Danielson, M. E. Davies, G. E. Hunt, A. Ingersoll, T. V. Johnson, H. Masursky, J. McCauley, D. Morrison, T. Owen, C. Sagan, E. M. Shoemaker, R. Strom, V. E. Suomi, and J. Veverka 1979b. The Galilean satellites and Jupiter: Voyager 2 Imaging Science results. Science 206, 927–950.

Smith, B. A., L. Soderblom, R. Beebe, J. Boyce, G. Briggs, A. Bunker, S. A. Collins, C. J. Hansen, T. V. Johnson, J. L. Mitchell, R. J. Terrile, M. Carr, A. F. Cook, II, J. Cuzzi, J. B. Pollack, G. E. Danielson, A. Ingersoll, M. E. Davies, G. E. Hunt, H. Masursky, E. Shoemaker, D. Morrison, T. Owen, C. Sagan, J. Veverka, R. Strom, and V. E. Suomi 1981. Encounter with Saturn: Voyager 1 Imaging Science results. Science 212, 163–191.

Smith, B. A., L. Soderblom, R. Batson, P. Bridges, J. Inge, H. Masursky, E. Shoemaker, R. Beebe, J. Boyce, G. Briggs, A. Bunker, S. A. Collins, C. J. Hansen, T. V. Johnson, J. L. Mitchell, R. J. Terrile, A. F. Cook, II, J. Cuzzi, J. B. Pollack, G. E. Danielson, A. P. Ingersoll, M. E. Davies, G. E. Hunt, D. Morrison, T. Owen, C. Sagan, J. Veverka, R. Strom, and V. E. Suomi 1982. A new look at the Saturn system: The Voyager 2 images. Science 215, 504–537.

Smith, B. A., L. A. Soderblom, R. Beebe, D. Bliss, J. M. Boyce, A. Brahic, G. A. Briggs, R. H. Brown, S. A. Collins, A. F. Cook, II, S. K. Croft, J. N. Cuzzi, G. E. Danielson, M. E.

Davies, T. E. Dowling, D. Godfrey, C. J. Hansen, C. Harris, G. E. Hunt, A. P. Ingersoll, T. V. Johnson, R. J. Krauss, H. Masursky, D. Morrison, T. Owen, J. B. Plescia, J. B. Pollack, C. C. Porco, K. Rages, C. Sagan, E. M. Shoemaker, L. A. Sromovsky, C. Stoker, R. G. Strom, V. E. Suomi, S. P. Synnott, R. J. Terrile, P. Thomas, W. R. Thompson, and J. Veverka 1986. Voyager 2 in the Uranian system: Imaging Science results. Science 233, 43–64.

Smith, B. A., L. A. Soderblom, D. Banfield, C. Barnet, A. T. Basilevsky, R. F. Beebe, K. Bollinger, J. M. Boyce, A. Brahic, G. A. Briggs, R. H. Brown, C. Chyba, S. A. Collins, T. Colvin, A. F. Cook, II, D. Crisp, S. K. Croft, D. Cruikshank, J. N. Cuzzi, G. E. Danielson, M. E. Davies, E. De Jong, L. Dones, D. Godfrey, J. Goguen, I. Grenier, V. R. Haemmerle, H. Hammel, C. J. Hansen, P. Helfenstein, C. Howell, G. E. Hunt, A. P. Ingersoll, T. V. Johnson, J. Kargel, R. Kirk, D. I. Kuehn, S. Limaye, H. Masursky, A. McEwen, D. Morrison, T. Owen, W. Owen, J. B. Pollack, C. C. Porco, K. Rages, P. Rogers, D. Rudy, C. Sagan, J. Schwartz, E. M. Shoemaker, M. Showalter, B. Sicardy, D. Simonelli, J. Spencer, L. A. Sromovsky, C. Stoker, R. G. Strom, V. E. Suomi, S. P. Synnott, R. J. Terrile, P. Thomas, W. R. Thompson, A. Verbiscer, and J. Veverka 1989. Voyager 2 at Neptune: Imaging Science results. Science 246, 1422–1449.

Smyth, W. H., and M. L. Marconi 1993. The nature of the hydrogen tori of Titan and Triton. Icarus 101, 18–32.

Soter, S. 1971. The dust belts of Mars. Cornell CRSR Report 472.

Spitzer, L. 1962. Physics of Fully Ionized Gases(2nd ed.), Interscience, NY, 190pp.

Stern, D.P. 1976. Representation of magnetic fields in space. Rev. Geophys. Space Phys. 14, 199–214.

Stevenson, D. J., A. W. Harris and J. I. Lunine 1986. Origins of satellites. In Satellites (J. A. Burns and M. S. Matthews, Eds.), Univ. Arizona Press, Tucson, pp. 39–88.

Synnott, S. P., R. J. Terrile, R. A. Jacobson, and B. A. Smith 1983. Orbits of Saturn's F Ring and its shepherding satellites. Icarus 53, 156–158.

Tagger, M., R. N. Henricksen and R. Pellat 1991. On the nature of the spokes in Saturn's rings. Icarus, 91, 297–314.

Thomas, P. C., J. Veverka, and P. Helfenstein 1995. Neptune's small satellites. In Neptune and Triton (D. P. Cruikshank, Ed.), University of Arizona Press, Tucson, pp. 685–699.

Thomas, P.C., Burns, J.A., Rossier, L., Simonelli, D., Veverka, J., Chapman, C.R., Klaasen, K., Johnson, T.V., and M.J.S. Belton 1998. The small inner satellites of Jupiter. Icarus 135, 360–371.

Throop, H. B., and L. W. Esposito 1998. G ring particle sizes derived from ring plane crossing observations. Icarus 131, 152–166.

Tsintikidis, D., D. Gurnett, L. J. Granroth, S. C. Allendorf, and W. S. Kurth 1994. A revised analysis of micron-sized particles detected near Saturn by the Voyager 2 Plasma Wave instrument. J. Geophys. Res. 99, 2261–2270.

Tsintikidis, D., W. S. Kurth, D. A. Gurnett, and D. A. Barbosa 1995. Study of dust in the vicinity of Dione using the Voyager 1 plasma wave instrument. J. Geophys. Res. 99, 2261–2270.

Tsintikidis, D., D. Gurnett, W. S. Kurth and L. J. Granroth. 1996. Micron-sized particles discovered in the vicinity of Jupiter by the Voyager plasma wave instruments. GRL 23, 997–1000.

Tyler, G. L., V. R. Eshleman, J. D. Anderson, G. S. Levy, G. F. Lindal, G. E. Wood, and T. A. Croft 1981a. Radio Science investigations of the Saturn system with Voyager 1: Preliminary results. Science 212, 201–206.

Tyler, G. L., E. A. Marouf, and G. E. Wood 1981b. Radio occultation of Jupiter's ring: Bounds on optical depth and particle size, and a comparison with infrared and optical results. J. Geophys. Res. 86, 8699–8703.

Tyler, G. L., R. A. Marouf, R. A. Simpson, H. A. Zebker and V. R. Eshleman 1983. The microwave opacity of Saturn's rings at wavelengths of 3.6 and 13 cm from Voyager 1 radio occultation. Icarus 54, 160–188.

Tyler, G. L., D. N. Sweetnam, J. D. Anderson, J. K. Campbell, V. R. Eshleman, D. P. Hinson, G. S. Levy, G. F. Lindal, E. A. Marouf, and R. A. Simpson 1986. Voyager 2 Radio Science observations of the Uranian system: Atmosphere, rings and satellites. Science 233, 79–84.

Tyler, G. L., D. N. Sweetnam, J. D. Anderson, S. E. Borutzki, J. K. Campbell, V. R.

Eshleman, D. L. Gresh, E. M. Gurrola, D. P. Hinson, N. Kawashima, E. R. Kursinski, G. S. Levy, G. F. Lindal, J. R. Lyons, E. A. Marouf, P. A. Rosen, R. A. Simpson, and G. E. Wood 1989. Voyager Radio Science observations of Neptune and Triton. Science 246, 1466–1473.

Van Allen, J. A. 1982. Findings on rings and inner satellites of Saturn by Pioneer 11. Icarus 51, 509–527.

Van Allen, J. A. 1983. Absorption of energetic protons by Saturn's Ring G. J. Geophys. Res. 88, 6911–6918.

Van Allen, J. A. 1987. An upper limit on the sizes of shepherding satellites at Saturn's Ring G. J. Geophys. Res. 92, 1153–1159.

Van Allen, J. A., B. A. Randall, and M. F. Thomsen 1980. Sources and sinks of energetic electrons and protons in Saturn's magnetosphere. J. Geophys. Res. 85, 5679–5694.

van de Hulst, H. C. 1981. Light Scattering by Small Particles. Dover Publications, New York.

Wyatt, S. P., and F. L. Whipple 1950. The Poynting-Robertson effect on meteor orbits. Ap. J. 111, 134–141.

Zebker, H. A., E. A. Marouf, and G. L. Tyler 1985. Saturn's rings: Particle size distributions for thin layer models. Icarus 64, 531-548.

Zook, H.A., E. Grün, M. Baguhl, D.P. Hamilton, G. Linkert, J.-C. Liou, R. Forsyth, and J.L. Phillips 1996. Solar magnetic field bending of jovian dust trajectories. Science 274, 1501–1503.